Full simulation studies of photon and jet energy scale calibration and precise measurement of Left-Right Asymmetry using $e^+e^- \to \gamma Z$ process at the ILC

Mizuno Takahiro

The Graduate University for Advanced Studies, SOKENDAI

December 10, 2021

ABSTRACT

The International Linear Collider (ILC) is a proposed energy frontier electron-positron collider to look for new physics. Its initial center of mass energy is 250 GeV, which is extendable to 1 TeV or higher. Both electron and positron beams can be polarized. Thanks to electrons and positrons being elementary particles, the initial state is well defined and there is significantly less QCD background at the ILC than at the LHC. The resultant clean experimental environment makes it possible to perform various precision measurements including those regarding the Higgs boson properties. The ILC will thus be an ideal Higgs factory. The clean environment also allows highly sensitive searches for new particles that are difficult to find in the high QCD background environment at the LHC. To take full advantage of the ILC, a high performance detector system which can reconstruct all final states in terms of fundamental particles, *i.e.* leptons, quarks, gauge bosons, and the Higgs boson is essential. By measuring each final-state particle energy with the most appropriate sub-detectors (Particle Flow Analysis: PFA), we can achieve sufficient jet energy resolution to distinguish the W, Z, and the Higgs boson decaying into jets by reconstructing their invariant masses. The International Large Detector (ILD) is a proposed detector system at the ILC optimized for PFA. In order to make the PFA method work, not only the precision of the energy measurement but also the reduction of the energy scale uncertainty is essential. Photon and jet energy scale (JES) calibration is a key to achieve high performance PFA.

In this thesis we developed data-driven methods using the $e^+e^- \to \gamma Z$ process to calibrate the photon and jet energy in order to reduce the systematic error due to photon and jet energy scale uncertainties. These methods make use of kinematical reconstruction based on measured production angles of the final state photon and the Z-decay daughters, and in the case of JES calibration, also measured jet masses, without reference to their measured energies. Comparisons of the kinematically reconstructed energies with their corresponding measured values allow very precise controls of the photon energy scale and JES. These studies demonstrate the effectiveness of these new methods using GEANT4-based full simulation, including expected energy scale accuracies and their dependences on energy and direction, and flavor in the case of JES calibration.

Being a Higgs factory, the primary target of ILC 250 is to precisely measure the coupling constants between the Higgs boson and various other Standard Model (SM) particles. The coupling constants can deviate from their SM values due to possible Beyond the Standard Model (BSM) effects. The pattern and size of the deviations depend on the BSM models. The precision measurements of the Higgs couplings at the ILC will thus provide a new and powerful tool not only to look for BSM effects but also to identify the type of new physics thereby showing the future direction of particle physics. In order to precisely determine various Higgs couplings as model independently as possible, it has recently been recognized that SM effective field theory (SMEFT) provides an appropriate theoretical analysis framework. In the SMEFT framework, we can express deviations from SM independently of new physics models as long as the new particles are heavy enough and their field degrees of freedom can be integrated out. The deviation from the SM is expressed by a set of higher dimensional operators. It has been shown that there is a finite but complete subset of dimension-6 operators that are related to Higgs physics at

electron-positron colliders whose coefficients can be determined simultaneously by a global SMEFT fit using observables that would be measurable at ILC experiments. In this SMEFT analysis, not only the processes having Higgs bosons in the final state but also other processes with no Higgs boson will play a significant role. The $e^+e^- \to \gamma Z$ process is one of the most important such processes since this process has the potential to significantly improve the currently available A_{LR} measurement by the SLC experiment which would otherwise limit the Higgs coupling precision. It turns out that the precision of the A_{LR} measurement done at the SLC, being at around 1.5% *i.e.* $A_{LR} = 0.1514 \pm 0.0019\,(stat) \pm 0.0011\,(syst)$, is not precise enough for the global fit. It is hence motivated to improve this observable at the ILC. A_{LR} was previously measured at the Z-pole, but at the ILC, we can measure A_{LR} at 250 GeV, using the so-called radiative return events with both electron and positron polarization and 150 times larger statistics than at the SLC experiment. We therefore perform a full simulation study to evaluate by how much we can improve the precision on A_{LR}.

This thesis consists of three main topics. The first is photon energy calibration which will be described in Part II. The second is jet energy scale calibration in Part III and the third is A_{LR} measurement in Part IV.

Contents

List of Figures

List of Tables

Part I

Introduction

Chapter 1

Introduction

1.1 Physics Motivation

The International Linear Collider (ILC) is a proposed energy-frontier e^+e^- collider to look for new physics. At the first stage of the ILC, the initial center of mass energy is optimized to measure the coupling constants between the Higgs boson and various other standard model (SM) particles. The coupling constants can deviate from their SM values due to possible Beyond the Standard Model (BSM) effects. The pattern and size of the deviations depend on the BSM model. The precision measurements of the Higgs couplings at the ILC will thus provide a new and powerful tool not only to look for BSM effects but also to identify the type of new physics thereby showing the future direction of particle physics. The expected deviation is around 1-10% in typical BSM models that introduce new heavy particles at the TeV scale, which are typically beyond the discovery reach of the LHC or HL-LHC [1]. It is therefore necessary to measure the Higgs coupling constants more precisely at a future e^+e^- collider such as the ILC.

In order to precisely determine various Higgs couplings as model independently as possible, it has recently been recognized that SM effective field theory (SMEFT) provides an appropriate theoretical analysis framework. The SMEFT provides a mathematical framework to express deviations from the SM independently of new physics models as long as the new particles are heavy enough and their field degrees of freedom can be integrated out. The deviation from the SM is expressed by a set of higher dimensional operators. It has been shown that there is a finite but complete subset of dimension-6 operators that are related to Higgs physics at e^+e^- colliders whose coefficients can be determined simultaneously by a global SMEFT fit using observables that would be measurable at ILC experiments [2] [3].

The useful observables for the SMEFT global fit include not only those from the reactions that directly involve the Higgs boson, but also those from Electroweak Precision Observables (EWPOs) for W and Z bosons. An important example is the operator $i\frac{c_{HL}}{v^2}(\Phi^\dagger \overleftrightarrow{D^\mu} \Phi)(\bar{L}\gamma_\mu L)$, where Φ is the SM Higgs doublet, $\overleftrightarrow{D^\mu}$ is the covariant derivative acting on both $\Phi^\dagger$ and Φ sandwiching it, L is the lepton doublet, v is the Higgs vacuum expectation value, and c_{HL} is a dimensionless SMEFT coefficient for this operator [3] [4]. In general, this operator induces corrections to the $e^+e^- \to Zhh$, $e^+e^- \to Zh$, and $e^+e^- \to Z$ (Z-pole) processes. Therefore, the EWPOs such as the left-right polarization asymmetry A_{LR} of the Z-pole cross section and the leptonic width Γ_l of the Z boson are very helpful for constraining such an operator. It turns out that the precision of the A_{LR} measurement done at the SLC, being at around 1.5% *i.e.* $A_{LR} = 0.1514 \pm 0.0019\,(stat) \pm 0.0011\,(syst)$ [5], is not precise enough for the global fit. It is hence motivated to improve this observable at the ILC. A_{LR} was previously measured at

the Z-pole, but at the ILC, we can use the reaction $e^+e^- \to \gamma Z$ at $\sqrt{s} = 250\,\mathrm{GeV}$, the so-called radiative return process. Taking advantage of polarized beams, A_{LR} can be measured as $A_{LR} = \frac{\sigma_L - \sigma_R}{\sigma_L + \sigma_R}$, where σ_L and σ_R are the cross sections of $e^+e^- \to \gamma Z$ with, respectively, left-handed and right-handed beam polarizations. At the SLC experiment, 600 thousand Z decays were observed with e^- polarization [5]. At ILC 250, 90 million radiative return events are expected with both electron and positron polarization. We therefore would like to evaluate by how much we can improve the precision on A_{LR}. There is a fast detector simulation study available for this reaction [6], which motivated us to perform this full simulation study.

1.2 Detector Benchmark

In order to achieve the highly precise measurements stated above, a high performance detector system which can reconstruct all final states in terms of fundamental particles, *i.e.* leptons, quarks, gauge bosons, and the Higgs boson is essential. By measuring each final-state particle energy with the most appropriate sub-detectors (Particle Flow Analysis: PFA), we can achieve sufficient jet energy resolution to distinguish the W, Z, and the Higgs bosons decaying into jets by reconstructing their invariant masses. The International Large Detector (ILD) [7] is a proposed detector system at the ILC optimized for PFA [8]. The combined asymptotic momentum resolution of the ILD tracking system is $\sigma_{\frac{1}{p_T}} = 2 \times 10^{-5}\,\mathrm{GeV}^{-1}$ [7]. The energy resolution of the ECAL is $\frac{\sigma_E}{E} = \frac{17}{\sqrt{E[\mathrm{GeV}]}} \oplus 1\,\%$ [7] and that of the HCAL is $\frac{\sigma_E}{E} = \frac{50}{\sqrt{E[\mathrm{GeV}]}}\,\%$ [9]. PFA jet energy resolution is between 3 to 4% [10]. In order to make the PFA method work, not only the precision of the energy measurement but also the reduction of the energy scale uncertainty is essential. Therefore, it is important to calibrate the energy scales of various sub-detectors. The process $e^+e^- \to \gamma Z$ allows data-driven methods to perform photon and jet energy scale (JES) calibration. These methods make use of kinematical reconstruction based on measured production angles of the final state photon and the Z-decay daughters, and in the case of jet energy scale calibration, also measured jet masses, without reference to their measured energies. Comparisons of the kinematically reconstructed energies with their corresponding measured values allow very precise controls of the photon energy scale and JES. These studies demonstrate the effectiveness of these new methods by GEANT4-based full simulation, including expected energy scale accuracies and their dependences on energy and direction, and flavor in the case of JES calibration.

This thesis consists of 3 main topics. The first one is photon energy calibration which will be described in Part II, the second one is jet energy scale calibration in Part III, and the third one is A_{LR} measurement in Part IV.

Chapter 2

Physics Overview

2.1 Standard Model Physics

Particle physics aims to identify the elementary particles of which matter is composed, and to understand the interactions between them. The Standard Model (SM) of particle physics describes the elementary particles in the framework of a Lorentz-invariant gauge theory. The SM particles are identified based on various quantum numbers in the theory. First, the size of spin classifies the SM particles into three categories: spin-0 Higgs boson, spin-$\frac{1}{2}$ fermions, and spin-1 gauge bosons. Free particles with different spin values have different Lagrangian densities (2.1), (2.2), and (2.3).

$$\mathcal{L}_{spin0} = \frac{1}{2}(\partial_\mu \phi)(\partial^\mu \phi) - \frac{1}{2}m^2\phi^2 \tag{2.1}$$

$$\mathcal{L}_{spin\frac{1}{2}} = \bar{\Psi} i\gamma^\mu \partial_\mu \Psi \tag{2.2}$$

$$\mathcal{L}_{spin1} = -\frac{1}{4}F_{\mu\nu}F^{\mu\nu} \tag{2.3}$$

Spin-$\frac{1}{2}$ fermions compose matter and spin-1 gauge bosons mediates the interactions between elementary particles. Interactions treated in the SM are electromagnetic, weak and strong interactions. The electromagnetic interaction is mediated by the photon, the weak interaction by the W and Z bosons, and the strong interaction by gluons. The electroweak interaction, which unifies the electromagnetic and weak interactions, is caused by weak isospin T and weak hypercharge Y complying with $SU(2)_L \times U(1)_Y$ symmetry. The strong interaction is caused by color charge complying with $SU(3)_C$ symmetry. $SU(3)_C$ symmetry holds strictly, while $SU(2)_L \times U(1)_Y$ symmetry is spontaneously broken. This $SU(2)_L \times U(1)_Y$ symmetry breaking is caused by a phase transition of the vacuum, namely condensation of the Higgs field [11]. This Higgs field provides mass to the fermions and W and Z bosons, which would be prohibited if all of the gauge symmetries are unbroken. The Dirac equation which results from (2.2) implies two things for spin-$\frac{1}{2}$ fermions: the existence of anti-fermions which have same size of quantum numbers, but opposite charges, and the existence of two chirality states *i.e.* chirality-right and -left fermions.

Spin-$\frac{1}{2}$ fermions are classified based on their gauge charges. By the $SU(3)_C$ charge, they are classified into quarks and leptons: quarks have $SU(3)_C$ charges while leptons do not. $SU(2)_L \times U(1)_Y$ charges further distinguish these matter particles. Fermions classified based on $SU(2)_L \times U(1)_Y$ charges (for one generation) are listed in Table 2.1, where T^3 and Q are third-component of the weak isospin and electric charge, respectively. Here suffixes R and L indicate chirality-

Table 2.1: $SU(2)_L \times U(1)_Y$ charge for the chirality-left fermions

Particle	T^3	Y	Q
ν_{eL}	$+\frac{1}{2}$	$-\frac{1}{2}$	0
e_L	$-\frac{1}{2}$	$-\frac{1}{2}$	-1
u_L	$+\frac{1}{2}$	$+\frac{1}{6}$	$+\frac{2}{3}$
d_L	$-\frac{1}{2}$	$+\frac{1}{6}$	$-\frac{1}{3}$

Table 2.2: $SU(2)_L \times U(1)_Y$ charge for the chirality-right fermions

Particle	T^3	Y	Q
ν_{eR}	0	0	0
e_R	0	-1	-1
u_R	0	$+\frac{2}{3}$	$+\frac{2}{3}$
d_R	0	$-\frac{1}{3}$	$-\frac{1}{3}$

right and -left particles, respectively. Note that the right-handed neutrino ν_{eR} has no SM interactions and it is sometimes ignored in the SM. There are two more generations of quarks and leptons which have the same $SU(3)_C \times SU(2)_L \times U(1)_Y$ charge combination as particles listed in Table 2.1 but different masses. It has been shown at the LEP experiment that the number of light neutrino generations is three [5].
In total, we have the matter particles:

$$\begin{pmatrix} u_L \\ d_L \end{pmatrix}, \begin{pmatrix} c_L \\ s_L \end{pmatrix}, \begin{pmatrix} t_L \\ b_L \end{pmatrix}, u_R,\, d_R,\, c_R,\, s_R,\, t_R,\, b_R,$$
$$\begin{pmatrix} \nu_{eL} \\ e_L^- \end{pmatrix}, \begin{pmatrix} \nu_{\mu L} \\ \mu_L^- \end{pmatrix}, \begin{pmatrix} \nu_{\tau L} \\ \tau_L^- \end{pmatrix}, e_R^-,\, \mu_R^-,\, \tau_R^-, \tag{2.4}$$

and gauge bosons:

$$g_i\,(i = 1, 2, \cdots 8),\, W^{\pm},\, Z^0,\, \gamma, \tag{2.5}$$

and Higgs boson:

$$h. \tag{2.6}$$

The Lagrangian of the SM after spontaneous symmetry breaking can be expressed as follows;

$$\mathcal{L} = -\frac{1}{4}\sum_a (F^a_{\mu\nu})^2 + \left(\frac{1}{2}g(h+v)\right)^2 W^+_\mu W^{\mu-} + \frac{1}{2}\left(\frac{1}{2}g_Z(h+v)\right)^2 Z_\mu Z^\mu + \bar{L}i\gamma^\mu D_{\mu L}L + \bar{R}i\gamma^\mu D_{\mu R}R$$
$$+ \left(y_u \bar{U_L}\,(h+v)\,U_R + y_d \bar{D_L}\,(h+v)\,D_R + h.c.\right) + \frac{1}{2}(\partial_\mu h)^2 - V(h+v), \tag{2.7}$$

where $F^a_{\mu\nu}$, W_μ, Z_μ, L, R, U, D, h, and v denote the field strength tensor, W boson field, Z boson field, left-handed fermion doublet, right-handed fermion singlet, up-type fermion, down-type fermion, Higgs field, and vacuum expectation value (*i.e.* 246 GeV) respectively. g, g_Z, y_u, y_d, and $V(h)$ denote $SU(2)_L$ coupling constant, Z boson coupling constant, Yukawa coupling matrix for up-type fermion, Yukawa coupling matrix for down-type fermion, and Higgs potential, respectively. The γ^μ denotes gamma matrices and $\bar{\Psi} = \Psi^\dagger\gamma^0$. The sum over a runs over the generators of $SU(3)_C \times SU(2)_L \times U(1)_Y$. The covariant derivatives D_f are of the form

$$\begin{aligned} D_{\mu L} &= \partial_\mu - i\frac{g}{\sqrt{2}}W^+_\mu\sigma^+ - i\frac{g}{\sqrt{2}}W^-_\mu\sigma^- - ieQ_f A_\mu - i\frac{g}{c_W}Q_{Zf L}Z_\mu - ig_s A^a_\mu t^a \\ D_{\mu R} &= \partial_\mu - ieQ_f A_\mu - i\frac{g}{c_W}Q_{Zf R}Z_\mu - ig_s A^a_\mu t^a, \end{aligned} \tag{2.8}$$

where A_μ and A^a_μ denote the photon field and gluon field, respectively. Q_f, Q_{ZfL} and Q_{ZfR} denote electric charge of Ψ_f, Z charge of Ψ_{fL}, and Z charge of Ψ_{fR}, respectively. The e, g_s, c_W and t^a denote elementary charge (electron charge magnitude), $SU(3)_C$ coupling constant, cosine of the weak mixing angle θ_W and $SU(3)_C$ generators. $\sigma^\pm$ are defined as $\sigma^\pm \equiv \frac{\sigma_1 \pm i\sigma_2}{2}$.

The SM is consistent with almost all experimental results at colliders. However, it has 18 parameters which cannot be predicted by theory as shown in Table 2.4 [12] [13] and it does not include gravitational interaction and dark matter. We need a more fundamental theory, which is being explored both theoretically and experimentally.

Table 2.3: Parameters in the SM which cannot be predicted by theory [13].

Parameters	# of parameters	Remarks
Coupling constants (α_s, α, θ_W)	3	strong, electromagnetic, weak interactions
Quark masses (m_u etc.)	6	3 generations $\times$ 2 components
Quark mixing angles and phase	4	CKM (Cabibbo-Kobayashi-Masukawa) matrix
Lepton masses (m_e *etc.*)	3	Assuming $m_\nu = 0$
Higgs potential	2	Higgs mass and vacuum expectation value
Total	18	

2.2 Z Boson Physics

As we will treat the eeZ coupling in the physics analysis of this thesis, the Z boson coupling with fermions in the SM is described more closely in this section. If we define W^a_μ and B_μ as the gauge fields corresponding to $SU(2)_L$ and $U(1)_Y$ symmetries, respectively, the covariant derivative for a fermion field can be expressed as follows.

$$D_\mu = \partial_\mu - i(gT^a W^a_\mu + g\prime \frac{Y}{2} B_\mu) \tag{2.9}$$

where g and $g\prime$ denote the $SU(2)_L$ and $U(1)_Y$ coupling constants, respectively. The Z boson and photon are linear combinations of W^3_μ and B_μ. So as to extract the Z boson and photon couplings, we can introduce Z boson field Z_μ and photon field A_μ as orthogonally transformed W^3_μ and B_μ,

$$\begin{pmatrix} Z_\mu \\ A_\mu \end{pmatrix} = \begin{pmatrix} \cos\theta_W & -\sin\theta_W \\ \sin\theta_W & \cos\theta_W \end{pmatrix} \begin{pmatrix} W^3_\mu \\ B_\mu \end{pmatrix}. \tag{2.10}$$

Extracting the W^3_μ and B_μ related terms in (2.9) and using (2.10),

$$gT^3 W^3_\mu + g\prime \frac{Y}{2} B_\mu = [g\cos\theta_W T^3 - g\prime \sin\theta_W \frac{Y}{2}] Z_\mu + [g\sin\theta_W T^3 + g\prime \cos\theta_W \frac{Y}{2}] A_\mu. \tag{2.11}$$

As we regard A_μ as the photon, the coupling should be eQ where Q is electric charge in unit of e. Then,

$$g\sin\theta_W T^3 + g\prime \cos\theta_W \frac{Y}{2} = eQ = e(T^3 + \frac{Y}{2}). \tag{2.12}$$

Therefore,

$$g\sin\theta_W = g\prime\cos\theta_W = e \tag{2.13}$$

and

$$\tan\theta_W = \frac{g\prime}{g},\ e = \frac{gg\prime}{\sqrt{g^2 + g\prime^2}}. \tag{2.14}$$

With respect to Z_μ, the coupling is

$$g\cos\theta_W T^3 - g\prime \sin\theta_W \frac{Y}{2} = \frac{g}{\cos\theta_W}(T^3 - \sin^2\theta_W Q) \tag{2.15}$$

using (2.14) [14]. This means the eeZ coupling for left-handed electron g_L and that for right-handed electron g_R are

$$\begin{aligned} g_L &= \frac{g}{\cos\theta_W}(-\frac{1}{2} + \sin^2\theta_W) \\ g_R &= \frac{g}{\cos\theta_W}(\sin^2\theta_W) \end{aligned} \tag{2.16}$$

As a result, we can express the Lagrangian corresponding to the $f\bar{f}\gamma$ coupling $\mathcal{L}_{EM}$ and $f\bar{f}Z$ coupling $\mathcal{L}_{NC}$ as follows.

$$\mathcal{L}_{EM} = eA_\mu \sum_f Q_f \bar{\Psi}_f \gamma^\mu \Psi_f \tag{2.17}$$

$$\mathcal{L}_{NC} = \frac{g}{\cos\theta_W} Z_\mu \sum_f \bar{\Psi}_f \gamma^\mu (T_f^3 - \sin^2\theta_W Q_f)\Psi_f \tag{2.18}$$

Thanks to the W_μ^3 and B_μ mixing, the Z boson can couple to $T^3 = 0$ right-handed particles. We can define $Q_Z \equiv T^3 - \sin^2\theta_W Q$, Q_Z for each polarization Q_{ZL} and Q_{ZR}, and S_f and A_f as

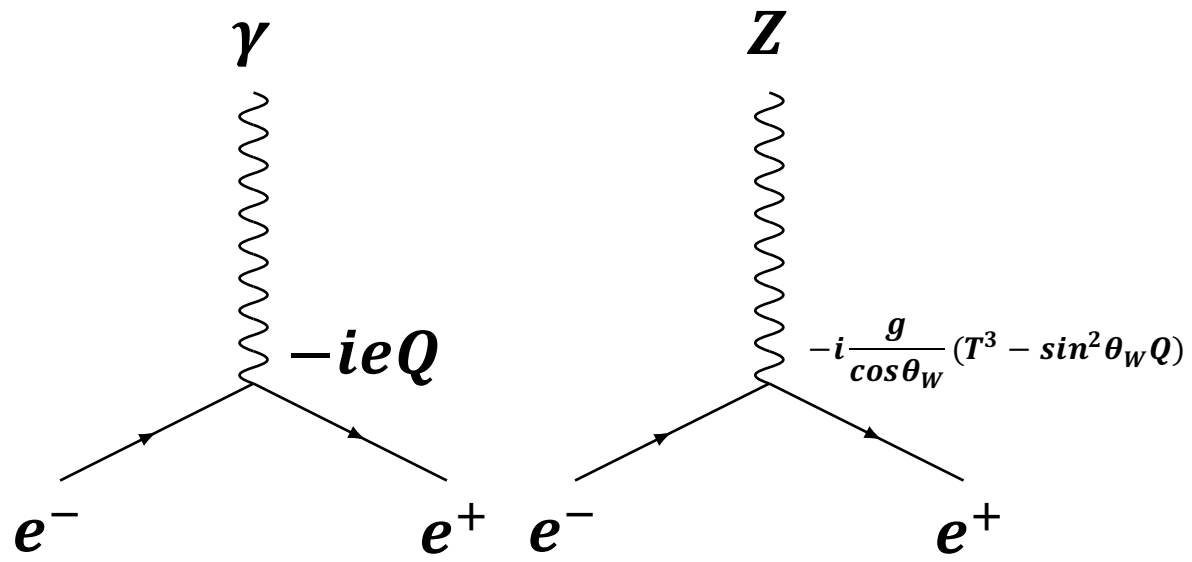

Figure 2.1: $ee\gamma$ coupling and eeZ coupling.

follows:

$$S_f = Q_{ZL}^2 + Q_{ZR}^2 \tag{2.19}$$

$$A_f = \frac{Q_{ZL}^2 - Q_{ZR}^2}{Q_{ZL}^2 + Q_{ZR}^2}. \tag{2.20}$$

The total rate for Z decay to the species f is proportional to S_f. The quantity A_f gives the asymmetry between the decay rates for left- and right-handed fermions. $\sin^2\theta_W$ is a parameter which can be determined only experimentally as shown in Table 2.4. The value is

$$\sin^2\theta_W = 0.23121 \pm 0.00004 \tag{2.21}$$

in the definition (2.13) and (2.14) ($\overline{MS}$ scheme) [15]. Then the values of S_f and A_f can be evaluated as in Table 2.4. The branching ratios of the Z to various fermions can be calculated

Table 2.4: Values of S_f and A_f

Particle	Q_{ZL}	Q_{ZR}	S_f	A_f
ν	$+0.5$		0.250	1.000
e	-0.269	$+0.231$	0.126	0.151
u	$+0.346$	-0.154	0.143	0.669
d	-0.423	$+0.077$	0.185	0.936

from S_f in Table 2.4 by the fermion masses. They are

$$\begin{aligned} BR(\nu_e\bar{\nu_e}) &= 6.8\% \\ BR(e^+e^-) &= 3.5\% \\ BR(u\bar{u}) &= 11.8\% \\ BR(d\bar{d}) &= 15.2\% \end{aligned} \tag{2.22}$$

and similarly for the fermions of the second and third generations [16]. The differential cross-sections for the $e^+e^- \to Z \to f\bar{f}$ process (Z-exchange) specific to each initial- and final-state fermion helicity are:

$$\begin{aligned} \frac{d\sigma_{Ll}}{d\cos\theta} &\propto g_{Le}^2 g_{Lf}^2 (1+\cos\theta)^2 \\ \frac{d\sigma_{Rr}}{d\cos\theta} &\propto g_{Re}^2 g_{Rf}^2 (1+\cos\theta)^2 \\ \frac{d\sigma_{Lr}}{d\cos\theta} &\propto g_{Le}^2 g_{Rf}^2 (1-\cos\theta)^2 \\ \frac{d\sigma_{Rl}}{d\cos\theta} &\propto g_{Re}^2 g_{Lf}^2 (1-\cos\theta)^2 \end{aligned} \tag{2.23}$$

Here the upper-case subscript of the cross-section defines the helicity of the initial-state electron, while the lower-case defines the helicity of the final-state fermion. Summing over final-state helicities,

$$\frac{d\sigma_{f\bar{f}}}{d\cos\theta} = \frac{3}{8}\sigma_{f\bar{f}}^{tot}[(1-P_eA_e)(1+\cos^2\theta) + 2(A_e-P_e)A_f\cos\theta], \tag{2.24}$$

where P_e stands for the effective polarization of the electron,

$$P_e = \frac{N_R - N_L}{N_R + N_L}, \tag{2.25}$$

where N_R and N_L stand for the number of right-handed polarized electrons and left-handed polarized electrons, respectively [5].

2.3 Standard Model Effective Field Theory (SMEFT)

If new physics exists, the SM must be modified. In order to investigate a more general theory, we consider the SM as an effective low-energy theory which is valid up to a certain scale Λ, and the effects from new physics as higher dimensional interactions added to the SM Lagrangian:

$$\mathcal{L} = \mathcal{L}_{SM}^{(4)} + \frac{1}{\Lambda}\sum_k C_k^{(5)} O_k^{(5)} + \frac{1}{\Lambda^2}\sum_k C_k^{(6)} O_k^{(6)} + \mathcal{O}(\frac{1}{\Lambda^3}), \tag{2.26}$$

where $\mathcal{L}_{SM}^{(4)}$ stands for the dimension-4 SM Lagrangian and $O_k^{(n)}$ denotes a dimension-n operator whose coefficient is $C_k^{(n)}$. The EFT valid below Λ should satisfy the following requirements [17]:
(i) Its gauge group should contain $SU(3)_C \times SU(2)_L \times U(1)_Y$ of the SM.
(ii) All the SM degrees of freedom should be incorporated either as fundamental or composite fields.
(iii) At low energies, it should reduce to the SM.
Considering the constraints above, only one dimension-5 operator exists, which violates lepton number L for one generation when hermitian conjugates of fermionic operators are not counted separately. Assuming baryon number conservation, there exist 59 independent dimension-6 operators: 15 0-fermion fields *i.e.* bosonic operators, 19 2-fermion fields *i.e.* single-fermionic-current operators, 25 4-fermion fields *i.e.* B-conserving four-fermion operators. There exist 4 independent dimension-6 operators which violate baryon number [17]. Many of these operators have flavor (generation) indices. For three generations, the dimension-6 Lagrangian has 1350 CP-even and 1149 CP-odd couplings, for a total of 2499 hermitian operators [18].

While there is such a very large number of free parameters, at e^+e^- colliders, it is shown that we can analyze the extension of the Standard Model (SM) by addition of 10 effective operators that describe the most general new physics effects on the couplings of the Higgs boson to the W, Z, γ, and the light leptons and can constrain the coefficients of these operators simultaneously [3]. The 10 effective operators considered in the analysis are

$$\begin{aligned}\Delta\mathcal{L} = {} & \frac{c_H}{2v^2}\partial^\mu\left(\Phi^\dagger\Phi\right)\partial_\mu\left(\Phi^\dagger\Phi\right) + \frac{c_T}{2v^2}\left(\Phi^\dagger\overleftrightarrow{D^\mu}\Phi\right)\left(\Phi^\dagger\overleftrightarrow{D_\mu}\Phi\right) - \frac{c_6\lambda}{v^2}\left(\Phi^\dagger\Phi\right)^3 \\ & + \frac{g^2 c_{WW}}{m_W^2}\Phi^\dagger\Phi W^a_{\mu\nu}W^{a\mu\nu} + \frac{4gg\prime c_{WB}}{m_W^2}\Phi^\dagger t^a\Phi W^a_{\mu\nu}B^{\mu\nu} + \frac{g\prime^2 c_{BB}}{m_W^2}\Phi^\dagger\Phi B_{\mu\nu}B^{\mu\nu} + \frac{g^3 c_{3W}}{m_W^2}\epsilon_{abc}W^a_{\mu\nu}W^{b\nu}_\rho W^{c\rho\mu} \\ & + i\frac{c_{HL}}{v^2}(\Phi^\dagger\overleftrightarrow{D^\mu}\Phi)(\bar{L}\gamma_\mu L) + 4i\frac{c\prime_{HL}}{v^2}(\Phi^\dagger t^a\overleftrightarrow{D^\mu}\Phi)(\bar{L}\gamma_\mu t^a L) + i\frac{\bar{c}_{HE}}{v^2}(\Phi^\dagger\overleftrightarrow{D^\mu}\Phi)(\bar{e}\gamma_\mu e).\end{aligned} \tag{2.27}$$

If new physics modifies the SM, the size of corrections to the SM Higgs boson couplings can be expressed as

$$a\frac{m_h^2}{M^2}, \tag{2.28}$$

where M is new particle mass, m_h is the Higgs mass, and a is a coefficient of order 1. As the exclusions of new particles through searches at the LHC suggest that M is at least close to 1 TeV which corresponds to the effects of new physics around 10%, we need to measure Higgs couplings with a precision at least of order 1% for further exploration [9]. These operators can be determined not only from the reactions that directly involve the Higgs boson, but also W and Z bosons. For example, reactions including the eeZ coupling are important to constrain the operators.

2.4 eeZ Coupling

First, EFT parameters relevant to the eeZ coupling will be considered. Contributions to g_L, the left-handed electron coupling to the Z, include the effects of contact interactions and AZ kinetic mixing shown in Fig. 2.2. The contributions to g_R have a similar structure as shown in Fig. 2.3.

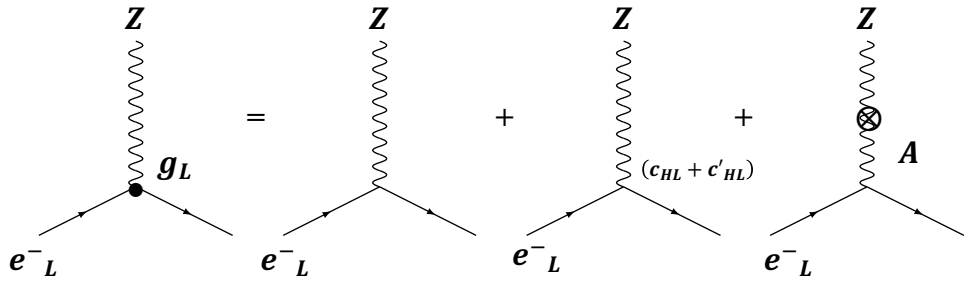

Figure 2.2: g_L, left-handed electron coupling to the Z.

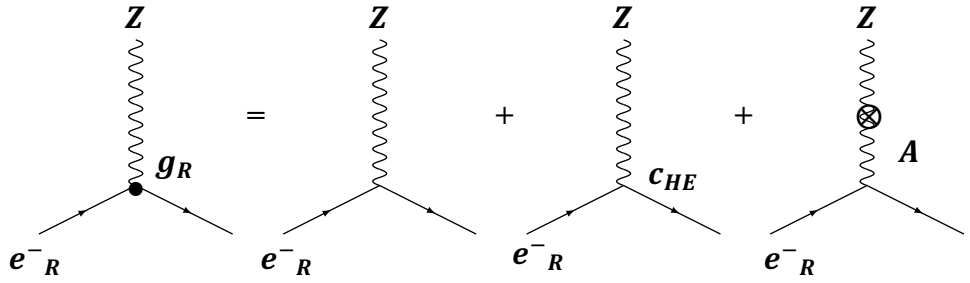

Figure 2.3: g_L, right-handed electron coupling to the Z.

When we look at the EFT Lagrangian (2.27), the following 3 terms are relevant to the contact interactions:

$$\begin{aligned} i\frac{c_{HL}}{v^2}(\Phi^\dagger \overleftrightarrow{D^\mu}\Phi)(\bar{L}\gamma_\mu L) \\ 4i\frac{c\prime_{HL}}{v^2}(\Phi^\dagger t^a \overleftrightarrow{D^\mu}\Phi)(\bar{L}\gamma_\mu t^a L) \\ i\frac{\bar{c}_{HE}}{v^2}(\Phi^\dagger \overleftrightarrow{D^\mu}\Phi)(\bar{e}\gamma_\mu e) \end{aligned} \tag{2.29}$$

and the following 3 terms are relevant to AZ mixing:

$$\begin{aligned} \frac{g^2 c_{WW}}{m_W^2}\Phi^\dagger\Phi W^a_{\mu\nu}W^{a\mu\nu} \\ \frac{4gg\prime c_{WB}}{m_W^2}\Phi^\dagger t^a\Phi W^a_{\mu\nu}B^{\mu\nu} \\ \frac{g\prime^2 c_{BB}}{m_W^2}\Phi^\dagger\Phi B_{\mu\nu}B^{\mu\nu}. \end{aligned} \tag{2.30}$$

In this formalism, g_L and g_R are expressed as follows [3] :

$$\begin{aligned} g_L &= \frac{g}{c_W}[(-\frac{1}{2}+s_W^2)(1+\frac{1}{2}\delta Z_Z)-\frac{1}{2}(c_{HL}+c\prime_{HL})-s_W c_W \delta Z_{AZ}] \\ g_R &= \frac{g}{c_W}[(+s_W^2)(1+\frac{1}{2}\delta Z_Z)-\frac{1}{2}c_{HE}-s_W c_W \delta Z_{AZ}] \\ \delta Z_Z &= c_W^2(8c_{WW})+2s_W^2(8c_{WB})+\frac{s_W^4}{c_W^2}(8c_{BB}) \\ \delta Z_{AZ} &= s_W c_W((8c_{WW})-(1-\frac{s_W}{c_W^2})(8c_{WB})-\frac{s_W}{c_W^2}(8c_{BB}) \end{aligned} \tag{2.31}$$

The contribution to the deviation of the eeZ coupling is different for each polarization. The left-right asymmetry in the Z production cross section can be written as

$$A_{LR} = \frac{\sigma_L - \sigma_R}{\sigma_L + \sigma_R}. \tag{2.32}$$

Measuring A_{LR} is equivalent to measurement of A_e.

$$\begin{aligned} A_e &= \frac{g_{Le}^2 - g_{Re}^2}{g_{Le}^2 + g_{Re}^2} \\ \delta A_e &= \frac{4g_{Le}^2 g_{Re}^2(\delta g_{Le} - \delta g_{Re})}{g_{Le}^4 - g_{Re}^4} \end{aligned} \tag{2.33}$$

If we define g_V and g_A as

$$\begin{aligned} g_V &= g_L + g_R \\ g_A &= g_L - g_R, \end{aligned} \tag{2.34}$$

then A_e can be expressed as

$$A_e = \frac{2g_{Vf}g_{Af}}{g_{Vf}^2 + g_{Af}^2} = 2\frac{\frac{g_{Vf}}{g_{Af}}}{1+(\frac{g_{Vf}}{g_{Af}})^2}. \tag{2.35}$$

Thus A_e depends only on the ratio of the couplings. As we have already seen, measurement of A_{LR} allows us to determine the deviation of the eeZ coupling for each polarization and to constrain EFT operators. The current best measurement of A_{LR} is

$$A_{LR} = 0.1514 \pm 0.0019\,(stat) \pm 0.0011\,(syst)\,[5]. \tag{2.36}$$

At the SLC experiment, 600 thousand Z decays were observed with a polarized e^- beam [5]. The improvement of the Higgs coupling is from dark to light green in Fig. 2.4 [9] when there are a factor of 10 improvement in the A_{LR} through the measurement of $e^+e^- \to Z$ with polarized beams at 250 GeV, 10% improvement in signal efficiency of the jet clustering algorithm, 20% improvement in the performance of the flavor tagging algorithm, 20% improvement in statistics by including more signal channels in $\sigma_{Zh}\cdot BR(h \to WW)$, and 30% improvement in the precision of Higgs self-coupling and top-Yukawa coupling at 500 GeV, which is a consequence of the improvements in jet clustering algorithm, flavor tagging algorithms and statistics by including more signal channels. Especially, hZZ and hWW couplings only depend on the A_{LR} precision. At the ILC 250, 90 million radiative return events are expected with both electron and positron polarization. We present in Part IV a full detector simulation of radiative return events and evaluate the improvement of the precision on A_{LR}.

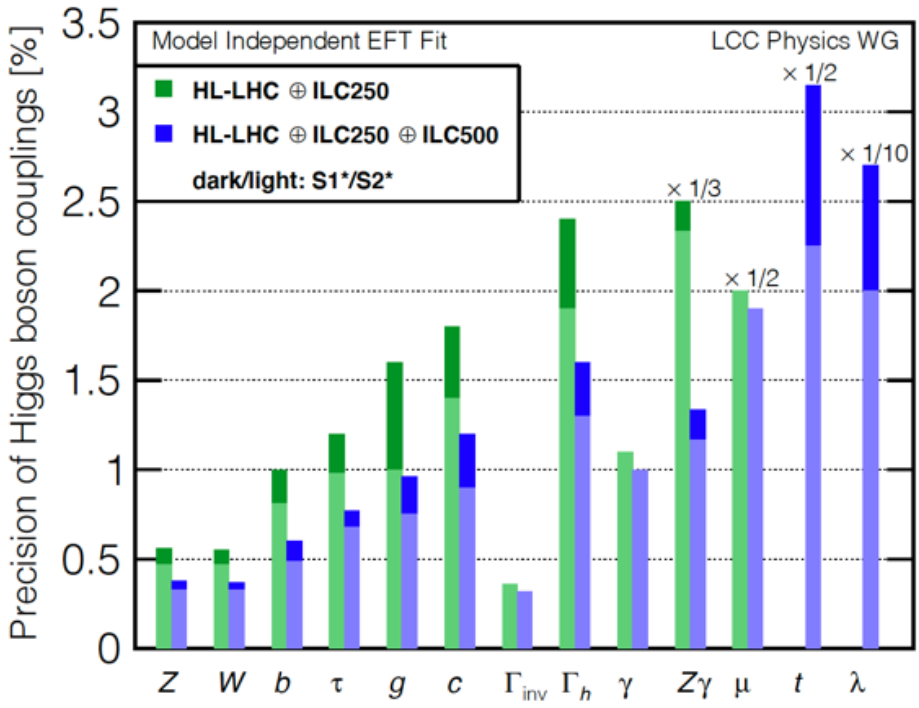

Figure 2.4: Improvement of the Higgs coupling before (dark green) and after (light green) the 10 times improvement of A_{LR} precision and other analysis improvements [9].

Chapter 3

International Linear Collider (ILC)

3.1 ILC Overview

The International Linear Collider (ILC) is a future electron-positron collider which will be the world's highest energy lepton collider, and at which beam polarization is available. The ILC collision energy $\sqrt{s}$ is proposed to be 250, 350 and 500 GeV and extendable to even higher energy, and 80% polarized electron beam and 30% polarized positron beam are available. Using ILC, we can explore new physics and precisely measure observables in the unexplored high energy region. A comparison with the properties of the Large Hadron Collider (LHC) is shown in Table 3.1. As

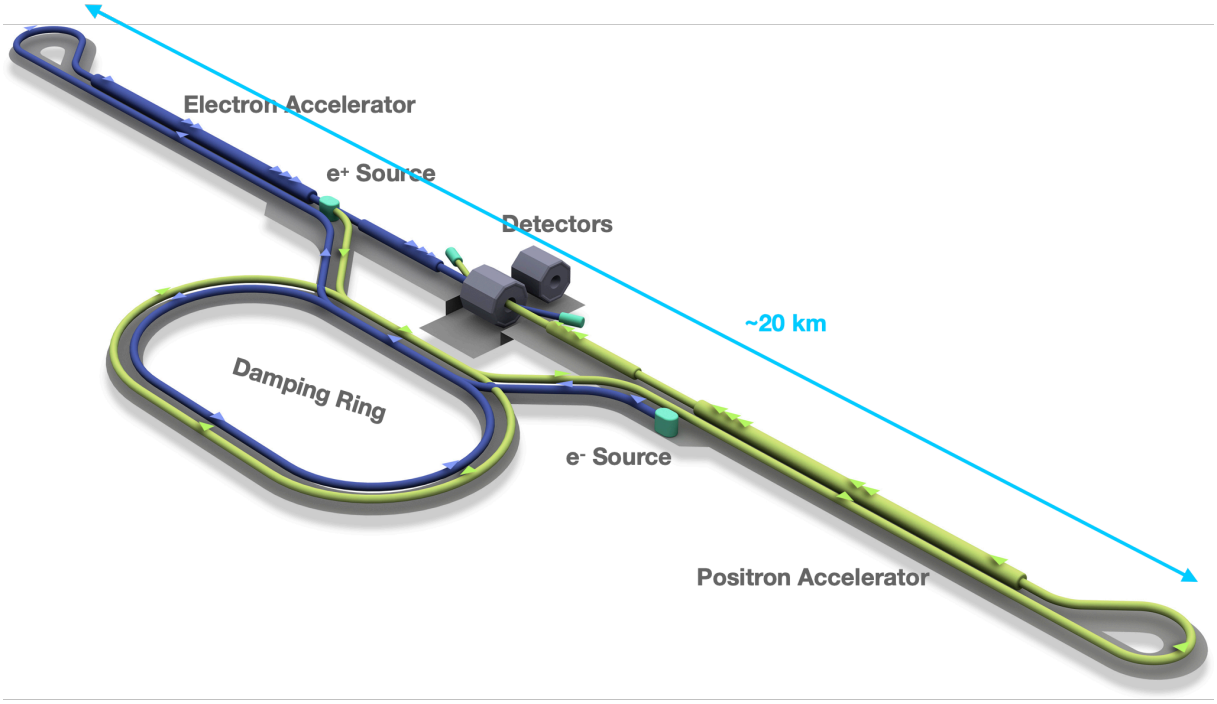

Figure 3.1: Bird's-eye view of the International Linear Collider (ILC) © Rey.Hori.

LHC is a proton-proton collider which collides protons which are composed of colored particles, there are many QCD background events while ILC uses e^+ and e^- which leads to a cleaner signal. The difference of the shape of the accelerator is related to synchrotron radiation. When a charged particle changes its direction, it loses energy proportional to γ^4 where $\gamma = \frac{E}{mc^2}$ [15].

Table 3.1: Properties of LHC and ILC

	LHC [19]	ILC [9]
Colliding particles	pp	e^+e^-
Shape	circular	linear
Center of mass energy	14 TeV at Run-3	250, 350, 500 GeV
Luminosity	$2.0 \times 10^{34}\text{cm}^2\text{s}^{-1}$	$1.35 \times 10^{34}\text{cm}^{-2}\text{s}^{-1}$ at 250 GeV

As this effect depends on particle mass, electrons lose energy more easily. In order to achieve high energy while avoiding energy loss, ILC uses linear shaped accelerators.

At the energy of 250 GeV, the cross section for the Higgs-strahlung process $e^+e^- \to Zh$ is near the peak and precision Higgs couplings measurements are possible. At the energy of 350 GeV, scanning the threshold for top quark pair production will be performed, and at the energy of 500 GeV, two important processes become directly accessible: $e^+e^- \to t\bar{t}h$ process which includes top Yukawa coupling and $e^+e^- \to Zhh$ process whose cross section is maximum at around 500 GeV which includes the triple Higgs coupling [9] [20]. Higgs production processes at the ILC are shown in Fig. 3.2. The luminosity is $1.35 \times 10^{34}\,\text{cm}^{-2}\text{s}^{-1}$ at 250 GeV. In every physics study, systematic uncertainty depends on the settings of center-of-mass energies and beam polarization. Proposed integrated luminosity for each energy and polarization are listed in Table 3.2, where P_{e^-} and P_{e^+} stand for the electron beam polarization and positron beam polarization, respectively [9] [20] and the 22-year run plan for the staged ILC machine is shown in Fig. 3.3 [21].

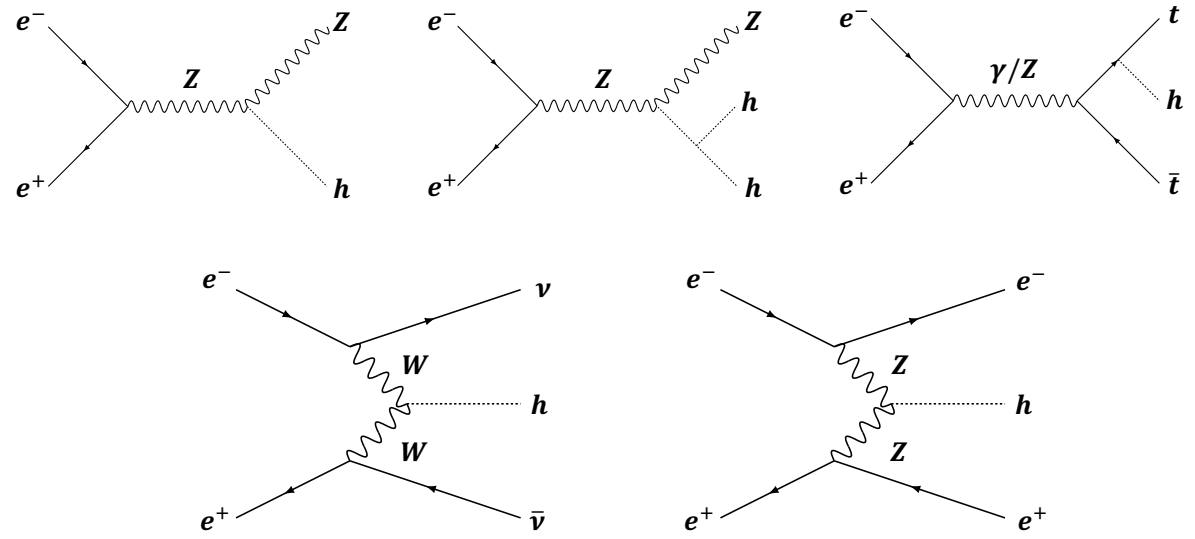

Figure 3.2: Higgs production processes at the ILC. Top right, top middle, top left, bottom right, and bottom left processes correspond to the single Higgs production by Higgs-strahlung, double Higgs production by Higgs-strahlung, $t\bar{t}h$, WW fusion, and ZZ fusion, respectively.

3.2 Electron and positron source

At the ILC, each electron and positron beam has the same time structure with a 727 μs train pulse with a repetition rate of 5 Hz. Each train consists of 1312 bunches of 2.0×10^{10} electrons

Table 3.2: Proposed integrated luminosity for each energy and polarization at the ILC [9]

	Integrated luminosity [fb^{-1}] for polarization (P_{e^-}, P_{e^+})				
$\sqrt{s}$[GeV]	(−,+)	(+,−)	(−,−)	(+,+)	Total
250	900	900	100	100	2000
350	135	45	10	10	200
500	1600	1600	400	400	4000

or positrons. The 199 ms interval between bunch trains provides ample time for a full readout of data from the previous train [9].

The electron beam is produced by a laser illuminating a strained GaAs/GaAsP superlattice photocathode in a DC gun [22]. In the DC gun, the strained GaAs layer resolves the degeneracy of heavy-hole and light-hole bands at the valence-band and we can enhance only the electron with a particular angular momentum state [23], which provides at least 85% electron polarization, sufficient for 80% beam polarization at the interaction point. Normal-conducting structures are used for bunching and pre-acceleration to 76 MeV, after which the beam is accelerated to 5 GeV in a superconducting linac. Before injection into the damping ring, superconducting solenoids rotate the spin vector into the vertical direction [22] [9]. A schematic view of the electron source is shown in Fig. 3.4.

For the positron beam, the primary electron beam after acceleration in the main linac is transported through a 147 m superconducting helical undulator which generates photons with energies from $\sim$ 10 MeV up to $\sim$ 30 MeV depending on the electron beam energy. We can get polarized photons from the undulator which are directed onto a rotating 0.4 radiation-length Ti-alloy target $\sim$ 500 meters downstream, producing electron and positron pairs. The obtained polarized positron beam is then matched using an optical-matching device (a pulsed flux concentrator) and accelerated to 125 MeV. Then positrons are accelerated to 400 MeV in two normal conducting preaccelerators with solenoidal focusing followed by a superconducting accelerator very similar to the main linac before they are injected into the damping rings at 5 GeV [22] [9]. The layout of the positron source is shown in Fig. 3.5.

Frequent enough helicity reversal of each beam is required so as to control systematic effects. For the electron beam, a fast helicity reversal is possible through a flip of the cathode laser polarization. For the positron beam, the spin rotators in front of the damping rings are used that rotate the polarization vector either to the $+y$ or $-y$ direction. With this scheme, fast kickers can select a path through either of the two spin rotators and thus provide a fast spin reversal capability [9].

3.3 Damping Ring, Main Linac, and beam-delivery system

Damping Rings (DR) accept the 5 GeV electrons and positrons and reduce the horizontal and vertical emittance of the beams by almost six orders of magnitude within a time span of 100 ms. It is housed in a common tunnel at the center of the ILC complex with a circumference of 3.2 km. The beam from the Damping Ring is transported into the Ring to Main Linac (RTML) system, which transport the low emittance beam at 5 GeV with minimal emittance increase, to the upstream ends of the Main Linacs. RTML system also collimates the beam halo generated in the Damping Rings. The beam polarization is vertical in the Damping Rings. Before entering the linac, RTML system rotates the spin polarization vector from the vertical to any arbitrary

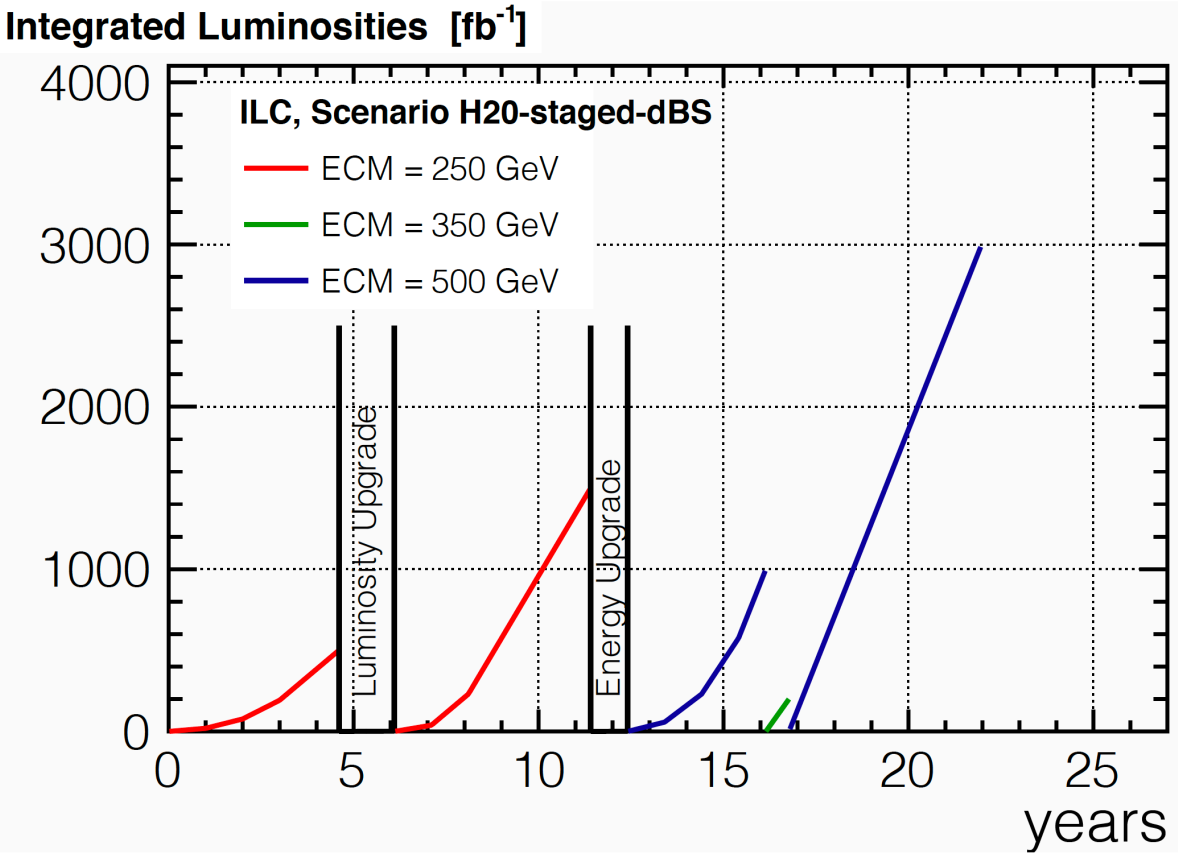

Figure 3.3: the 22-year run plan for the staged ILC machine [21].

angle required at the IP [22].

Two $\sim$ 7.5 km long Main Linacs accelerate the beams from 5 GeV to a maximum energy of 125 GeV [24]. The ILC Main Linacs utilize 1.3 GHz SCRF cavities operating at an average gradient of 31.5 MV/m with a pulse length of 1.6 ms. Beam acceleration in each linac is provided by approximately 8000 $\sim$ 1 m-long superconducting niobium cavities consisting of nine elliptical cells operating at 2 K (Fig. 3.9), assembled into $\sim$ 900 cryomodules [24]. Then a 2×2.25 km-long beam-delivery system with the final-focus (FF) system demagnifies the beam to the required size (474 nm horizontal and 5.9 nm vertical) at the IP. Two beams go into collision with a 14 mrad crossing angle, at a single interaction point which can be shared by two detectors (push-pull) [22] [9]. The resulting luminosity spectrum is shown in Fig. 3.7.

Two energy spectrometers, located 700 m upstream and 55 m downstream of the IP provide measurements of the beam energy with an accuracy of 100 ppm. The luminosity is measured to 10^{-3} accuracy in the LumiCal and BeamCal which will be describes in section 3.4.6. Beam polarization is measured with 0.25% accuracy by means of Compton scattering: we can infer the beam polarization by using the momentum spectrum of electrons which lose enough energy by scattering laser photons. Two such polarimeters are located 1800 m upstream and 150 m downstream of the IP, which allows to interpolate the precise polarization at the IP and control the systematics, including effects from precession of the polarization vector by transverse fields and depolarizing effects in the interaction, which lead to a sizable variation of the polarization within the bunch during the collision [9].

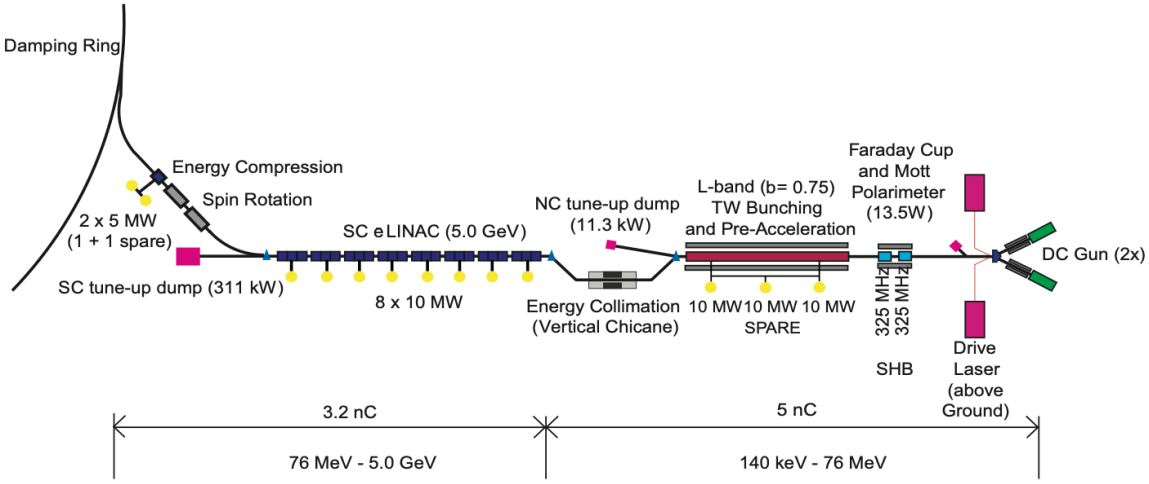

Figure 3.4: Schematic view of the electron source [22].

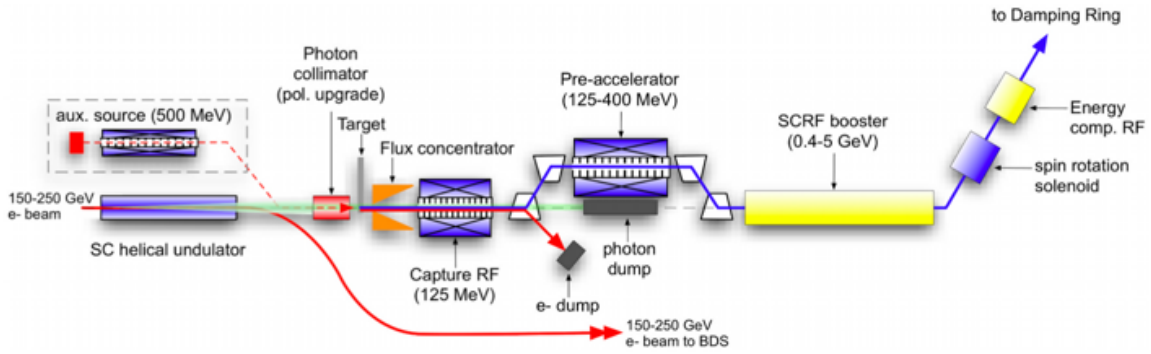

Figure 3.5: Layout of the positron source [22].

Figure 3.6: 1.3 GHz superconducting nine-cell niobium cavity [22].

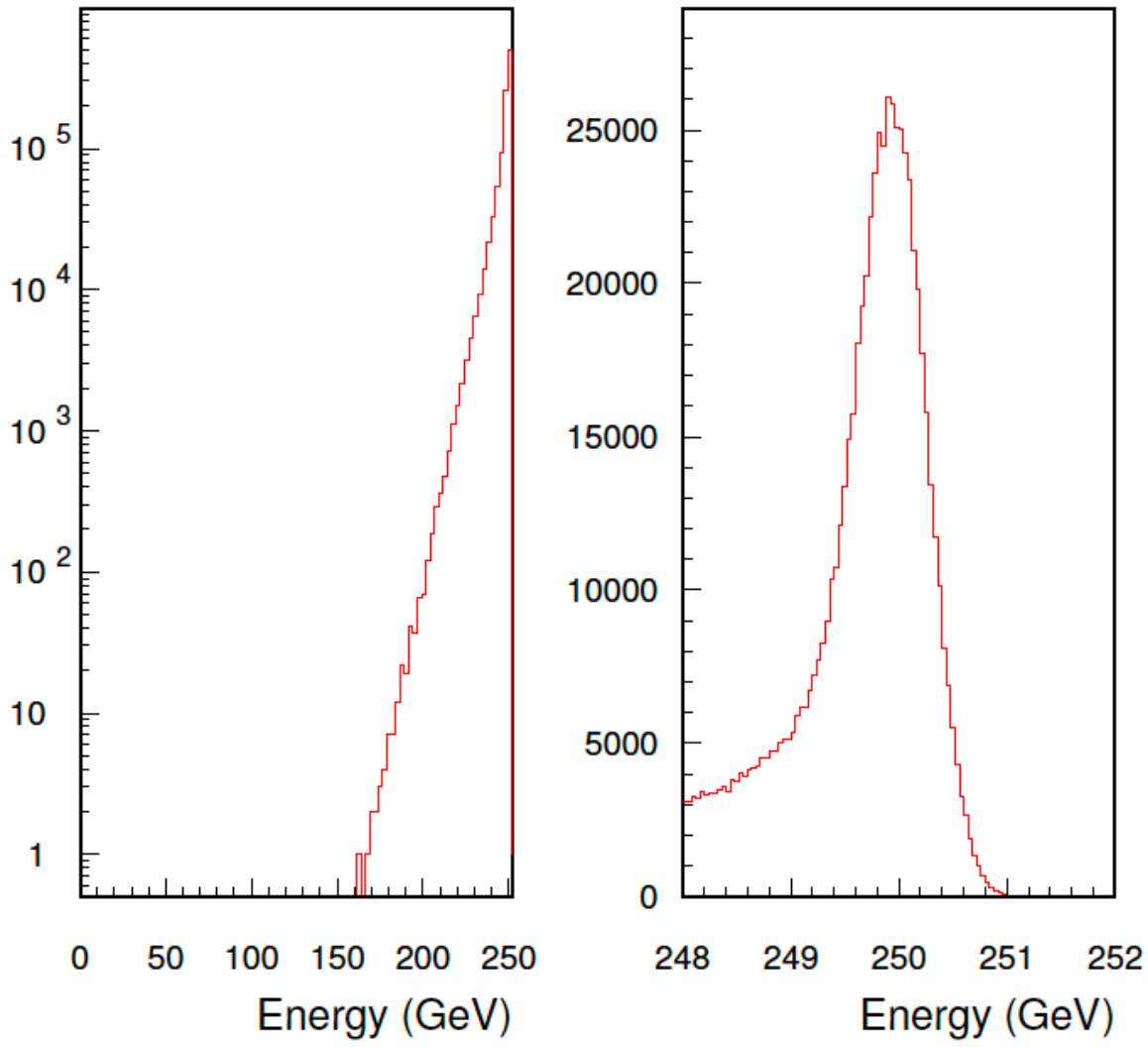

Figure 3.7: Luminosity spectrum for ILC 250 [20].

3.4 International Large Detector (ILD)

The International Large Detector (ILD) [7] is a detector concept for the ILC designed for precise measurements of each particle in the final state using the Particle Flow Algorithm [8]. The ILD (Fig. 3.8) has been designed as a general purpose collider detector. A high precision vertex detector is followed by an inner silicon tracker, a time projection chamber (TPC), an outer silicon tracker, an electromagnetic calorimeter (ECAL), and a hadronic calorimeter (HCAL). The complete tracking and calorimetry system is located inside a large solenoidal coil, which generates 3.5 or 4 T magnetic field. Outside the coil, the iron return yoke is instrumented as a muon detector and as a tail catcher calorimeter. The combined asymptotic momentum resolution of the ILD tracking system is $\sigma_{\frac{1}{p_T}} = 2 \times 10^{-5}\,\mathrm{GeV}^{-1}$ [7]. The energy resolution of the ECAL is $\frac{\sigma_E}{E} = \frac{17}{\sqrt{E[\mathrm{GeV}]}} \oplus 1\,\%$ [7] and that of the HCAL is $\frac{\sigma_E}{E} = \frac{50}{\sqrt{E[\mathrm{GeV}]}}\,\%$ [9].

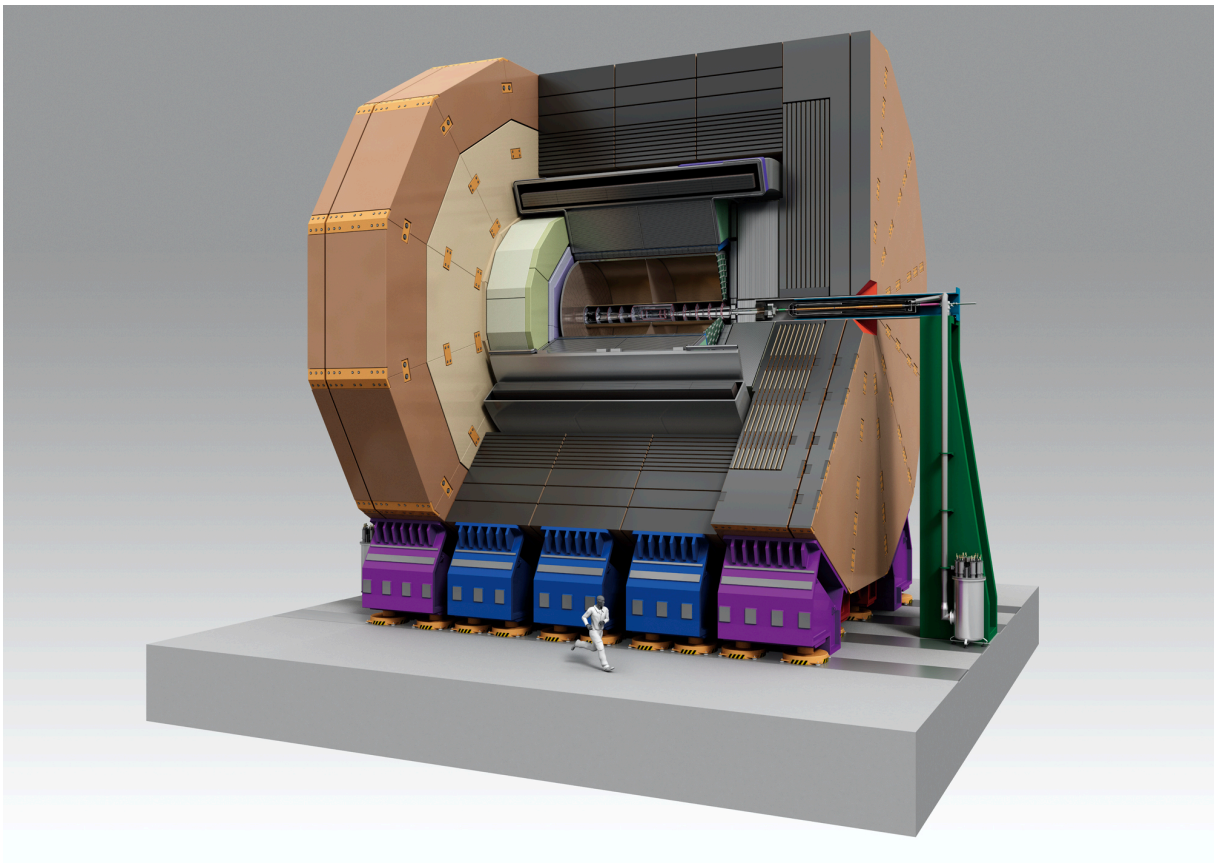

Figure 3.8: View of the International Large Detector (ILD) [7].

3.4.1 ILD vertex system

Bottom quark, charm quark, and tau lepton identification is essential for the ILC experiment. To do this, the Vertex detector (VTX), a multi-layer pixel detector, is implemented. The reconstruction of decay vertices of short lived particles such as D or B mesons is done by reconstructing the trajectory of their decay products. This is achieved through the very precise measurement of the charged particles' track parameters in the vicinity of the interaction point.

The performance of a vertex detection system can be expressed by the resolution on the impact parameter, which is the minimum distance from a track to the beam axis. VTX has three double-layers [9] resulting in six measured positions for each charged particle traversing the detector. The required resolution on the track impact parameter is $\sigma_b < 5 \oplus \frac{10}{p \sin^{\frac{3}{2}} \theta}\, \mu\,\mathrm{m}$[7] and the material thickness which should not exceed $0.15\% X_0$ per layer to minimize multiple scattering. There are three technological options for the pixel sensors: CMOS Pixel Sensors (CPS) [25], Fine Pixel CCD (FPCCD) sensors [26], and Depleted Field Effect Transistor (DEPFET) sensors [27].

3.4.2 The ILD silicon tracking system

The silicon part of the ILD tracking system is made of three components: two barrel components, the Silicon Inner Tracker (SIT) and the Silicon External Tracker (SET), and the forward tracker (FTD). SIT bridges the gap between VTX detector and the TPC, and SET between the TPC and the ECAL. These improves the overall momentum resolution. In the very forward region, FTD provides precise tracking at small polar angle [7]: the FTD acceptance starts at $|\cos\theta| \sim 0.996$, with at least one hit for tracks with polar angles below $|\cos\theta| \sim 0.82$ and nearly standalone tracking for tracks below $|\cos\theta| \sim 0.96$ [20].

3.4.3 TPC

The TPC performs 3-dimensional tracking and dE/dx-based particle identification for charged particles. The tracking system maintains a very low material budget and the total material in front of the calorimeters is less than 0.6 radiation length in almost all regions [20], which enables good calorimeter and PFA performance. The TPC consists of 220 layers, and 1 or 2 million $1 \times 6\,\mathrm{mm}^2$ pads in total. Then, a point resolution better than $100\,\mu$m for the complete drift region and a double hit resolution better than 2 mm are possible [20]. Three options for the the gas amplification systems are Micromegas [28], Gas Electron Multipliers (GEM) [29], and GridPix. The properties of the gas determine the drift velocity and the diffusion constant [7]. Layout of the TPC system is shown in Fig. 3.9.

3.4.4 ECAL

In order to perform PFA, ECAL and HCAL need to be highly-segmented, which leads to about 10^8 channels in total. ECAL identifies photons and measures their energy. It consists of 30 sensitive layers with tungsten absorber and a total thickness of 24 radiation lengths. The size of each readout pad is $5 \times 5\,\mathrm{mm}^2$. There are two choices for the ECAL: with silicon (SiECAL) or scintillator (ScECAL) readout as shown in Fig. 3.10 [7].

3.4.5 HCAL

The HCAL measures the energy of neutral hadrons. The HCAL is conceived as a sampling calorimeter having 48 sensitive layers with steel absorber. There are two choices for the HCAL: with $3 \times 3\,\mathrm{cm}^2$ scintillator tiles and SiPMs analog readout (analogue HCAL; AHCAL) or gaseous devices Glass Resistive Plate Chamber (GRPC) with $1 \times 1\,\mathrm{cm}^2$ cell geometries (semi-digital HCAL; SDHCAL) as active medium [7].

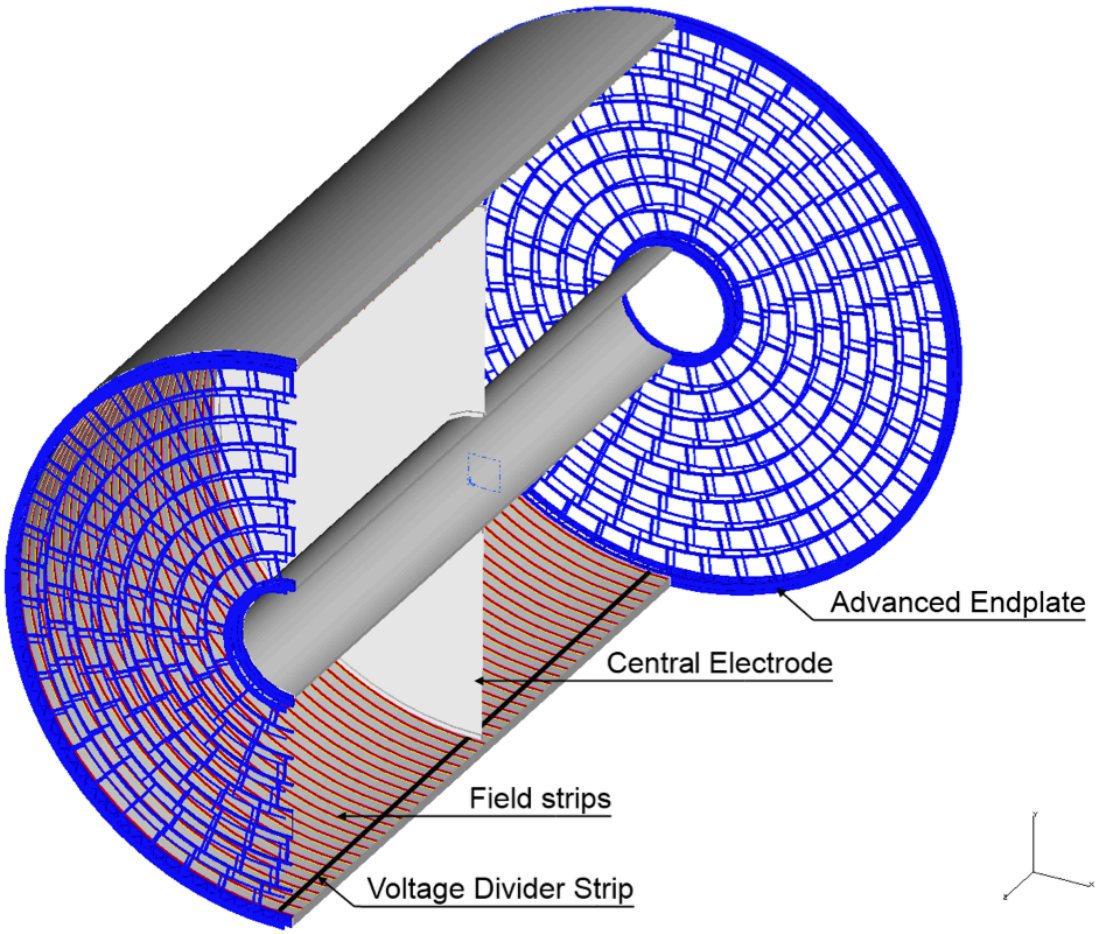

Figure 3.9: Layout of the TPC system (not to scale) [7].

3.4.6 Forward calorimetry

In the very forward region, three systems, LumiCal, BeamCal and LHCAL, are proposed. Their configuration is shown in Fig. 3.11. The luminosity is measured to 10^{-3} accuracy from low angle Bhabha scattering in the LumiCal at polar angles from 30 to 90 mrad. BeamCal in the region 5 to 30 mrad performs a bunch-by-bunch estimate of the luminosity and, supplemented by a pair monitor, assists beam tuning when included in a fast feedback system. LHCAL closes the coverage down to very small angles also for hadrons [9] [7]. These very forward detectors are based on similar technologies as the ECAL, taking into account the specific conditions of the forward region such as the harder radiation environment or the need for an improved compactness to identify electromagnetic showers in a high occupancy environment [20].

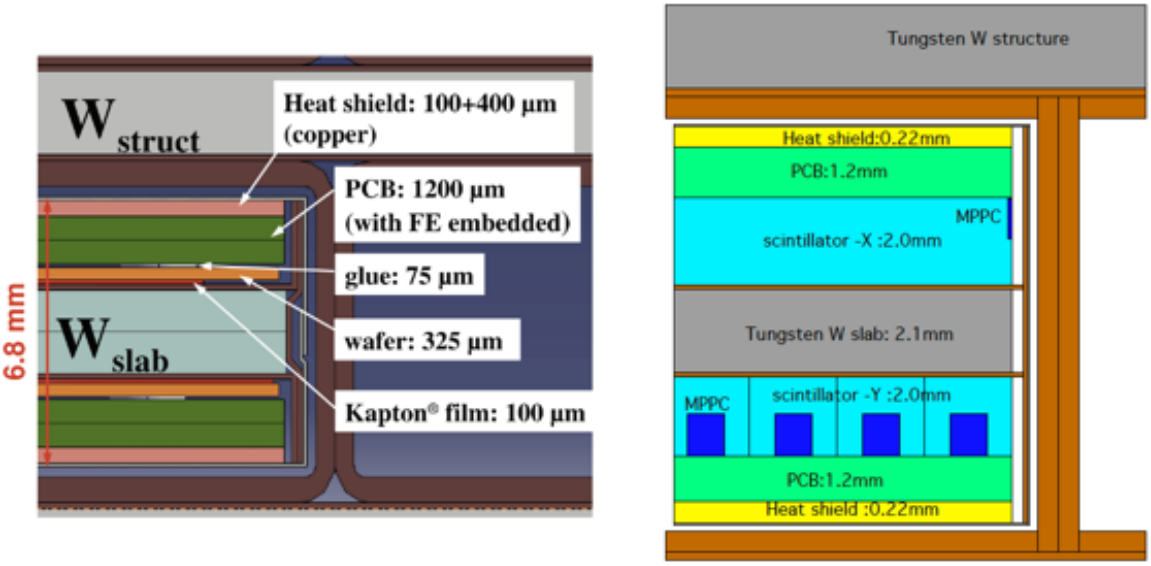

Figure 3.10: Cross sections through SiECAL layers (left) and ScECAL layers (right) [7].

3.4.7 ILD outer detector

A large volume superconducting coil surrounds the calorimeters, creating an axial B-field of nominally 3.5 to 4 tesla. An iron yoke returns the magnetic flux of the solenoid and, at the same time, serves as a muon filter, muon detector and tail catcher calorimeter [9]. The muon system/tail catcher instruments the iron return yoke in the barrel and in the forward region. Two main options are investigated for the sensitive layers, scintillator strips equipped with wave-length shifting fibers and read out with silicon photomultipliers (SiPM), or resistive plate chambers (RPC) [7].

3.4.8 IDR-L and IDR-S

In order to study whether similar performance can be achieved with a smaller detector, a simulation comparison of two ILD detectors was performed. One is the IDR-L model, which has the same structure as the previously proposed model. The other is the IDR-S model, which has a smaller TPC outer radius and a stronger magnetic field. The TPC outer radius is 177 cm and magnetic field is 3.5 tesla in IDR-L while TPC outer radius is 143 cm and magnetic field is 4 tesla in IDR-S [20], and their cross section is shown in Fig. 3.12. In Fig. 3.12, the length in z is the same, as is layout of inner detection.

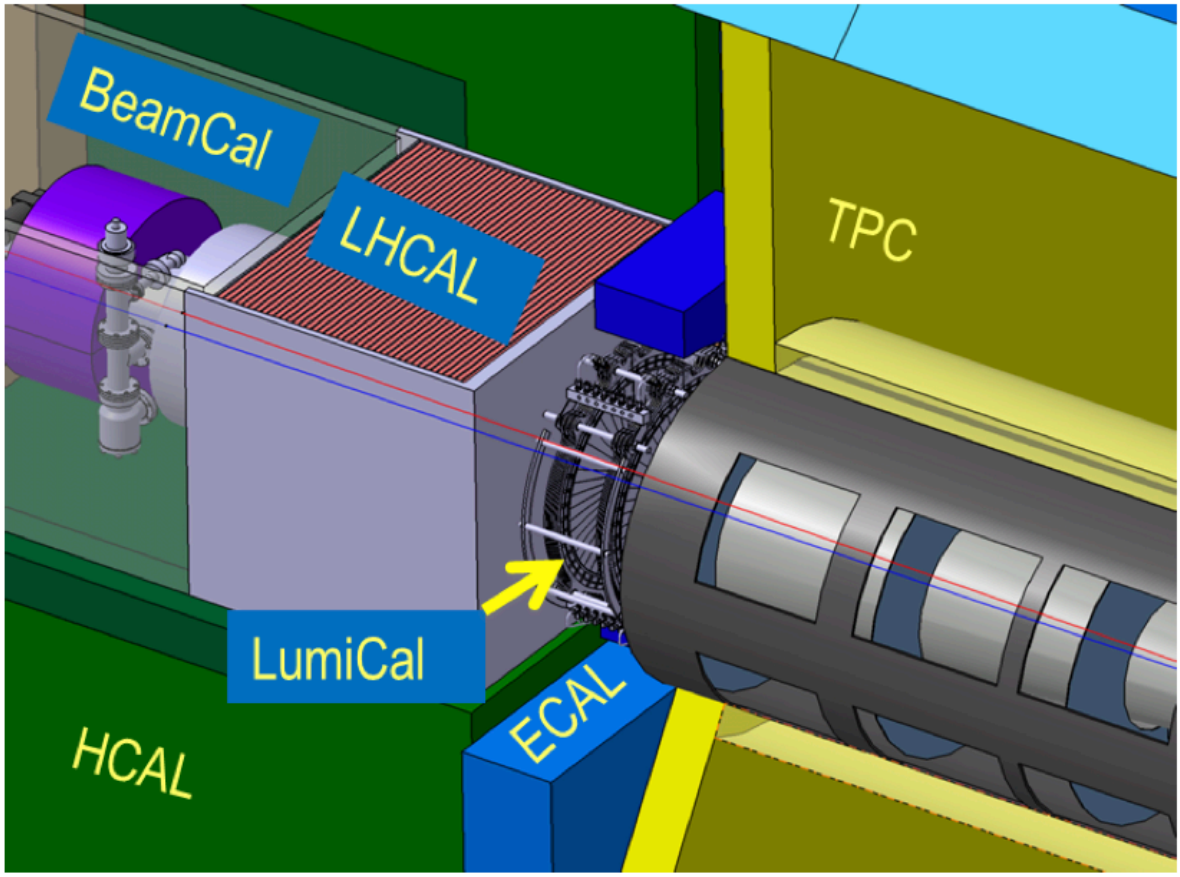

Figure 3.11: The very forward region of the ILD detector [7].

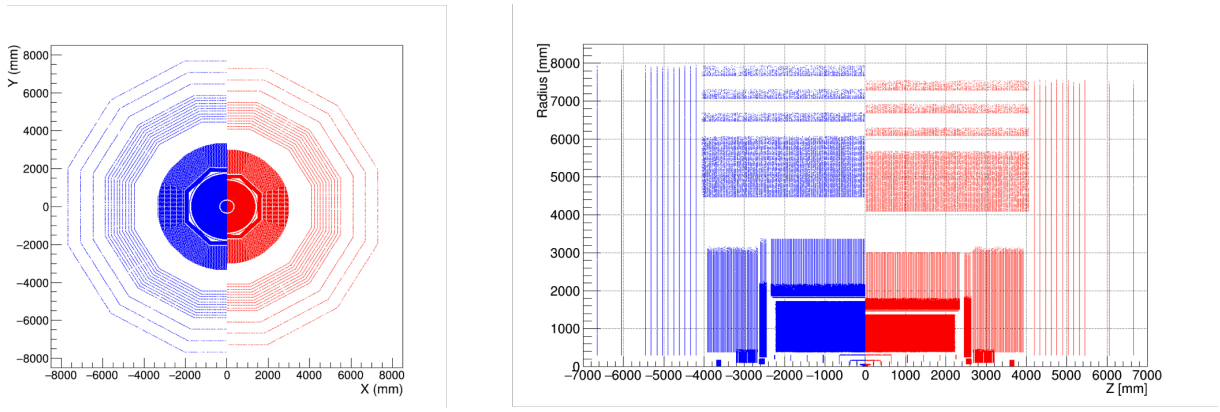

Figure 3.12: Cross section of the two ILD detector models: blue corresponds to IDR-L and red corresponds to IDR-S [30].

Chapter 4

Detector Simulation

iLCSoft is the common software framework for Linear Collider detector studies [31] [32]. In this software, LCIO provides a persistency framework that defines a data model for the studies [33]. It provides data classes for all phases of the event processing, starting from Monte Carlo truth information, continuing to generation of raw data and digitization, and to event reconstruction and analysis [9]. Marlin provides a C++ software framework for ILC software. Marlin uses the LCIO data model and can be used for all tasks that involve processing of LCIO files, *e.g.* reconstruction and analysis [34] [35].
DD4hep (Detector Description for HEP) is the common detector geometry description for iLCSoft [36]. It describes the detector geometries, materials and readout properties [9]. Interactions of generated particles with the detector material are simulated with a full detector simulator based on GEANT4 [37] to describe in detail detector geometries, materials and readout properties. Beamstrahlung and ISR effects are implemented. It implements the 14 mrad crossing angle, IP smearing and offset depending on initial particles.

Full sets of MC samples: "DBD", "IDR", and "mc-2020", were produced using various versions of iLCSoft. The DBD sample aims for physics study, while the IDR sample aims for detector optimization. Mc-2020 sample is new full set of high statistics 250 GeV MC samples for physics studies [38].
For detector optimization studies two ILD simulation models, ILD_l5_v02 (large) and ILD_s5_v02

Table 4.1: Properties of various full simulation samples [38]

	DBD (2013)	IDR (2019)	mc-2020 (2020)
Aim	Physics study	Detector opt.	Physics study
Ecm	$250\,(250\,\mathrm{fb}^{-1}), 350, 500\,\mathrm{GeV}, 1\,\mathrm{TeV}$	$500\,\mathrm{GeV}$	$250\,\mathrm{GeV}(1\,\mathrm{ab}^{-1})$
GEN sample	Whizard 1.95 stdhep	Re-use DBD sample	Whiard 2.8.5 slcio
Detector SIM	Mokka	DDSim	DDSim
iLCSoft	v01-16	v02-01	v02-02
Detector model		Hybrid CAL L5/S5	Hybrid CAL L5

(small) have been implemented using DD4hep. For simplicity, these two simulation models are referred to as IDR-L and IDR-S [20]. In the mc-2020 sample, detector model is ILD_l5_v02 only (not S5) and it uses a hybrid calorimeter. Especially in the o1 model, calorimeters are Si-ECAL and AHCAL.

In a first step, large generator samples of e^+e^- events are created with the Whizard event generator [39]. Whizard uses tree-level matrix elements to generate events with the final state

quarks and leptons based on a realistic beam energy spectrum, the so-called hard sub-process. The parton-showering, fragmentation, and hadronization into the visible final stable or quasi-stable state is performed with Pythia [9]. Pythia is also used for particle decay [7].
The two dominating effects of the strong beam-beam interactions are beamstrahlung, leading to a collision energy distribution (luminosity spectrum) with a lower tail, and the creation of incoherent e^+e^- pairs that are a potential source of the beam-induced background at the ILC. Another source of background at the ILC is $\gamma\gamma \rightarrow hadrons$ events, due to ISR or beamstrahlung photons. These effects are implemented by Guinea-Pig and Pythia.
After having reconstructed all the individual particles in the event, the output of the detailed full simulations with GEANT4 stores the deposited energy in the sensitive detector elements together with the position and pointers to the MCParticle that created the energy deposition. These hits are digitized in dedicated Marlin processors taking into account all relevant effects from the detector and the readout electronics [20]. Simulated detector signals consisting of tracker hits and energy deposits in segmented calorimeter cells are passed through a chain of realistic event reconstruction programs that include track finding and fitting in trackers, cluster finding in calorimeters and linking to a corresponding charged particle track using PandoraPFA [8]. Then LCFIPlus executes the following algorithms: high-purity vertex finders for the reconstruction of primary and secondary vertices; a jet finder optimized for reconstruction of heavy flavor jets; and multivariate analysis for flavor identification based on the TMVA package [40]. The actual jet clustering is then performed by using a clustering with a Durham-like algorithm [20]. The Durham algorithm compares

$$y_{ij} = \frac{min(E_i^2, E_j^2)(1 - \cos\theta_{ij})}{E_{vis}^2} \tag{4.1}$$

for all particle pairs in the simulation and chooses the pair with smallest y_{ij}. Then combine 4-momenta of the pair to regard the pair as one particle. This merging is continued until the value y_{ij} reaches to the defined threshold value y_{cut}. The final clusters are defined as jets [41].

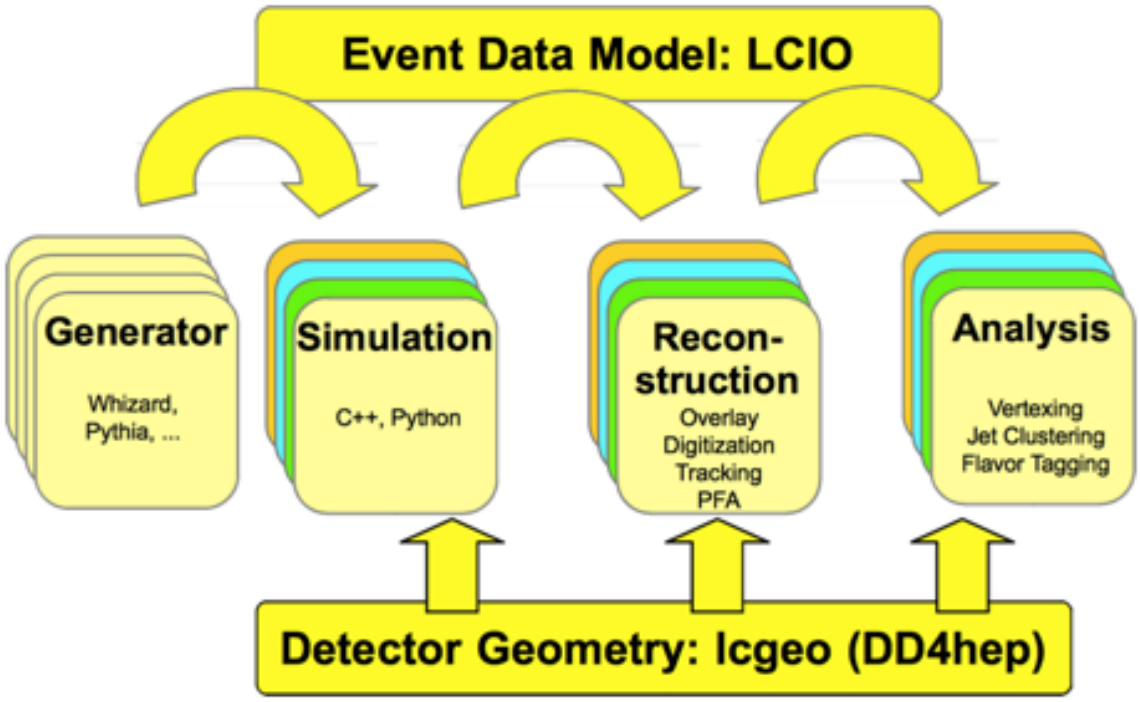

Figure 4.1: The flow of the simulation [42].

Part II

Photon Energy Calibration

This part will focus on the photon energy calibration. We will introduce our calibration methods in detail in Section 5. Event simulation and selection will be explained in Sections 6 and 7. Results will be given in Section 8. This part focuses on detector performance benchmarking. The performance of the photon energy calibration for two detector models, IDR-L having a larger TPC outer radius and IDR-S having a smaller TPC outer radius [20], will be evaluated.

Chapter 5

Photon Energy Calibration Methods

The signal channel used here is $e^+e^- \to \gamma Z, Z \to \mu^+\mu^-$. The energy of the final-state photon is approximately 241.7 GeV at $\sqrt{s} = 500$ GeV if there is neither beamstrahlung nor additional ISR.

The energy of photon can be reconstructed using four-momentum conservation from the mea-

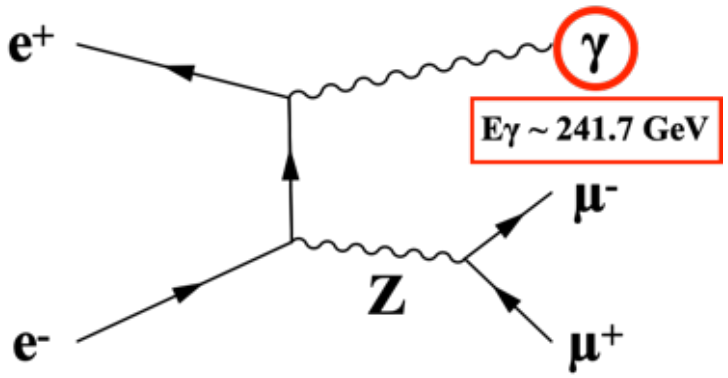

Figure 5.1: Signal channel $e^+e^- \to \gamma Z$, $Z \to \mu^+\mu^-$.

sured direction angles of μ^+, μ^-, and γ, or the measured energies of μ^+, μ^- in addition. The following five methods are considered to reconstruct the photon energy: "Method 1", "Method 2", "Method 3", "Method 4", and "Method 4′". The muon mass is neglected everywhere in the following.

Method 1 uses measured $\{\theta_{\mu^-}, \theta_{\mu^+}, \theta_\gamma, \phi_{\mu^-}, \phi_{\mu^+}, \phi_\gamma\}$ as inputs to determine $\{E_{\mu^-}, E_{\mu^+}, E_\gamma\}$. This method ignores beamstrahlung and additional ISR and beam crossing angles. Then four-momentum conservation requires the following equations:

$$\begin{cases} E_{\mu^-} + E_{\mu^+} + E_\gamma = 500 \\ E_{\mu^-} \sin\theta_{\mu^-} \cos\phi_{\mu^-} + E_{\mu^+} \sin\theta_{\mu^+} \cos\phi_{\mu^+} + E_\gamma \sin\theta_\gamma \cos\phi_\gamma = 0 \\ E_{\mu^-} \sin\theta_{\mu^-} \sin\phi_{\mu^-} + E_{\mu^+} \sin\theta_{\mu^+} \sin\phi_{\mu^+} + E_\gamma \sin\theta_\gamma \sin\phi_\gamma = 0 \\ E_{\mu^-} \cos\theta_{\mu^-} + E_{\mu^+} \cos\theta_{\mu^+} + E_\gamma \cos\theta_\gamma = 0. \end{cases} \tag{5.1}$$

Method 2 uses measured $\{\theta_{\mu^-}, \theta_{\mu^+}, \theta_\gamma, \phi_{\mu^-}, \phi_{\mu^+}, \phi_\gamma\}$ as inputs to determine $\{E_{\mu^-}, E_{\mu^+}, E_\gamma, E_{ISR} = |P_{ISR}|\}$. This method considers beamstrahlung and additional ISR, however the beam crossing

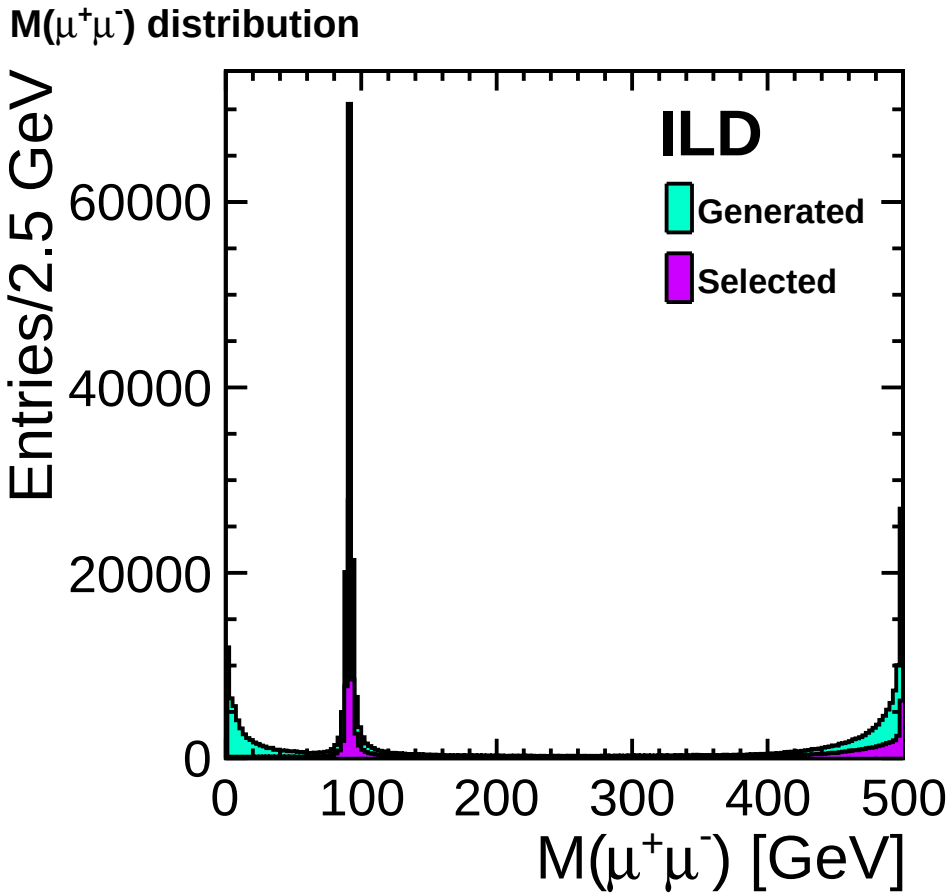

Figure 5.2: Invariant mass distribution of $\mu^-\mu^+$ pair for Large ILD (IDR-L) model samples with $e_L^- e_R^+$ polarization

Invariant mass distribution of $\mu^-\mu^+$ pair for Large ILD (IDR-L) model samples with $e_L^- e_R^+$ polarization.

angle is not considered. Then four-momentum conservation requires the following equations:

$$\begin{cases} E_{\mu^-} + E_{\mu^+} + E_\gamma + |P_{ISR}| = 500 \\ E_{\mu^-} \sin\theta_{\mu^-} \cos\phi_{\mu^-} + E_{\mu^+} \sin\theta_{\mu^+} \cos\phi_{\mu^+} + E_\gamma \sin\theta_\gamma \cos\phi_\gamma = 0 \\ E_{\mu^-} \sin\theta_{\mu^-} \sin\phi_{\mu^-} + E_{\mu^+} \sin\theta_{\mu^+} \sin\phi_{\mu^+} + E_\gamma \sin\theta_\gamma \sin\phi_\gamma = 0 \\ E_{\mu^-} \cos\theta_{\mu^-} + E_{\mu^+} \cos\theta_{\mu^+} + E_\gamma \cos\theta_\gamma + P_{ISR} = 0. \end{cases} \tag{5.2}$$

Method 3 uses $\{\theta_{\mu^-}, \theta_{\mu^+}, \theta_\gamma, \phi_{\mu^-}, \phi_{\mu^+}, \phi_\gamma\}$ as inputs to determine $\{E_{\mu^-}, E_{\mu^+}, E_\gamma, E_{ISR}\}$. This method considers the beam crossing angle in addition to *Method* 2. Then four-momentum conservation requires the following equations:

$$\begin{cases} E_{\mu^-} + E_{\mu^+} + E_\gamma + |P_{ISR}| = 500 \\ E_{\mu^-} \sin\theta_{\mu^-} \cos\phi_{\mu^-} + E_{\mu^+} \sin\theta_{\mu^+} \cos\phi_{\mu^+} + E_\gamma \sin\theta_\gamma \cos\phi_\gamma + |P_{ISR}| \sin\alpha = 500 \sin\alpha \\ E_{\mu^-} \sin\theta_{\mu^-} \sin\phi_{\mu^-} + E_{\mu^+} \sin\theta_{\mu^+} \sin\phi_{\mu^+} + E_\gamma \sin\theta_\gamma \sin\phi_\gamma = 0 \\ E_{\mu^-} \cos\theta_{\mu^-} + E_{\mu^+} \cos\theta_{\mu^+} + E_\gamma \cos\theta_\gamma \pm |P_{ISR}| \cos\alpha = 0, \end{cases} \tag{5.3}$$

where 2α is defined as the crossing angle.

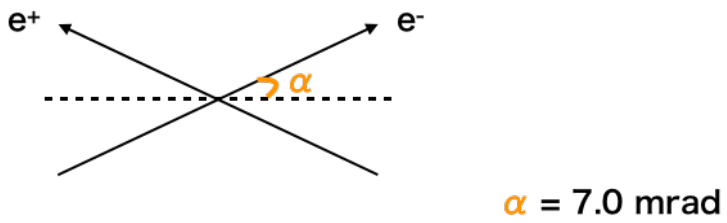

Figure 5.3: Definition of α.

Method 4 uses measured $\{\theta_{\mu^-}, \theta_{\mu^+}, \theta_\gamma, \phi_{\mu^-}, \phi_{\mu^+}, \phi_\gamma, E_{\mu^-}, E_{\mu^+}\}$ as inputs to determine $\{E_\gamma, E_{ISR}\}$, *i.e.* energies of muons are used as inputs in addition to *Method* 3. Then energy and longitudinal momentum conservations require the following equations:

$$\begin{cases} E_{\mu^-} + E_{\mu^+} + E_\gamma + |P_{ISR}| = 500 \\ E_{\mu^-}\cos\theta_{\mu^-} + E_{\mu^+}\cos\theta_{\mu^+} + E_\gamma\cos\theta_\gamma \pm |P_{ISR}|\cos\alpha = 0. \end{cases} \tag{5.4}$$

In Method 4′, the following formulae are used while inputs and outputs are the same as Method 4, *i.e.* measured $\{\theta_{\mu^-}, \theta_{\mu^+}, \theta_\gamma, \phi_{\mu^-}, \phi_{\mu^+}, \phi_\gamma, E_{\mu^-}, E_{\mu^+}\}$ are used to determine $\{E_\gamma, E_{ISR}\}$. Then energy and y component of momentum conservations require the following equations:

$$\begin{cases} E_{\mu^-} + E_{\mu^+} + E_\gamma + |P_{ISR}| = 500 \\ E_{\mu^-}\sin\theta_{\mu^-}\sin\phi_{\mu^-} + E_{\mu^+}\sin\theta_{\mu^+}\sin\phi_{\mu^+} + E_\gamma\sin\theta_\gamma\sin\phi_\gamma = 0. \end{cases} \tag{5.5}$$

In this method, the photon energy can be determined without considering P_{ISR} at all, though there are singularities at $\sin\theta_\gamma = 0$ and at $\sin\phi_\gamma = 0$, where the equations become unsolvable. Performances of the five methods will be compared in Section **??**.

Chapter 6

Simulation Setup

In this part, signal events, $e^+e^- \to \gamma Z, Z \to \mu^+\mu^-$, are first generated using Whizard 1.95 [39]. The whole set of programs used in this analysis is packaged as iLCSoft version v02-00-02 [31]. The event simulation for this analysis has been done at the center-of-mass energy of 500 GeV for both IDR-L and IDR-S.

Chapter 7

Event Selection

Signatures of the signal events are a $\mu^+\mu^-$ pair which has an invariant mass consistent with the Z boson mass and one energetic isolated photon. In the analysis, we used the IsolatedLepton-Tagging processor to identify muons and require a pair of oppositely charged muons [9][1]. After this selection, events from the three diagrams shown in Fig. 7.1 remain, as well as $\mu^+\mu^-$ events without final-state photons.

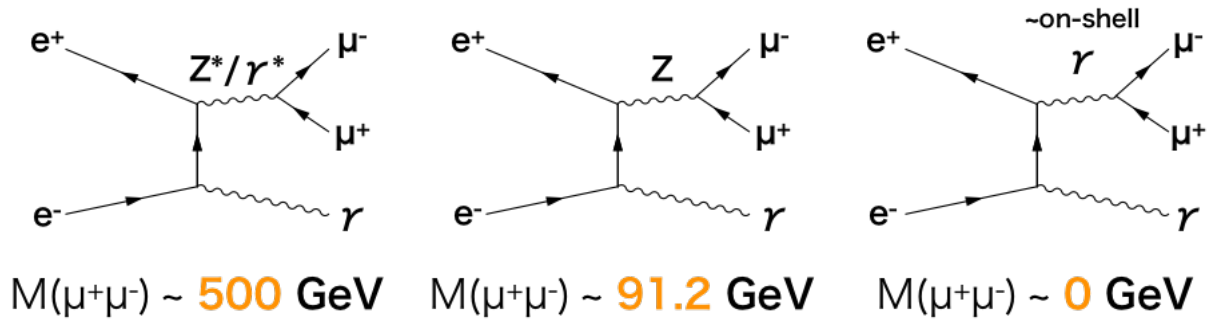

Figure 7.1: Three diagrams in process $e^+e^- \to \gamma Z$, $Z \to \mu^+\mu^-$.

In order to select the radiative return events, the invariant mass of the two muons $M(\mu^+\mu^-)$ is required to satisfy $|M(\mu^+\mu^-) - M_Z| < 10\,\text{GeV}$, where M_Z is the nominal Z boson mass of 91.19 GeV. Then, events with at least one isolated photon are selected. The photon is identified using Photon ID by PandoraPFA[2]. The photon energy is required to be more than 50 GeV. The photon whose energy is closest to the expected value, *i.e.* 241.7 GeV, is selected and all photons inside the cone with opening angle $\cos^{-1}(0.95)$ around the direction of the photon are merged. Owing to the beamstrahlung and ISR effects, the photon energy spectrum has a long downward tail from its peak at 241.7 GeV, as shown in Fig. 7.2.

[1]The key algorithm, implemented based on multivariate analysis, is to distinguish the isolated leptons and the leptons in jets, by looking at the energies within two cones around the leptons.

[2]PandoraPFA provides its own algorithms for identifying various particles including photons based on the information of tracks and calorimeter clusters which are associated with each particle-flow object (PFO).

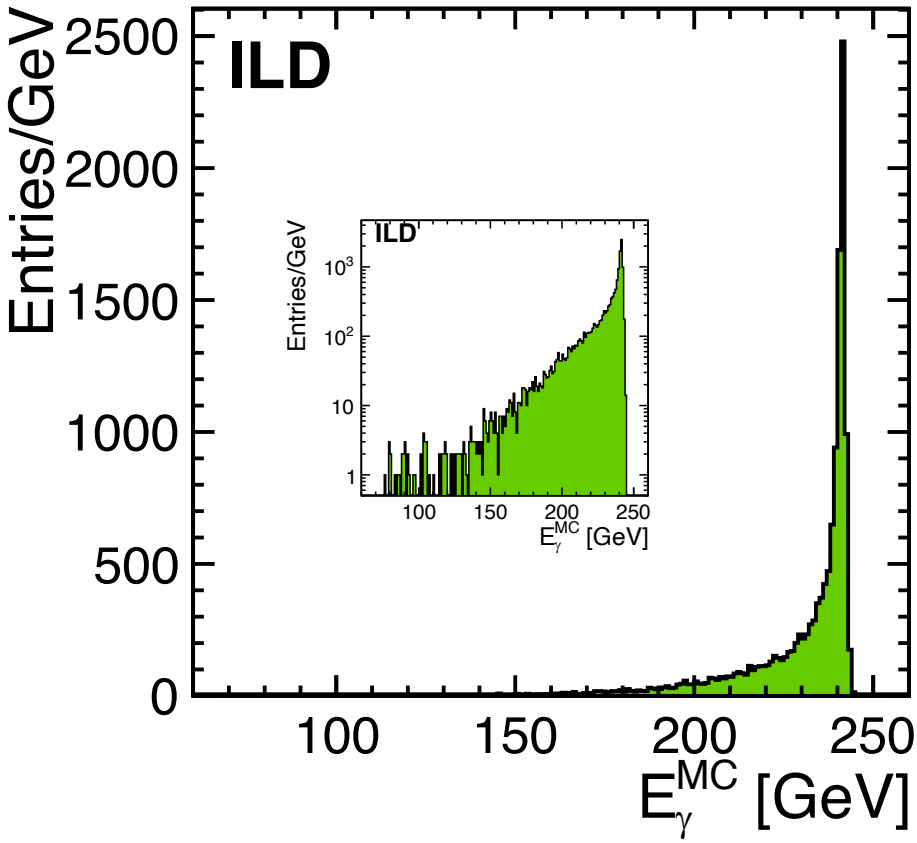

Figure 7.2: MC truth photon energy distribution for the selected events.

Chapter 8

Results

8.1 Comparison of the five methods

The photon energy is kinematically reconstructed for each of the selected events using the five methods explained in Section 5. The relative difference of the reconstructed photon energy from its MC truth, $\frac{(E_\gamma - E_\gamma^{MC})}{E_\gamma^{MC}}$, is shown in Fig. 8.1. As shown, Method $4'$ has the best resolution and small, symmetric tails. We hence decided to use Method $4'$ to calibrate the photon energy in what follows. Notice that in Method $4'$, the photon energy can be determined without solving for P_{ISR}. To demonstrate the validity of Method $4'$, the reconstructed ISR energy $|P_{ISR}|$ by Method $4'$ is compared to the MC truth. They are consistent as shown in Fig. 8.2. Hereafter Method $4'$ is referred to as the Angular Method (sometimes abbreviated as "Ang. Method" hereafter).

8.2 Photon Energy Calibration

In general, because of various detector effects, the photon energy measured in the ECAL might be biased and requires calibration. In this section, we will demonstrate how an energy calibration can be performed using the Angular Method introduced above. The measured photon energy given by PandoraPFA in our current MC samples has a slight systematic upward shift for high energy photons as seen in Fig. 8.3, which shows the relative differences from the MC truth for the measured (PFO) and kinematically reconstructed (Angular Method) photon energies. The central value of the PFO photon energy distribution is $\sim 1.8\,\%$ off the MC truth, while the bias in the kinematically reconstructed photon energy by the Angular Method is $< 0.05\,\%$. The bias in the PFO photon energy depends on the polar angle as shown in Fig. 8.4. To correct this angle-dependent systematic shift, we introduce the following angle-dependent calibration factor:

$$f(|\cos\theta_\gamma|) = \frac{\langle E_{\gamma,\text{Angular Method}}(|\cos\theta_\gamma|)\rangle}{\langle E_{\gamma,\text{PFO}}(|\cos\theta_\gamma|)\rangle} \tag{8.1}$$

for each of the 20 $|\cos\theta_\gamma|$ bins, where the angled brackets represent mean values of the distributions of quantities in the brackets as obtained from Gaussian fits. Using this calibration factor, we rescale the photon energy from PandoraPFA bin-by-bin as

$$E_{\gamma,\text{PFO,Corr.}}(|\cos\theta_\gamma|) = f(|\cos\theta_\gamma|) \times E_{\gamma,\text{PFO}}(|\cos\theta_\gamma|). \tag{8.2}$$

Figure 8.5 is the same figure as Fig. 8.3 but additionally with the calibrated PFO photon energy distribution. We can see that the above calibration procedure removes the overall bias in the

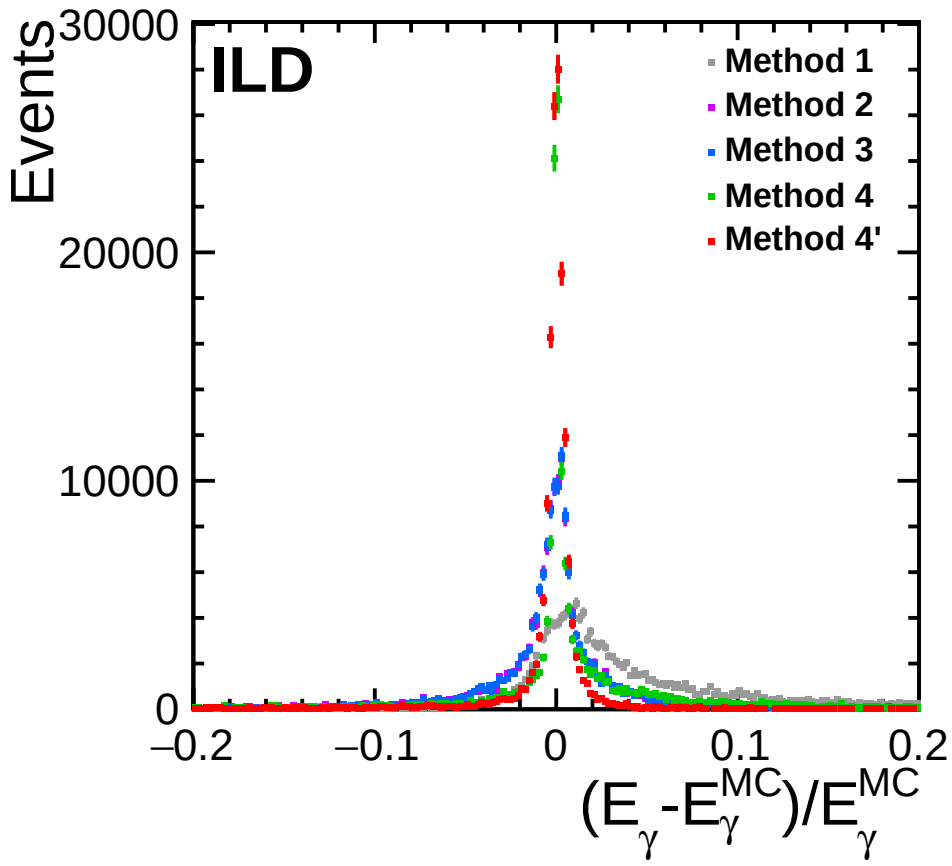

Figure 8.1: The relative difference of the reconstructed photon energy from its MC truth for the five methods. Some of the points from Method 2 are underneath those from Method 3.

raw PFO photon energy. We can also see that the photon energy resolution by the Angular Method is much better than that of the PFO. It is ensured that the expected photon energy calibration uncertainty by the Angular Method will not be limited by the remaining bias and finite resolution of photon energy obtained with the method itself. It will be limited instead by the statistics of signal events and intrinsic ECAL resolution. Though here we calibrated the photon energy only as a function of $|\cos\theta_\gamma|$, in principle we can also use the same calibration procedure as a function of other variables like ϕ_γ or E_γ. To make sure that this correction procedure also works at different photon energies, we looked at the relative difference from the MC truth for the measured photon energy after the correction as a function of photon energy (see Fig. 8.6). The mean value is calibrated to about 0.1 % for photon energies above 120 GeV.

8.3 Energy Scale Uncertainty After Calibration

In the previous section, we demonstrated that the measured photon energy can be calibrated using the Angular Method. In this section, we will investigate the calibration uncertainty expected at the ILC. In order to see how the detector design affects the photon energy calibration, we will evaluate the calibration uncertainty for each of the two detector models, IDR-L and

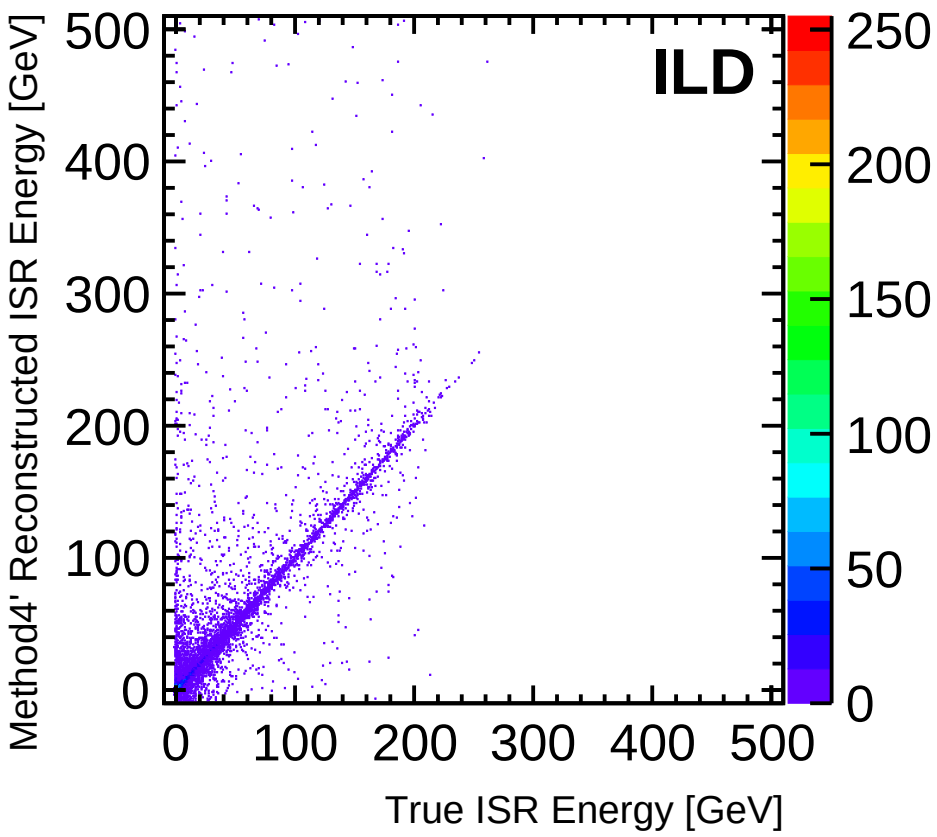

Figure 8.2: Reconstructed ISR energy and MC truth by Method 4′.

IDR-S.

First, sigma values, *i.e.* relative photon energy resolutions, from Gaussian fits to the distributions of the relative difference from the MC truth are compared between measured (PFO) and kinematically reconstructed (Angular Method) photon energies so as to demonstrate the validity of the Angular Method. The dependence of the sigma values on $|\cos\theta_\gamma|$, ϕ_γ, and E_γ will be discussed. Figure 8.7 shows the $|\cos\theta_\gamma|$ dependence. The photon energy resolution of the Angular Method gets worse at large $|\cos\theta_\gamma|$ reflecting the existence of the singularity at $\sin\theta_\gamma = 0$. In each detector model, the kinematically reconstructed photon energy by the Angular Method has a better resolution than the measured PFO energy for $|\cos\theta_\gamma| < 0.95$. This result demonstrates the effectiveness of the photon energy calibration using the Angular Method for $|\cos\theta_\gamma| < 0.95$. The resolutions of kinematically reconstructed photon energies for IDR-L and IDR-S are slightly different. IDR-L is better for $|\cos\theta_\gamma| < 0.9$, but IDR-S is better for $|\cos\theta_\gamma| > 0.9$. As described in Section 15., IDR-L and IDR-S have different TPC outer radii and hence ECAL outer radii as well. Therefore, the different performance could be due to the different momentum resolution for muons or different photon angle resolution, or both. To identify what dominantly determines the performance, plots similar to Fig. 8.7 are made using cheated (MC truth) photon angles in the Angular Method in Fig. 8.8 and cheated (MC truth) muon momenta in the Angular Method in Fig. 8.9, respectively. Figure 8.8 shows no difference, indicating that the angle resolution effect is

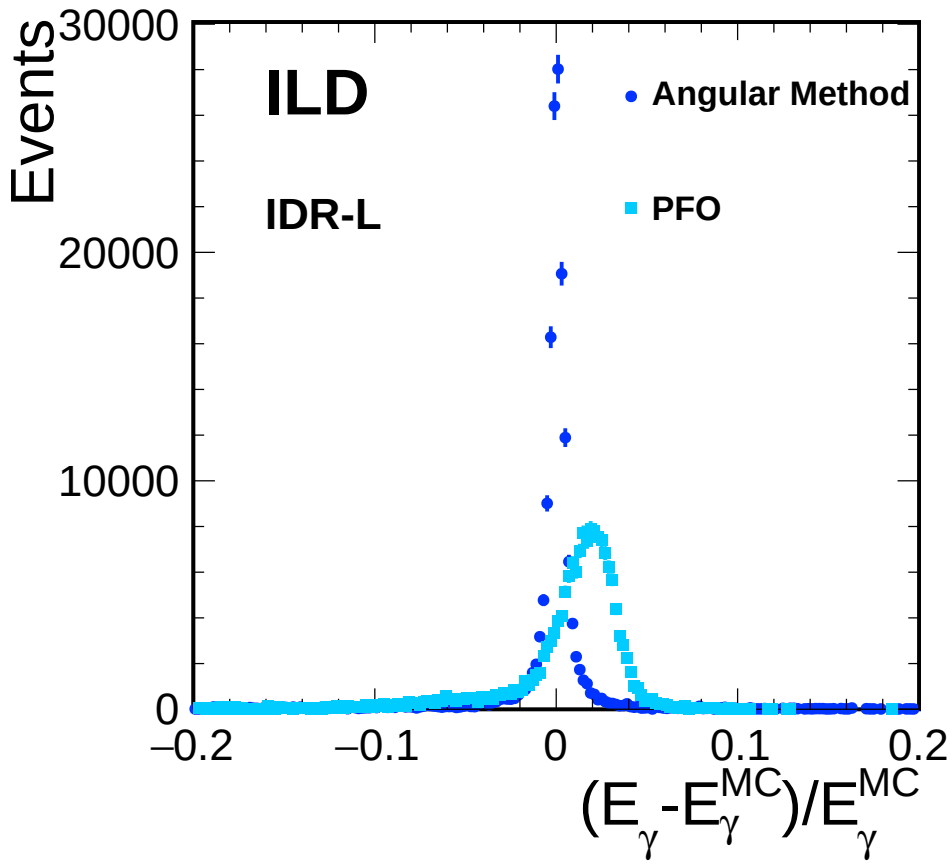

Figure 8.3: The comparison of relative differences from the MC truth for measured (PFO: light blue) and kinematically reconstructed (Angular Method: blue) photon energies for IDR-L model. To avoid singularities in the Angular Method at $\phi_\gamma = 0$ and $\theta_\gamma = 0$, measured photon angles are restricted to $|\sin\phi_\gamma| \geq 0.1$ and $|\cos\theta_\gamma| \leq 0.95$ in this plot.

negligible. When muon momenta are cheated, the photon energy resolution becomes very small, less than 0.005 %, suggesting that the kinematically reconstructed photon energy resolution is dominated by the muon momentum resolution. As the muon momentum resolution for IDR-L is better than that for IDR-S at low $|\cos\theta_\gamma|$ values and worse at high $|\cos\theta_\gamma|$ values, the kinematically reconstructed photon energy resolution shows a similar behavior. The point-to-point fluctuation in the PFO energy resolution can be attributed to the ECAL structure: there is a gap between the barrel part and the endcap part of ECAL and that the barrel part is segmented into five (if folded at $z = 0$ as Fig. 8.7, then three) blocks in the z-direction.

The ϕ_γ dependence is shown in Fig. 8.10. The effect of the singularity at $\sin\phi_\gamma = 0$, *i.e.* $\phi_\gamma = 0$ and $\pm\pi$ is seen as degradation in the resolution of the photon energy reconstructed by the Angular Method. In each detector model, the photon energy reconstructed by the Angular Method has a better resolution than the PFO photon energy, although it is degraded towards $\sin\phi_\gamma = 0$. This result demonstrates the effectiveness of the photon energy calibration by the Angular Method for $\frac{\pi}{40} < |\phi_\gamma| < \frac{39\pi}{40}$ *i.e.* $|\sin\phi_\gamma| > 0.078$. The large fluctuations of the PFO energy resolution seen in the figure are due to the ECAL structure having an eight-fold symmetry

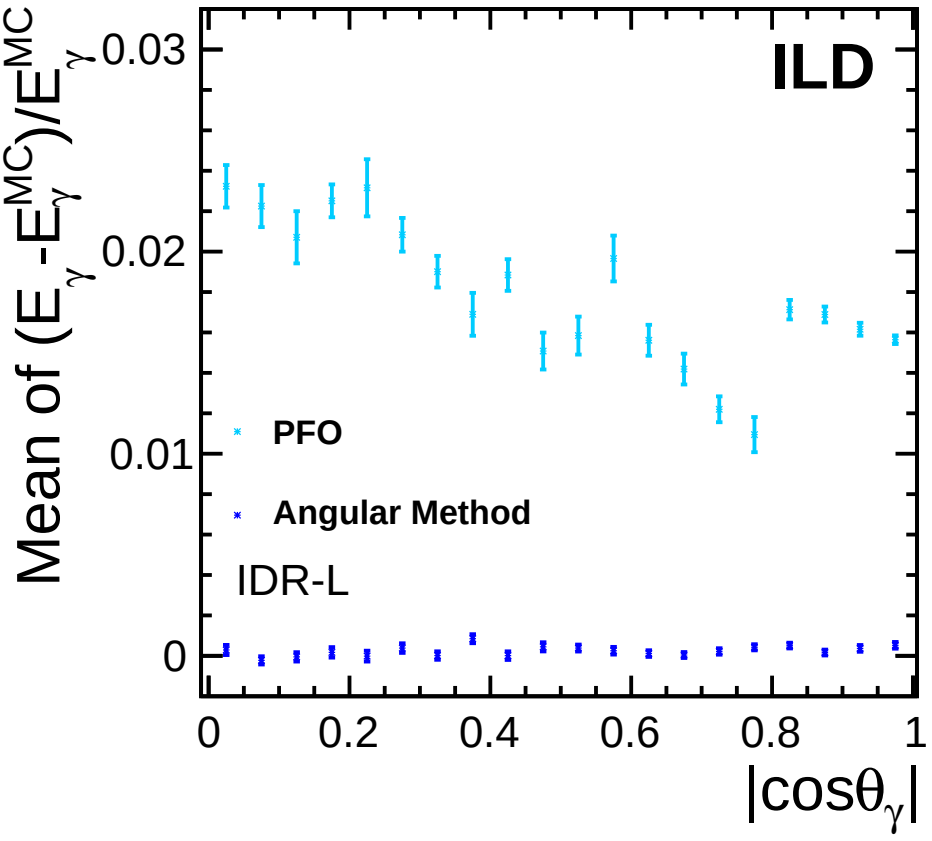

Figure 8.4: Mean value of a Gaussian fit to the relative difference from the MC truth as a function of $|\cos\theta_\gamma|$ for each of measured (PFO: light blue) and kinematically reconstructed (Angular Method: blue) photon energies for the IDR-L model. Photon energy range is not restricted and to avoid singularities in the Angular Method at $\phi_\gamma = 0$, measured photon angles are restricted to $|\sin\phi_\gamma| \geq 0.1$ in this plot.

as shown in Fig. 8.11.

Finally, we now examine the energy dependence of the photon energy resolution. Figure 8.12 shows the E_γ dependence. The photon energy kinematically reconstructed by the Angular Method has a constant resolution of $\sim 0.4\,\%$ for $120\,\text{GeV} \lesssim E_\gamma \lesssim 260\,\text{GeV}$ significantly smaller than the PFO photon energy resolution for both IDR-L and IDR-S. Notice also here that the PFO photon energy resolution is roughly consistent with the ECAL design resolution of $\frac{\sigma_E}{E} = \frac{17}{\sqrt{E[\text{GeV}]}} \oplus 1\,\%$ [7]. In summary, Figures 8.7, 8.10, and 8.12 demonstrated that the photon energy kinematically reconstructed by the Angular Method has a better resolution than the PFO photon energy, except in the singular regions near $\sin\phi_\gamma = 0$ and $|\cos\theta_\gamma| = 1$, and therefore can be used to calibrate the PFO photon energy.

Overall the photon energy scale uncertainty for this calibration can be estimated using the

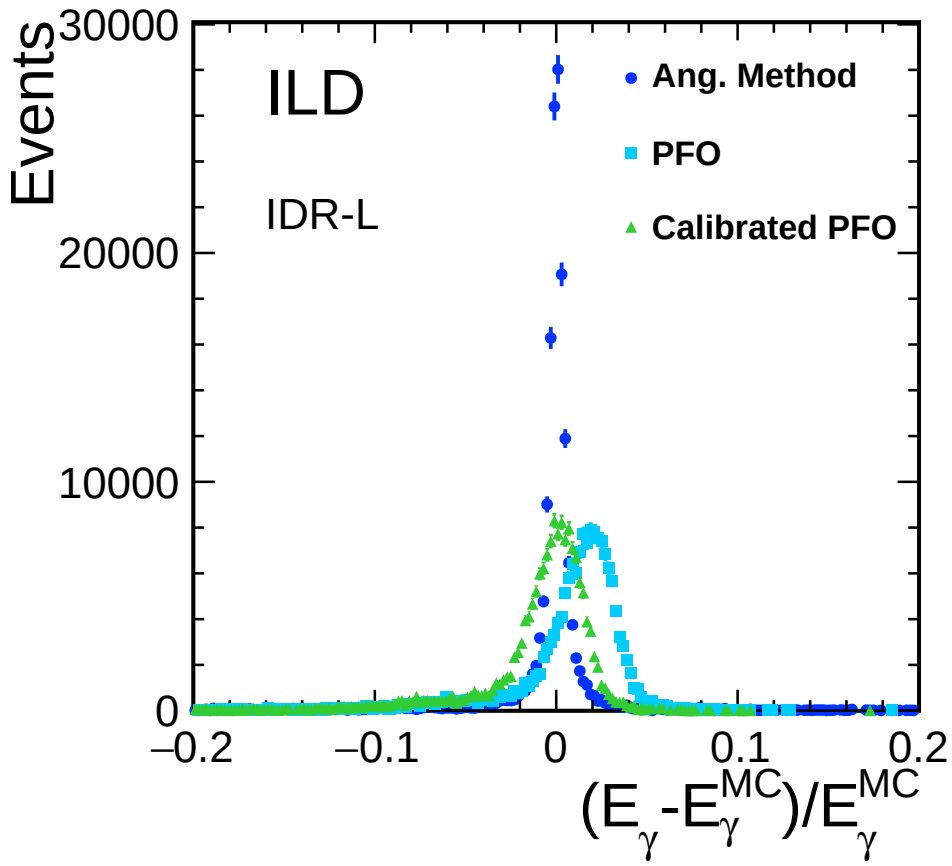

Figure 8.5: The same figure as Fig. 8.3 but additionally with the calibrated PFO photon energy (green) distribution.

following equation:

$$E_\gamma \text{ Scale Uncertainty} = \sqrt{(\text{PFO Energy Uncertainty})^2 + (\text{Ang. Method Uncertainty})^2}$$

$$\text{Energy Uncertainty} = \frac{\text{Sigma of } \frac{(E_\gamma - E_\gamma^{MC})}{E_\gamma^{MC}} \text{ distribution}}{\sqrt{\text{Number of events}}}.$$

The photon energy scale uncertainty calculated this way is shown in Fig. 8.13. The figure shows that the photon energy scale uncertainty is below 80 MeV for $E_\gamma \sim 120$ GeV decreasing to 15 MeV for $E_\gamma \sim 250$ GeV.

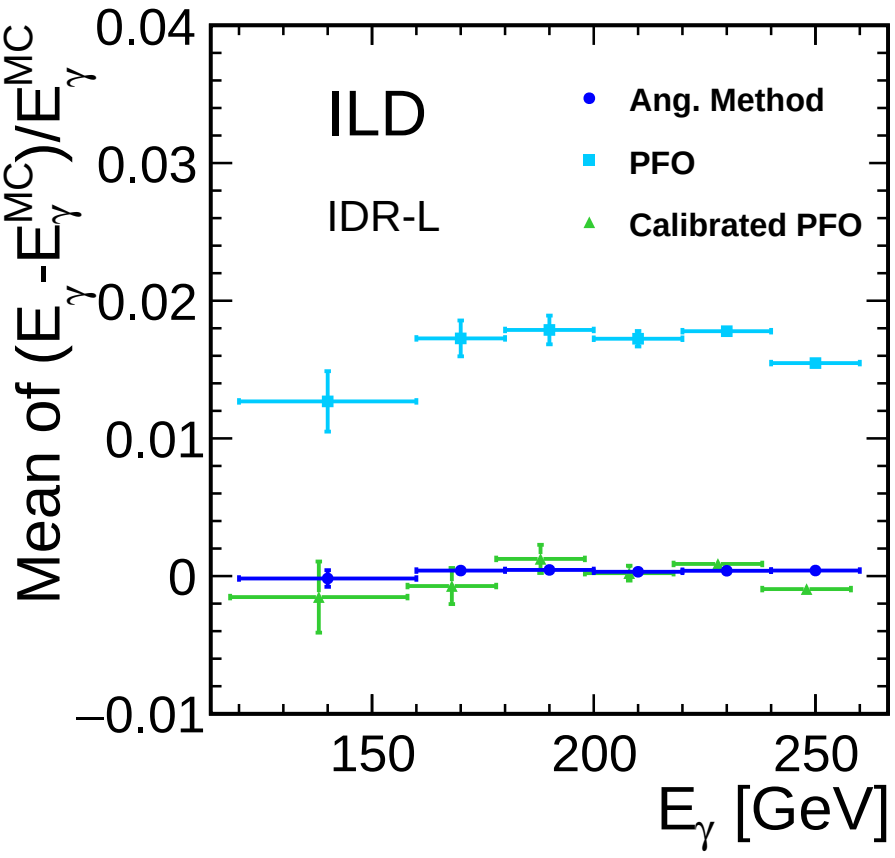

Figure 8.6: Mean value of a Gaussian fit to the relative difference from the MC truth as a function of photon energy for each of measured (PFO: light blue) and kinematically reconstructed (Angular Method: blue) and calibrated (Calibrated PFO: green) photon energies for IDR-L model. To avoid singularities in the Angular Method at $\phi_\gamma = 0$ and $\theta_\gamma = 0$, measured photon angles are restricted to $|\sin\phi_\gamma| \geq 0.1$ and $|\cos\theta_\gamma| \leq 0.95$ in this plot.

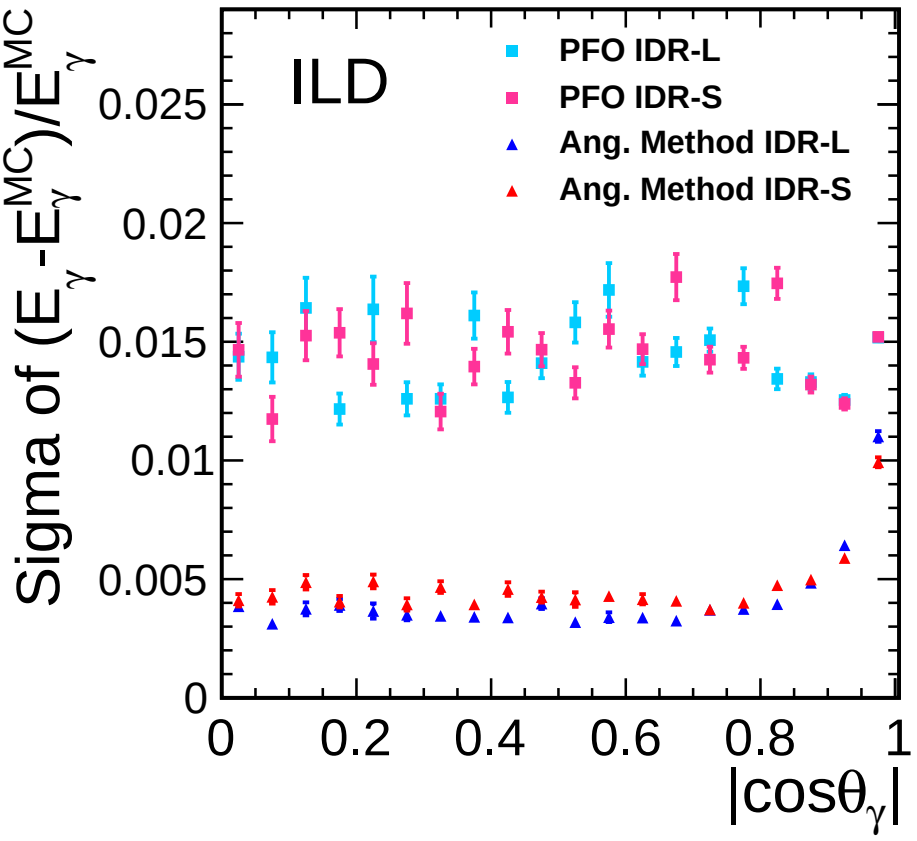

Figure 8.7: Sigma value from a Gaussian fit to the distribution of the relative difference from the MC truth as a function of $|\cos\theta_\gamma|$ for each of measured (PFO IDR-L: light blue, PFO IDR-S: magenta) and kinematically reconstructed photon energies (Angular Method IDR-L: blue, Angular Method IDR-S: red). Only photons satisfying $|\sin\phi_\gamma| \geq 0.1$ are included in this plot.

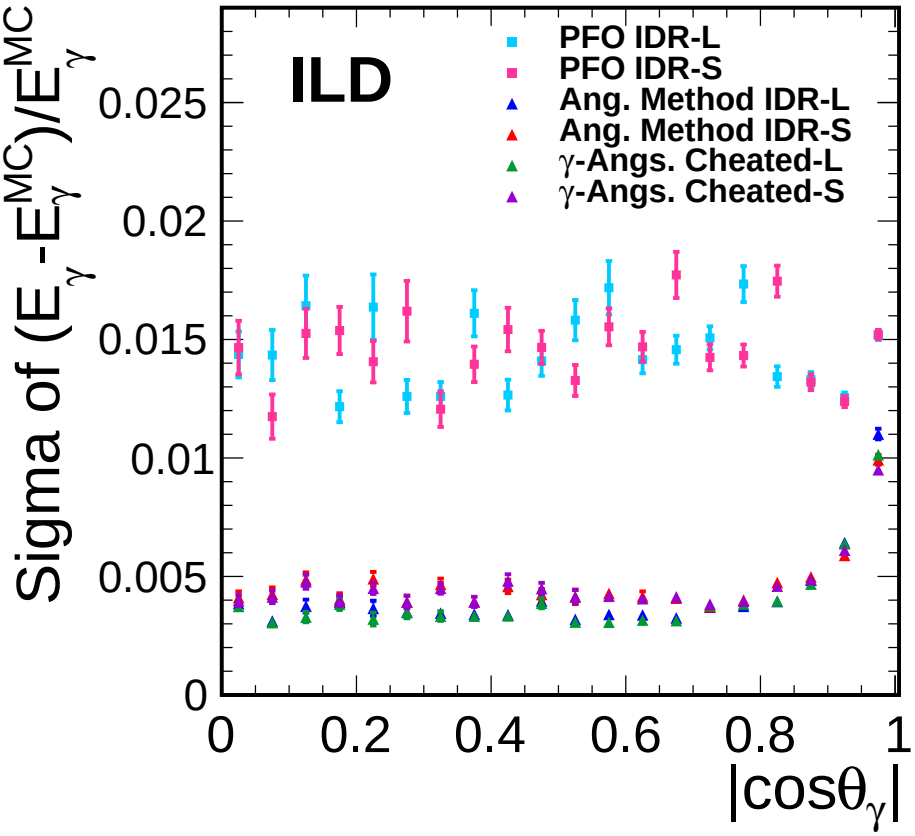

Figure 8.8: Similar plot to Fig. 8.7 but with additionally the sigma value for kinematically reconstructed photon energies cheating photon angles for IDR-L (γ-Angs. Cheated-L: Green) and for IDR-S (γ-Angs. Cheated-S: Violet).

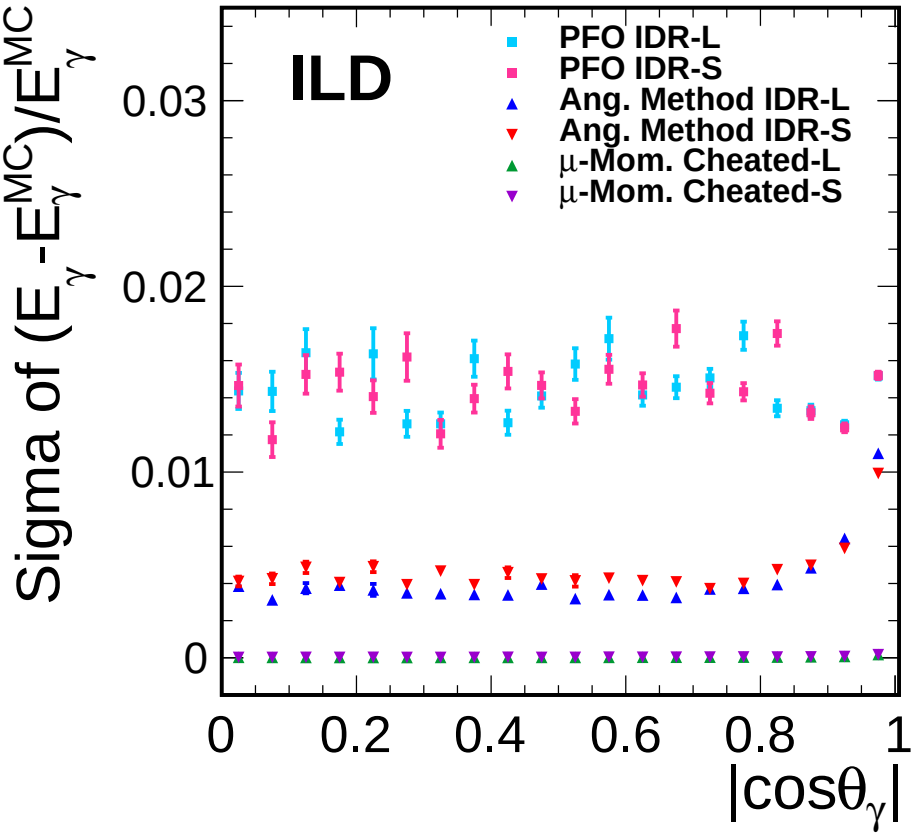

Figure 8.9: Similar plot to Fig. 8.7 but with additionally the sigma value for kinematically reconstructed photon energies cheating muon momenta for IDR-L (μ-Mom. Cheated-L: Green) and for IDR-S (μ-Mom. Cheated-S: Violet).

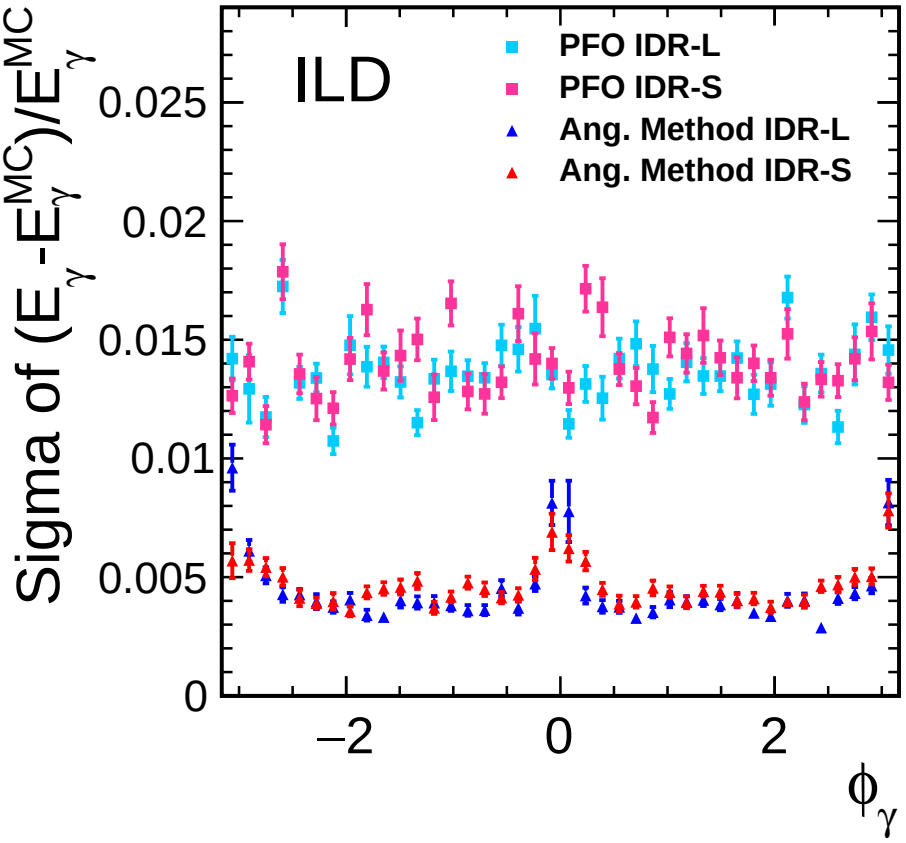

Figure 8.10: Sigma value from a Gaussian fit to the distribution of the relative difference from the MC truth as a function of ϕ_γ for each of measured (PFO IDR-L: light blue, PFO IDR-S: magenta) and kinematically reconstructed photon energies (Ang. Method IDR-L: blue, Ang. Method IDR-S: red). Only photons satisfying $|\cos\theta_\gamma| \leq 0.95$ are included in this plot.

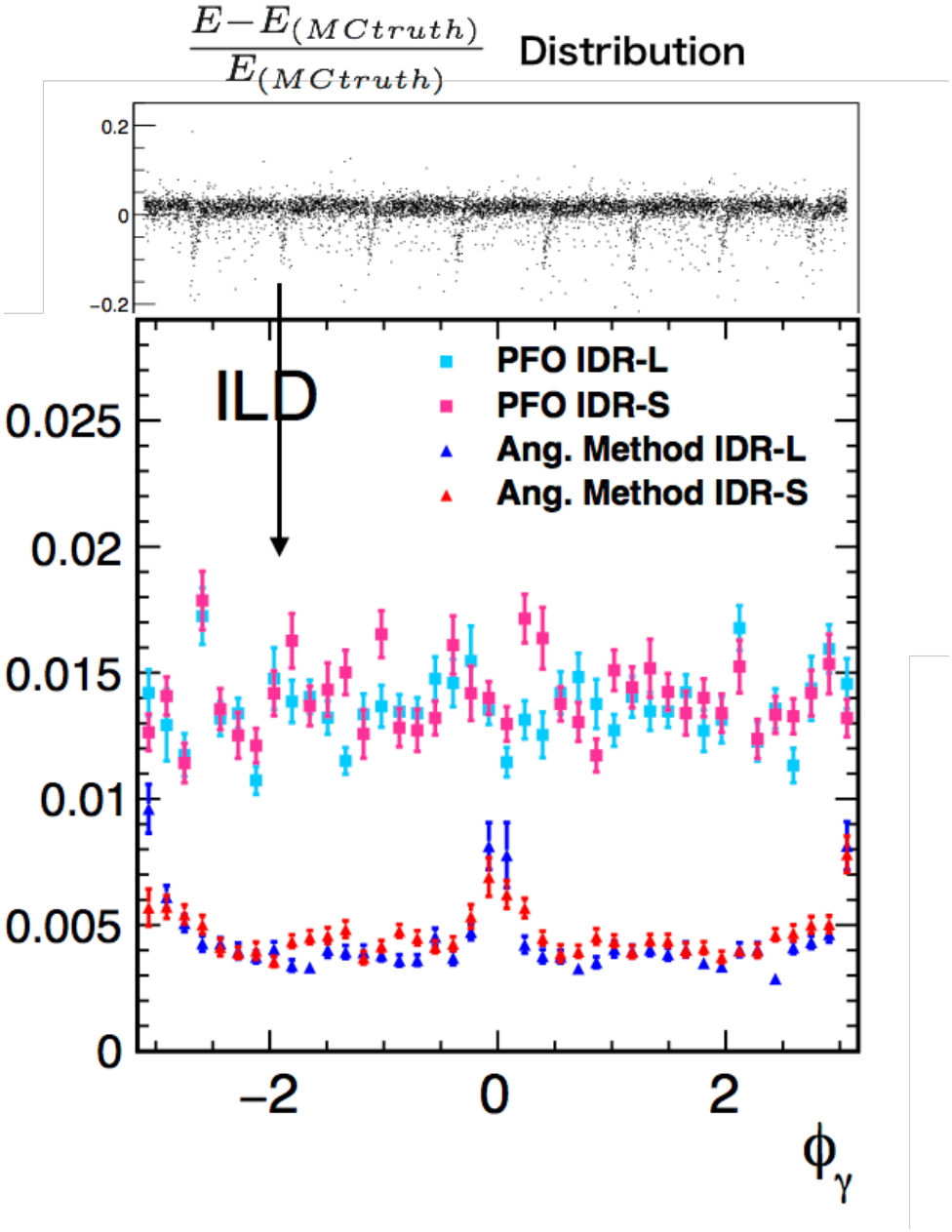

Figure 8.11: Explanation of the large fluctuation of PFO in Fig. 8.10.

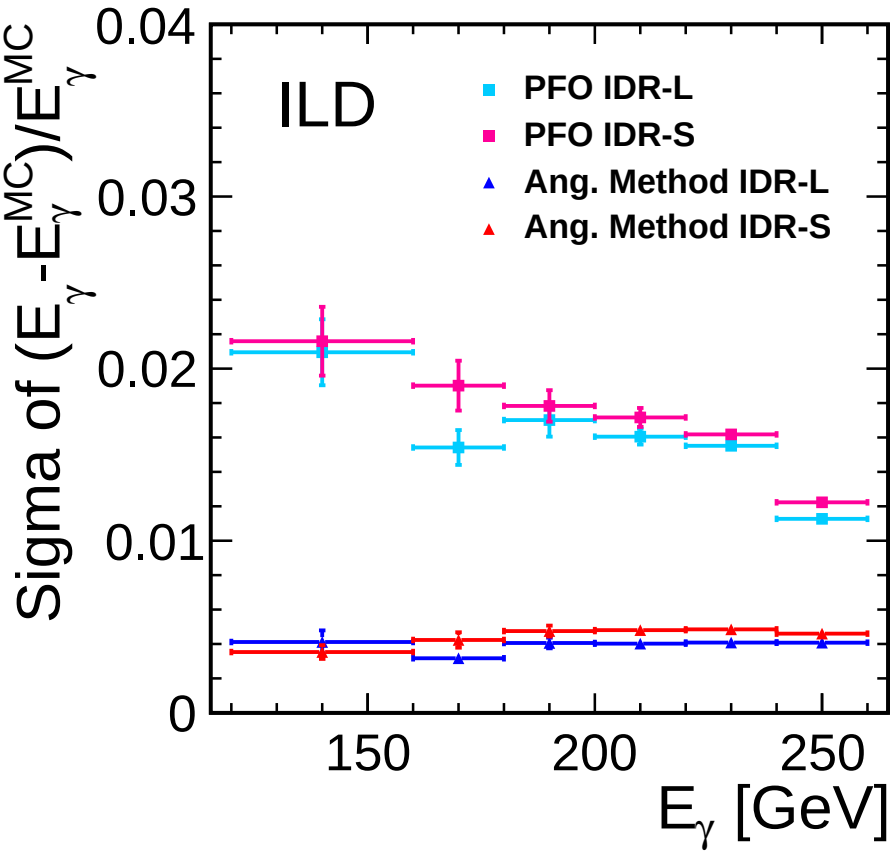

Figure 8.12: Sigma value from a Gaussian fit to the distribution of the relative difference from the MC truth as a function of E_γ for each of measured (PFO IDR-L: light blue, PFO IDR-S: magenta) and kinematically reconstructed photon energies (Ang. Method IDR-L: blue, Ang. Method IDR-S: red). Only photons satisfying $|\sin\phi_\gamma| \geq 0.1$ and $|\cos\theta_\gamma| \leq 0.95$ are included in this plot.

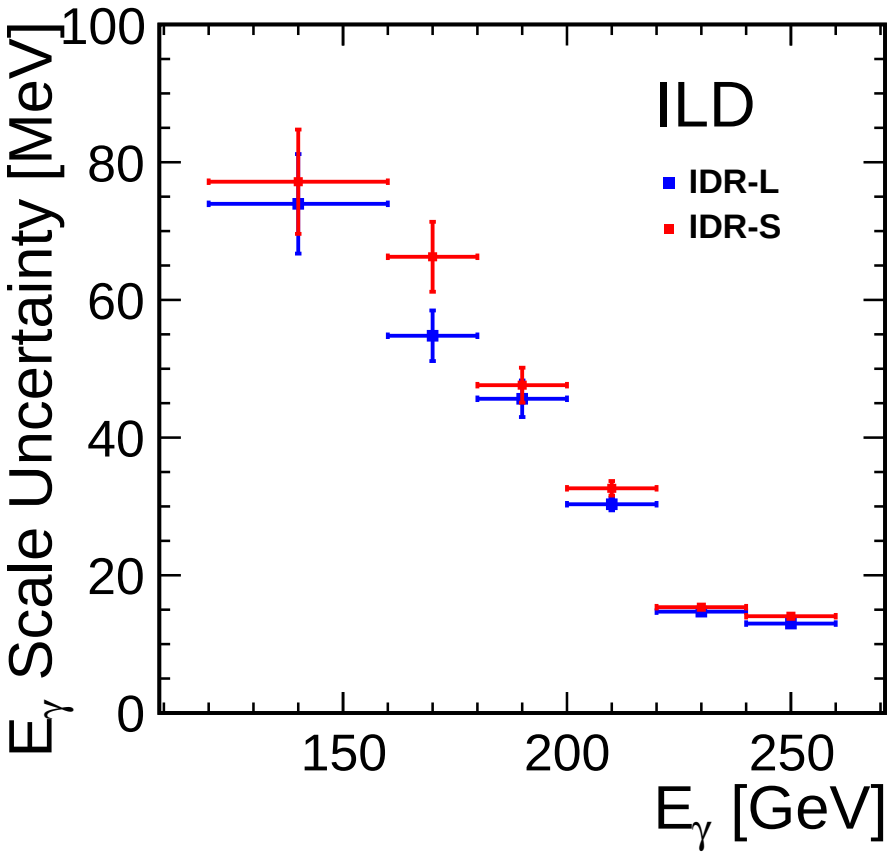

Figure 8.13: E_γ scale uncertainty after the photon energy calibration using the Angular Method as a function of E_γ for $|\sin\phi_\gamma| \geq 0.1$ and $|\cos\theta_\gamma| \leq 0.95$.

Chapter 9

Summary of Part II

Methods to calibrate the photon energy using the $e^+e^- \to \gamma Z$ process are studied. Among the five kinematic reconstruction methods studied, the Angular Method is found to be the best due to its good resolution and its symmetric response. The resolution of the photon energy kinematically reconstructed by the Angular Method is better than that of the PFO photon energy except in the singular regions near $\sin\phi_\gamma = 0$ and $|\cos\theta_\gamma| = 1$ and the Angular Method has almost no bias. We have hence shown that the PFO photon energy can be calibrated effectively using the Angular Method. It is concluded that the photon energy scale uncertainty after the calibration is below 80 MeV for $E_\gamma \sim 120$ GeV decreasing to 15 MeV for $E_\gamma \sim 250$ GeV. There is no large difference in terms of the calibrated photon energy uncertainty between IDR-L and IDR-S.

Part III

Jet Energy Scale Calibration

This part will focus on the jet energy scale (JES) calibration. We will introduce our calibration methods in detail in Section 10. Event simulation and selection will be explained in Sections 11 and 12, respectively. Results will be given in Section 13.

Chapter 10

Jet Energy Calibration Methods

The signal channel used here is $e^+e^- \to \gamma Z, Z \to 2\,\text{Jets}$ which is illustrated in Fig. 10.1. The invariant mass of the 2 jet system should be around M_Z in radiative return events.

Jet energies can be reconstructed by four-momentum conservation making use of measured jet

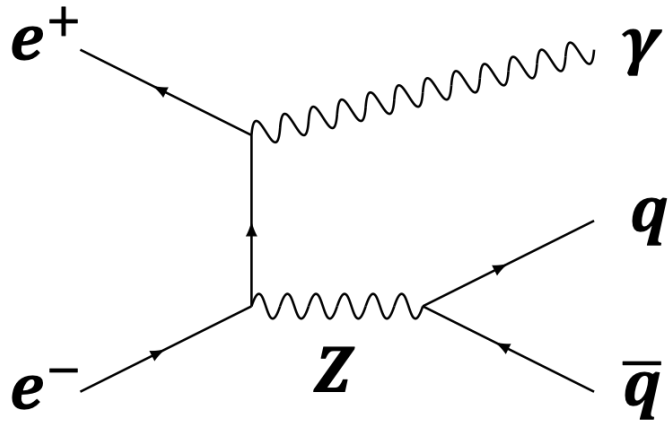

Figure 10.1: Signal channel $e^+e^- \to \gamma Z$, $Z \to q\bar{q}$.

masses and jet and photon direction angles, or measured photon energy or velocities of two jets in addition. Basic four-momentum conservation equations can be written as (10.1).

$$\begin{cases} \sqrt{|P_{J1}|^2 + m_{J1}^2} + \sqrt{|P_{J2}|^2 + m_{J2}^2} + |P_\gamma| + |P_{ISR}| = E_{CM} \\ |P_{J1}| \sin\theta_{J1} \cos\phi_{J1} + |P_{J2}| \sin\theta_{J2} \cos\phi_{J2} + |P_\gamma| \sin\theta_\gamma \cos\phi_\gamma + |P_{ISR}| \sin\alpha = E_{CM} \sin\alpha \\ |P_{J1}| \sin\theta_{J1} \sin\phi_{J1} + |P_{J2}| \sin\theta_{J2} \sin\phi_{J2} + |P_\gamma| \sin\theta_\gamma \sin\phi_\gamma = 0 \\ |P_{J1}| \cos\theta_{J1} + |P_{J2}| \cos\theta_{J2} + |P_\gamma| \cos\theta_\gamma \pm |P_{ISR}| \cos\alpha = 0 \end{cases} \tag{10.1}$$

Here P denotes the unknown jet momentum and m, θ and ϕ are the jet mass, polar angle and azimuthal angle, respectively. Suffixes $J1$, $J2$, γ and ISR correspond to one jet, the other jet, signal photon and additional unseen photon, respectively. E_{CM} is the center of mass energy of the e^+e^- beam collision and α is 7.0 mrad, half of the beam crossing angle as shown in Fig. 5.3.

Depending on the variables and conditions in the jet energy reconstructions, the following five methods are considered: “ Method 1 ”, “ Method 2′ ”, “ Method 2 ”, “ Method 3 ” and “ Method 4 ”.

Method 1 ignores beamstrahlung and additional ISR. In this case, energy conservation in (10.1) does not have to be considered and therefore measured jet masses are not necessary for the inputs. Then the method requires measured $\{\theta_{J1}, \theta_{J2}, \theta_\gamma, \phi_{J1}, \phi_{J2}, \phi_\gamma\}$ as inputs to determine $\{|P_{J1}|, |P_{J2}|, |P_\gamma|\}$. The required conservation equations are:

$$\begin{cases} \begin{pmatrix} \sin\theta_{J1}\cos\phi_{J1} & \sin\theta_{J2}\cos\phi_{J2} & \sin\theta_\gamma\cos\phi_\gamma \\ \sin\theta_{J1}\sin\phi_{J1} & \sin\theta_{J2}\sin\phi_{J2} & \sin\theta_\gamma\sin\phi_\gamma \\ \cos\theta_{J1} & \cos\theta_{J2} & \cos\theta_\gamma \end{pmatrix} \begin{pmatrix} |P_{J1}| \\ |P_{J2}| \\ |P_\gamma| \end{pmatrix} = \begin{pmatrix} E_{CM}\sin\alpha \\ 0 \\ 0 \end{pmatrix} \end{cases} \tag{10.2}$$

Method 2′ and Method 2 use the measured $|P_\gamma|$ as an input in addition to the jet angles, photon angles and jet masses. Method 2′ ignores beamstrahlung and additional ISR and four-momentum conservation requires measured $\{\theta_{J1}, \theta_{J2}, \theta_\gamma, \phi_{J1}, \phi_{J2}, \phi_\gamma, m_{J1}, m_{J2}, |P_\gamma|\}$ as inputs to determine $\{|P_{J1}|, |P_{J2}|\}$. The required conservation equations are:

$$\begin{cases} \begin{pmatrix} \sin\theta_{J1}\cos\phi_{J1} & \sin\theta_{J2}\cos\phi_{J2} \\ \sin\theta_{J1}\sin\phi_{J1} & \sin\theta_{J2}\sin\phi_{J2} \end{pmatrix} \begin{pmatrix} |P_{J1}| \\ |P_{J2}| \end{pmatrix} = \begin{pmatrix} E_{CM}\sin\alpha - \sin\theta_\gamma\cos\phi_\gamma|P_\gamma| \\ -\sin\theta_\gamma\sin\phi_\gamma|P_\gamma| \end{pmatrix} \end{cases} \tag{10.3}$$

Method 2 considers beamstrahlung and additional ISR. Four-momentum conservation requires measured $\{\theta_{J1}, \theta_{J2}, \theta_\gamma, \phi_{J1}, \phi_{J2}, \phi_\gamma, m_{J1}, m_{J2}, |P_\gamma|\}$ as inputs to determine $\{|P_{J1}|, |P_{J2}|, |P_{ISR}|\}$. The four-momentum conservation (10.1) takes the form of:

$$\begin{cases} \sqrt{|P_{J1}|^2 + m_{J1}^2} + \sqrt{|P_{J2}|^2 + m_{J2}^2} + |P_\gamma| + |P_{ISR}| = E_{CM} \\ \begin{pmatrix} \sin\theta_{J1}\cos\phi_{J1} & \sin\theta_{J2}\cos\phi_{J2} & \sin\alpha \\ \sin\theta_{J1}\sin\phi_{J1} & \sin\theta_{J2}\sin\phi_{J2} & 0 \\ \cos\theta_{J1} & \cos\theta_{J2} & \pm\cos\alpha \end{pmatrix} \begin{pmatrix} |P_{J1}| \\ |P_{J2}| \\ |P_{ISR}| \end{pmatrix} = \begin{pmatrix} E_{CM}\sin\alpha - \sin\theta_\gamma\cos\phi_\gamma|P_\gamma| \\ -\sin\theta_\gamma\sin\phi_\gamma|P_\gamma| \\ -\cos\theta_\gamma|P_\gamma| \end{pmatrix} \end{cases} \tag{10.4}$$

As there are 2 direction candidates for the ISR which correspond to the sign of $|P_{ISR}|$ in P_z conservation, 2 possible solutions can be obtained from the three-momentum conservation. In order to choose the better answer, the left-hand side of the energy conservation of (10.4) is calculated for each solution and compare which solution is closer to the right-hand side.

Method 3 solves the full set of four-momentum conservation equations (10.1). It uses measured $\{\theta_{J1}, \theta_{J2}, \theta_\gamma, \phi_{J1}, \phi_{J2}, \phi_\gamma, m_{J1}, m_{J2}\}$ as inputs to determine $\{|P_{J1}|, |P_{J2}|, |P_\gamma|, |P_{ISR}|\}$. Then four-momentum conservation is:

$$\begin{cases} \sqrt{|P_{J1}|^2 + m_{J1}^2} + \sqrt{|P_{J2}|^2 + m_{J2}^2} + |P_\gamma| + |P_{ISR}| = E_{CM} \\ \begin{pmatrix} \sin\theta_{J1}\cos\phi_{J1} & \sin\theta_{J2}\cos\phi_{J2} & \sin\theta_\gamma\cos\phi_\gamma \\ \sin\theta_{J1}\sin\phi_{J1} & \sin\theta_{J2}\sin\phi_{J2} & \sin\theta_\gamma\sin\phi_\gamma \\ \cos\theta_{J1} & \cos\theta_{J2} & \cos\theta_\gamma \end{pmatrix} \begin{pmatrix} |P_{J1}| \\ |P_{J2}| \\ |P_\gamma| \end{pmatrix} = \begin{pmatrix} (E_{CM} - |P_{ISR}|)\sin\alpha \\ 0 \\ \pm|P_{ISR}|\cos\alpha \end{pmatrix} \end{cases} \tag{10.5}$$

As the first equation of (10.5) includes two radical signs which make a quartic equation, 4 possible solutions appear for each sign of the ISR. As a result, 8 possibilities exists in (10.5). In order to examine those solutions, following criteria were considered.

1. Solution $|P_{ISR}|$ should take real and positive value less than half of the E_{CM}.

2. Solutions $\{|P_{J1}|, |P_{J2}|, |P_\gamma|\}$ should take (real and) positive values.

3. Each radical expressed by variables other than those contained in the radical should be positive, namely

$$\begin{aligned}\sqrt{|P_{J1}|^2+m_{J1}^2} &= E_{CM}-\left(\sqrt{|P_{J2}|^2+m_{J2}^2}+|P_\gamma|+|P_{ISR}|\right)>0\\ \sqrt{|P_{J2}|^2+m_{J2}^2} &= E_{CM}-\left(\sqrt{|P_{J1}|^2+m_{J1}^1}+|P_\gamma|+|P_{ISR}|\right)>0.\end{aligned}$$

4. Solution $|P_\gamma|$ should be the closest to the measured $|P_\gamma|$ among all solution candidates satisfying above criteria.

The jet mass $m_{Ji}\,(i=1,2)$ can be expressed as $\frac{|P_{Ji}|}{\gamma_{Ji}\beta_{Ji}}$ where β_{Ji} is ratio of the velocity v_{Ji} to the speed of the light in a vacuum c; $\beta_{Ji}=\frac{v_{Ji}}{c}$ and γ_{Ji} is the Lorentz factor; $\gamma_{Ji}=\frac{1}{\sqrt{1-\beta_{Ji}^2}}$. When using $\gamma\beta$ as input, the first equation of (10.5) in the Method 3 would be a linear equation. In this case, only two-fold ambiguity exists corresponding to the direction of the ISR which can be removed by comparing solution $|P_\gamma|$ with measured $|P_\gamma|$. Then, Method 4 uses measured $\{\theta_{J1},\theta_{J2},\theta_\gamma,\phi_{J1},\phi_{J2},\phi_\gamma,m_{J1},m_{J2}\}$ as inputs to determine $\{|P_{J1}|,|P_{J2}|,|P_\gamma|,|P_{ISR}|\}$.

$$\begin{cases} |P_{J1}|\sqrt{1+\frac{1}{(\gamma\beta)_{J1}^2}}+|P_{J2}|\sqrt{1+\frac{1}{(\gamma\beta)_{J2}^2}}+|P_\gamma|+|P_{ISR}|=E_{CM}\\ \begin{pmatrix}\sin\theta_{J1}\cos\phi_{J1} & \sin\theta_{J2}\cos\phi_{J2} & \sin\theta_\gamma\cos\phi_\gamma\\ \sin\theta_{J1}\sin\phi_{J1} & \sin\theta_{J2}\sin\phi_{J2} & \sin\theta_\gamma\sin\phi_\gamma\\ \cos\theta_{J1} & \cos\theta_{J2} & \cos\theta_\gamma\end{pmatrix}\begin{pmatrix}|P_{J1}|\\|P_{J2}|\\|P_\gamma|\end{pmatrix}=\begin{pmatrix}(E_{CM}-|P_{ISR}|)\sin\alpha\\0\\\pm|P_{ISR}|\cos\alpha\end{pmatrix}\end{cases} \tag{10.6}$$

Performances of the five methods will be compared in Section 13.

Chapter 11

Simulation Setup

In this part, signal events, $e^+e^- \to \gamma Z, Z \to 2$ Jets, are first generated using Whizard 2.85 [38] and detector geometry is ILD-L. It uses a hybrid calorimeter simulation, of which we consider the o1 model, whose calorimeters are Si-ECAL and AHCAL. It implements the 14 mrad beam crossing angle, IP smearing and offset depending on the initial particles [38]. The whole set of programs used in this analysis is packaged as iLCSoft version v02-02 [38]. The event simulation for this analysis has been done at the center-of-mass energy of 250 GeV. We assume an integrated luminosity $\int Ldt = 900\,\mathrm{fb}^{-1}$ for each of two beam polarizations: "eLpR" in which $(P_{e^-}, P_{e^+}) = (-0.8, +0.3)$ and "eRpL" in which $(+0.8, -0.3)$. To simplify the analysis, overlay removal by MCTruth link is implemented. Two MCTruth definitions were employed: "All-MC" which contains all stable MC particles and "Detected-MC" which contains only particles linked to detected PFOs.

Chapter 12

Event Selection

Signatures of the signal events are 2 jets with a combined invariant mass consistent with the Z boson mass and one energetic isolated photon. First, events with at least one isolated photon are selected. The photon is identified using Photon ID by PandoraPFA. The photon energy is required to be more than 50 GeV. The photon whose energy is closest to the expected value, *i.e.* 108.4 GeV, is selected and all photons inside the cone with opening angle $\cos^{-1}(0.998)$ around the direction of the photon are merged. Owing to beamstrahlung and ISR effects, the photon energy spectrum has a long downward tail from its peak at 108.4 GeV, as shown in Fig. 12.2.

After this selection, for eLpR samples, 82.2% of the generated events contain no signal photon and 17.8% contain one signal photon. Then, All Particle Flow Objects (PFOs) other than the selected photon are clustered into 2 jets using the Durham algorithm (done by LCFIPlus). The jet with higher reconstructed energy is defined as "jet 1" and the other as "jet 2".

Figure 12.1 shows the distribution of All-MC truth invariant mass of Z boson M_Z and Fig. 12.2 shows the distribution of M_Z and All-MC truth photon energy E_γ for the eLpR samples. The red curve in Fig. 12.2 shows the kinematic boundary corresponding to no additional photon when ignoring the electron and positron masses and the beam crossing angle. Figure 12.3 shows the flavor of the jets of All-MC. Figure 12.4, Fig. 12.5 and Fig. 12.6 show the distributions of All-MC truth jet masses, energies and cosine of polar angle, respectively. Figure 12.7 shows the correlation between cosines of All-MC truth jet polar angle of 2 jets. Figure 12.8 shows correlation between cosine of All-MC truth jet polar angle and All-MC truth jet energy for each jet.

After these selections, there are still some events in which the measured signal photon does not match with the MCTruth signal photon *i.e.* wrong photon selection events. Comparing the polar angles of measured signal photon with the MCTruth photon revealed that 9.8% of the eLpR sample suffered from wrong photon selection corresponds to
$|\Delta\theta_\gamma| \equiv |\theta_\gamma^{MC} - \theta_\gamma^{PFO}| > 0.01$ rad. Figure 12.9 shows the $|\Delta\theta_\gamma|$ of the signal photon and visible energy defined as $E_{vis} \equiv E_{J1} + E_{J2} + E_\gamma$ distribution. According to the Fig. 12.9, two classes of wrong photon selection can be seen: in one case E_{vis} is around 250 GeV but $|\Delta\theta_\gamma| > 0.01$, and in the other E_{vis} is much below 250 GeV and $|\Delta\theta_\gamma| > 0.01$. In the former case the true signal photon had a small energy and was not reconstructed and in the second case the true signal photon was energetic but not found. In both cases, the selected signal photon originates from the jets, for example by final state radiation (FSR). In order to suppress these wrong selected photon events, the invariant mass of 2 jets M_{2j} and the visible energy E_{vis} were compared between the correct and wrong photon selection cases as shown in Fig. 12.10. According to the

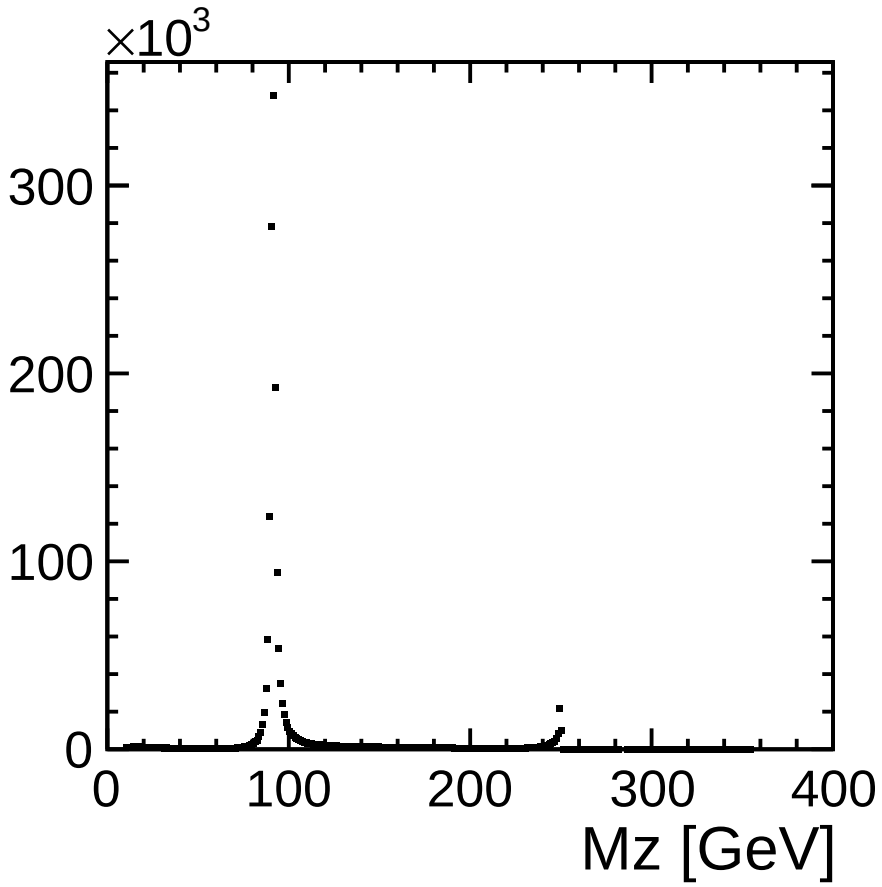

Figure 12.1: All-MC M_Z distribution for the selected events.

figure, the requirement $M_{2j} < 125\,\mathrm{GeV}$ and $E_{vis} > 200\,\mathrm{GeV}$, named as "Cut P1", would be effective. Then, the angles between each jet and photon $\theta_{J1\gamma}$ and $\theta_{J2\gamma}$ were studied. As shown in Fig. 12.11, the wrong photon tends to be near the jet axis. Therefore, cuts $\cos\theta_{J1\gamma} < 0.95$ and $\cos\theta_{J2\gamma} < 0.95$, named as "Cut P2", were applied. Figure 12.12 shows the M_{2j} distribution after the Cut P1 without $M_{2j} < 125\,\mathrm{GeV}$ and cu tP2. It shows the selection correctness after the Cut P1 and Cut P2 as 99.5%.

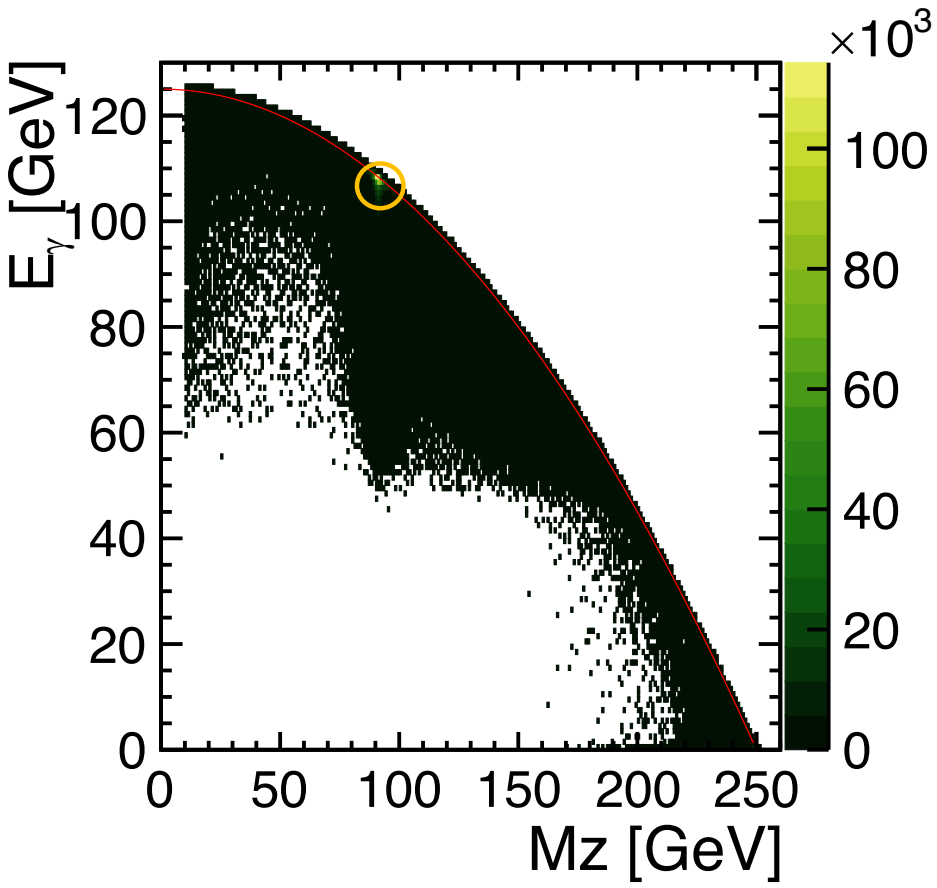

Figure 12.2: All-MC truth M_Z and E_γ distribution for the selected events. Red curve shows the kinematic boundary corresponding to no additional photon.

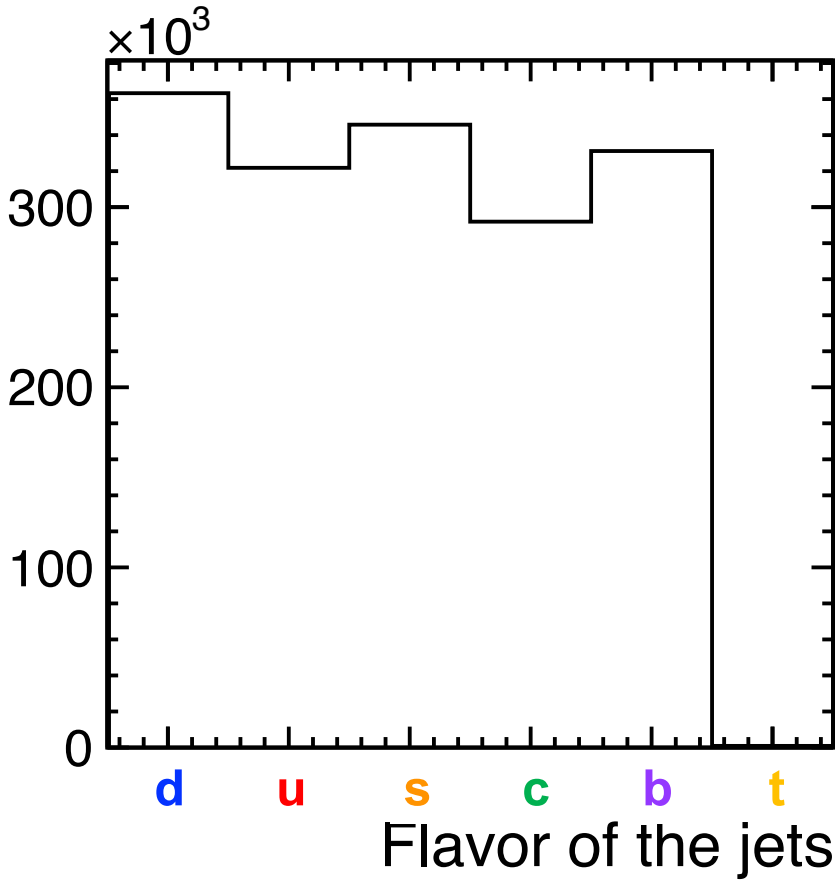

Figure 12.3: Flavor of the jets.

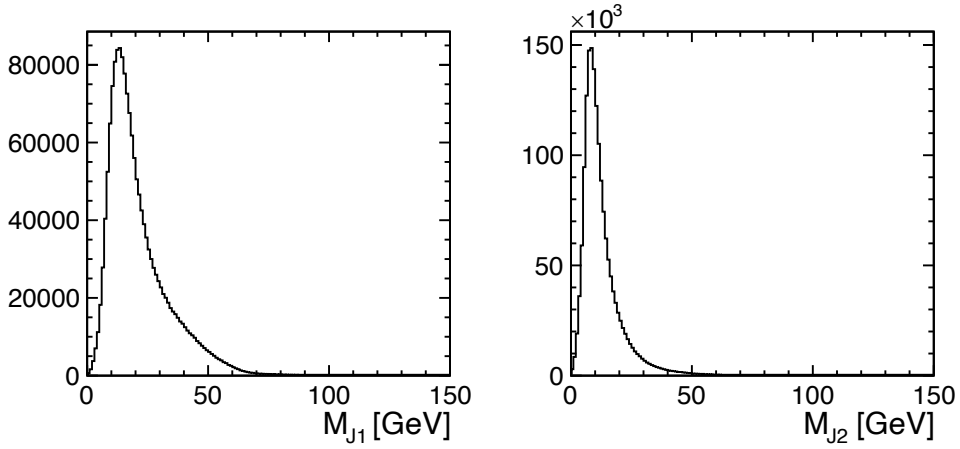

Figure 12.4: All-MC truth jet mass distribution for each jet for the selected events.

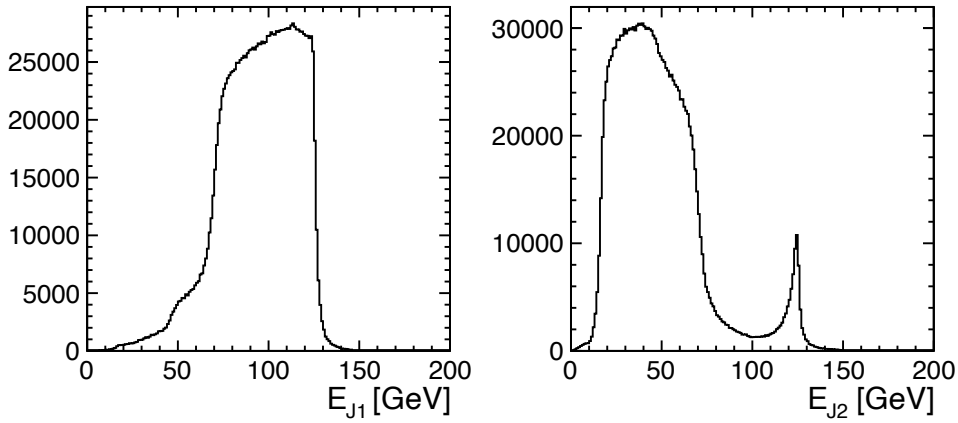

Figure 12.5: All-MC truth jet energy distribution for each jet for the selected events.

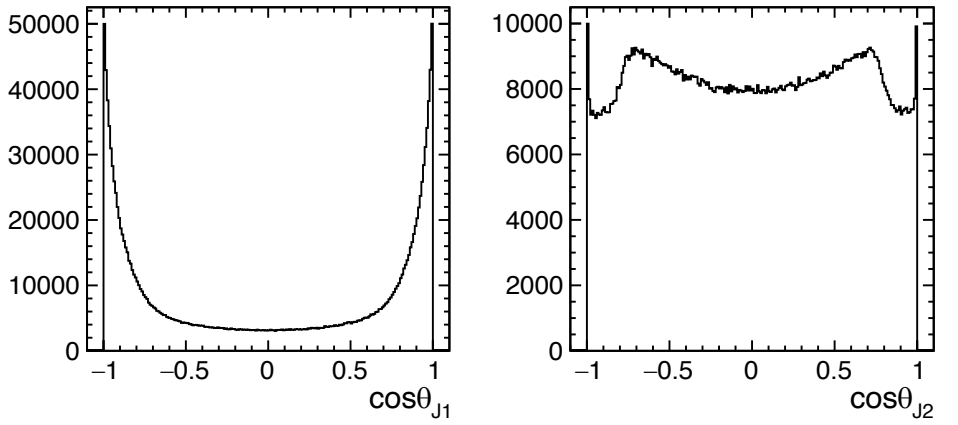

Figure 12.6: Cosine of All-MC truth jet polar angle distribution for each jet for the selected events.

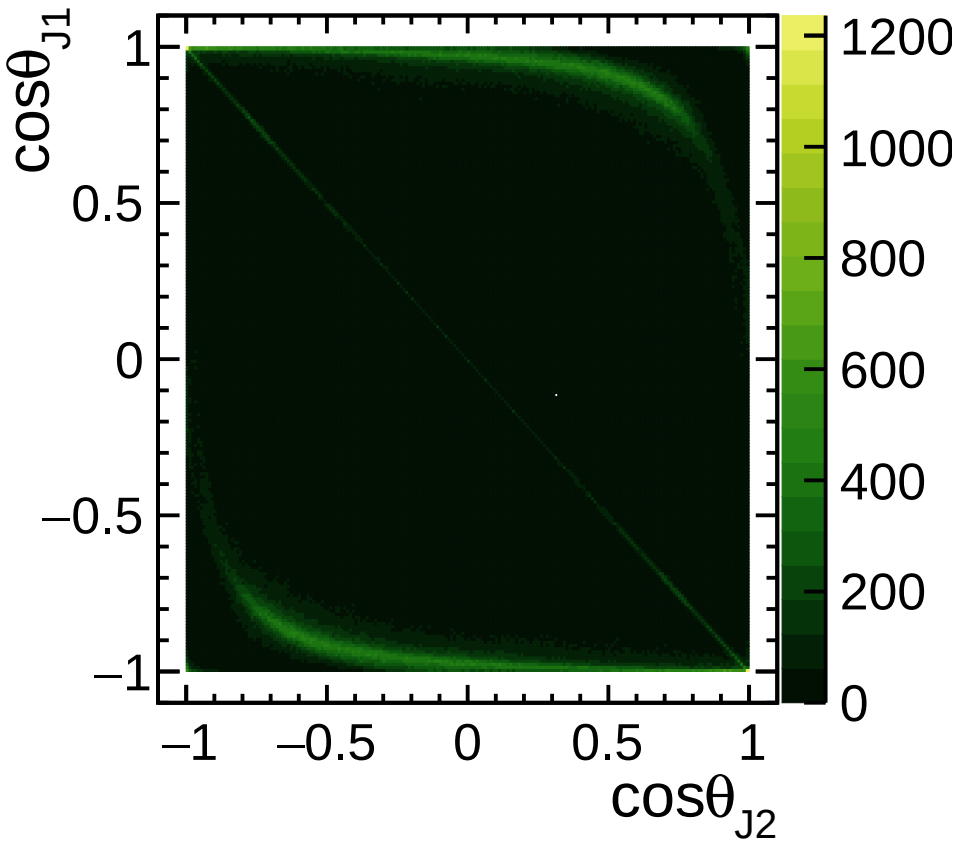

Figure 12.7: Correlation between cosines of All-MC truth jet polar angle of each jet.

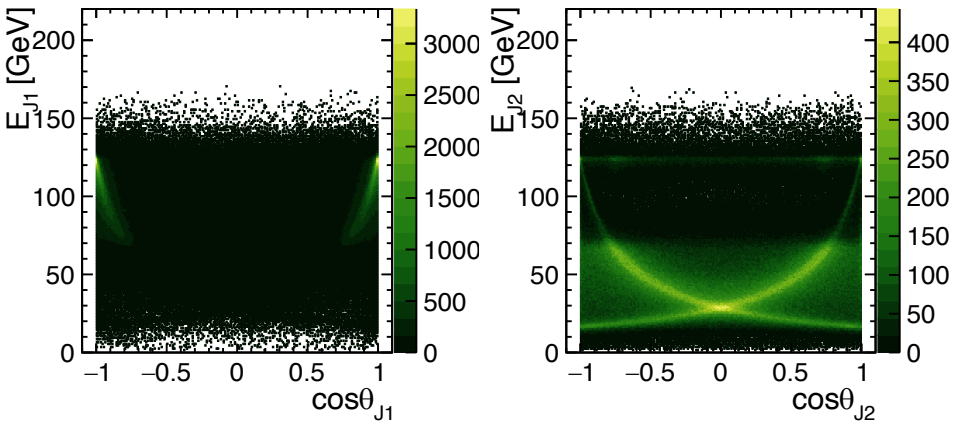

Figure 12.8: Correlation between cosine of All-MC truth jet polar angle and All-MC truth jet energy for each jet. Notice that the color scale is different in each plot.

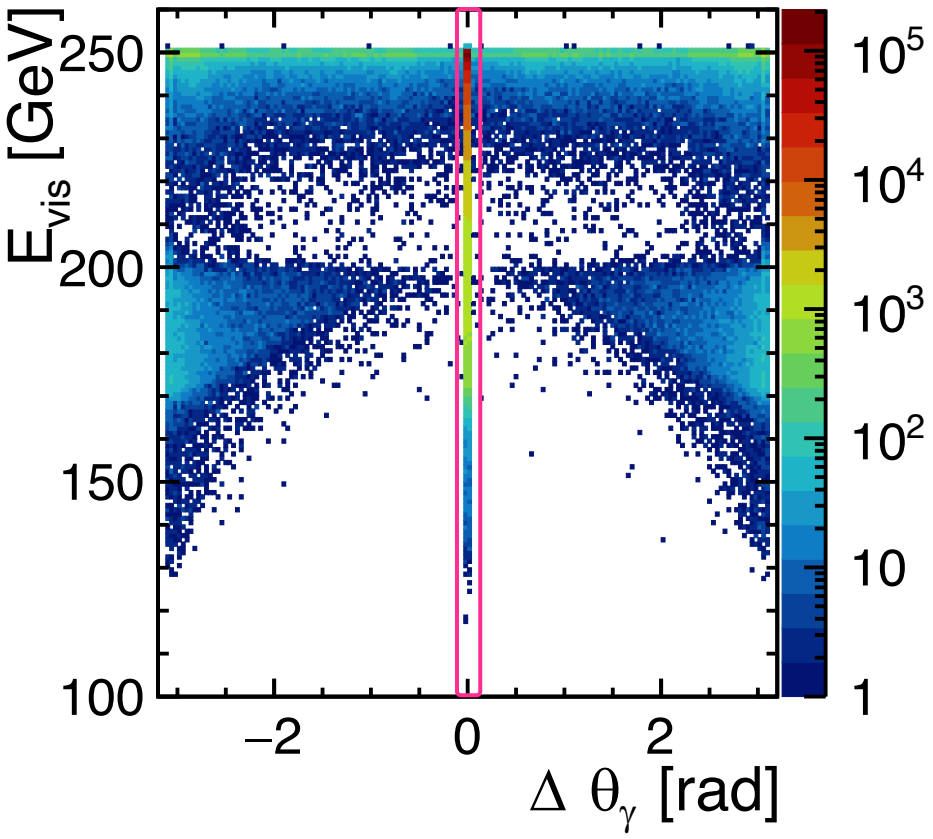

Figure 12.9: Correlation between visible energy $E_{vis} \equiv E_{J1} + E_{J2} + E_\gamma$ and photon angle difference $\Delta\theta_\gamma \equiv \theta_\gamma^{MC} - \theta_\gamma^{PFO}$ for all events with signal photon ($N_{\gamma(E>50\,\mathrm{GeV})} = 1$). Magenta surrounded area indicates correct photon selection.

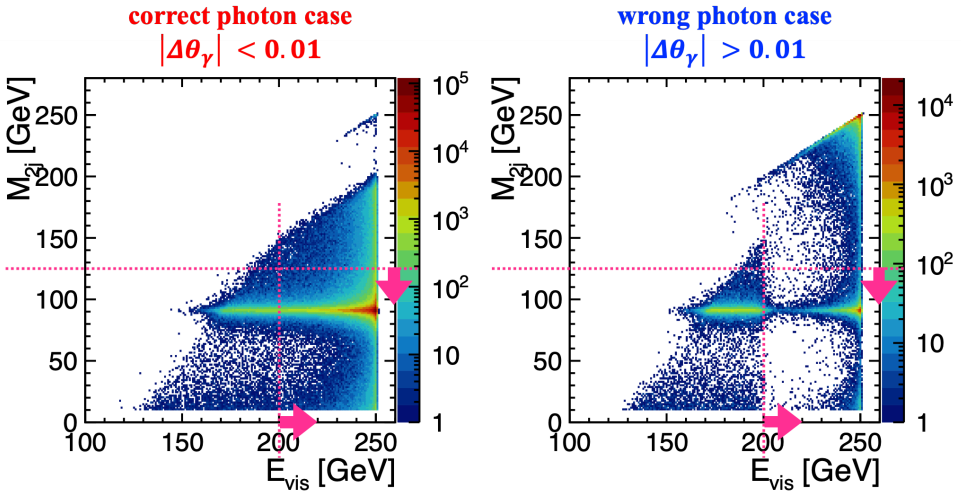

Figure 12.10: Invariant mass of 2 jets M_{2j} and the visible energy E_{vis} for correct photon selection case and wrong photon selection case.

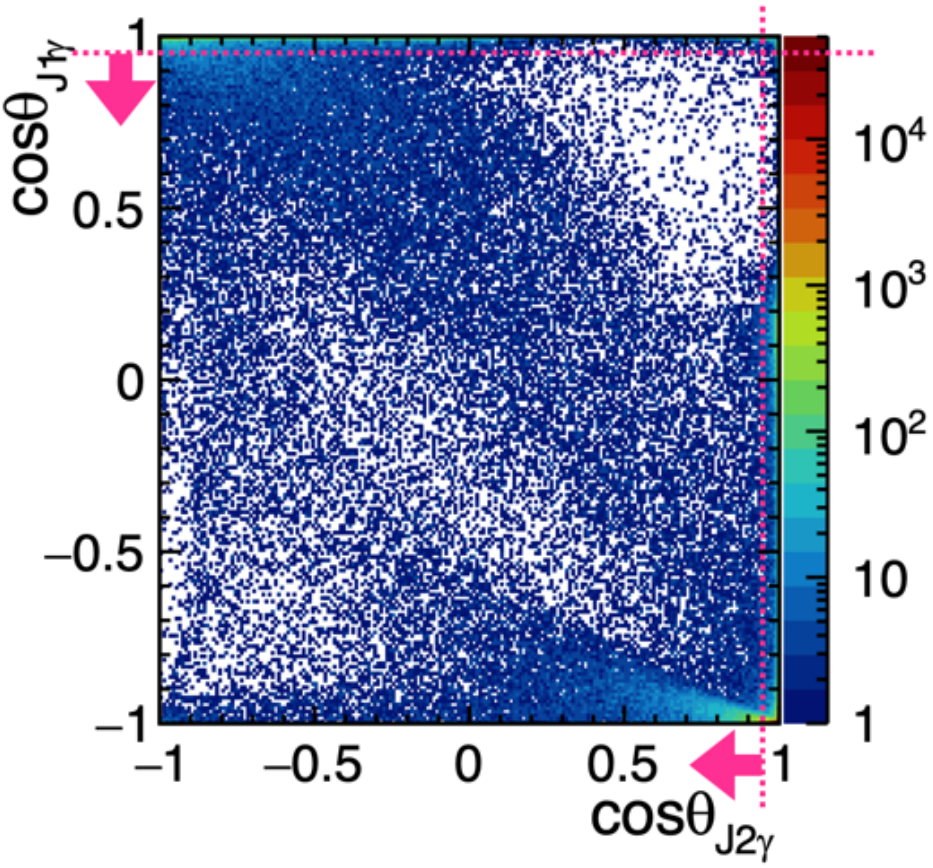

Figure 12.11: Angles between each jet and the selected photon. The wrong photon tends to be near the jet axis.

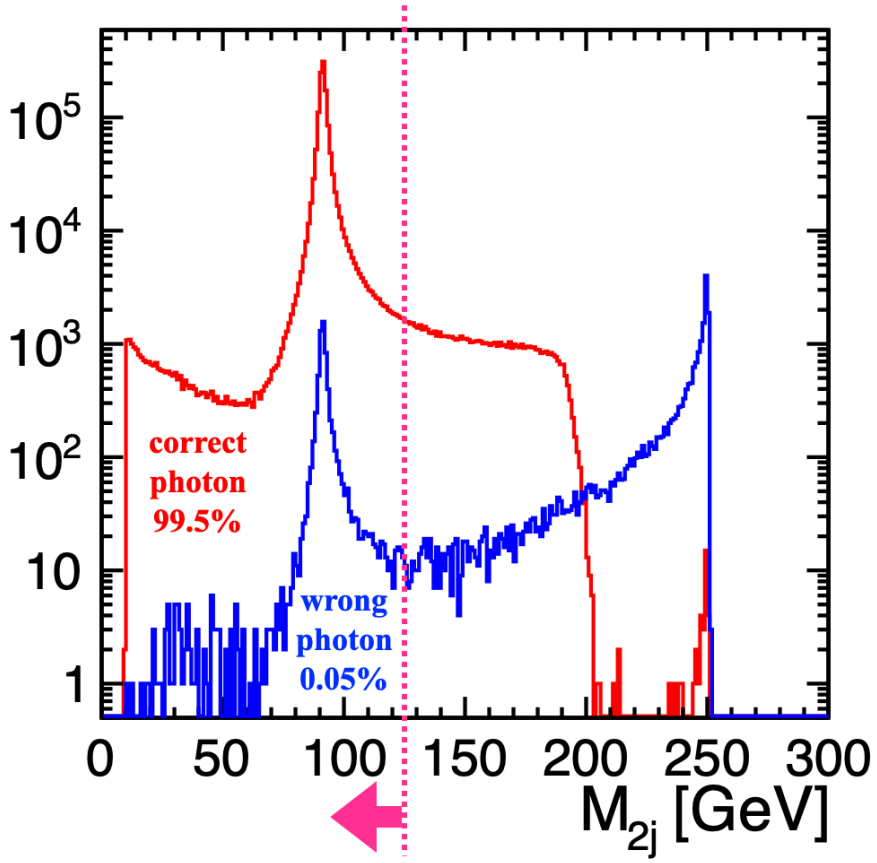

Figure 12.12: M_{2j} distribution of events with $E_{vis} > 200\,\text{GeV}$ and Cut P2. It shows that the sample purity after Cut P1 and Cut P2 is 99.5%.

Chapter 13

Results

13.1 Comparison of the Five Methods

The jet energies are kinematically reconstructed for the selected events using the five methods explained in Section 10. The relative difference of the reconstructed jet energy from its All-MC truth (AlMC), $\frac{(E_J - E_J^{AlMC})}{E_J^{AlMC}}$, is shown in Fig. 13.1. This plot only uses eLpR samples.

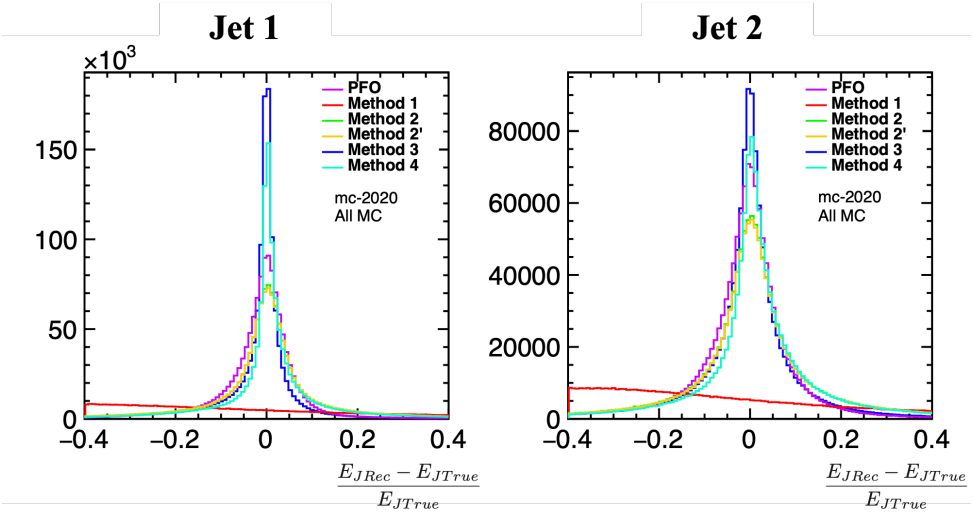

Figure 13.1: The relative difference of the reconstructed jet energy from its All-MC truth (AlMC) for the five methods and PFO.

As shown, Method 3 has the best resolution and its peak position is close to zero (between -0.008 and 0.008). Comparison of the relative difference from its Detected-MC truth (DeMC), $\frac{(E_J - E_J^{DeMC})}{E_J^{DeMC}}$, for eLpR samples is shown in Fig. 13.2. Method 3 gives slightly positive bias up to 0.8% and the peak height became worse, which means Method 3 is rather closer to the all MC than the detected MC. It can recover non-detected particles *e.g.* undetected neutrinos and missing particles going into the beam pipe. Considering these results, it is hence decided to use Method 3 to calibrate the jet energies in what follows. Hereafter Method 3 is referred to as the Angular Method (sometimes abbreviated as "Ang. Method" hereafter).

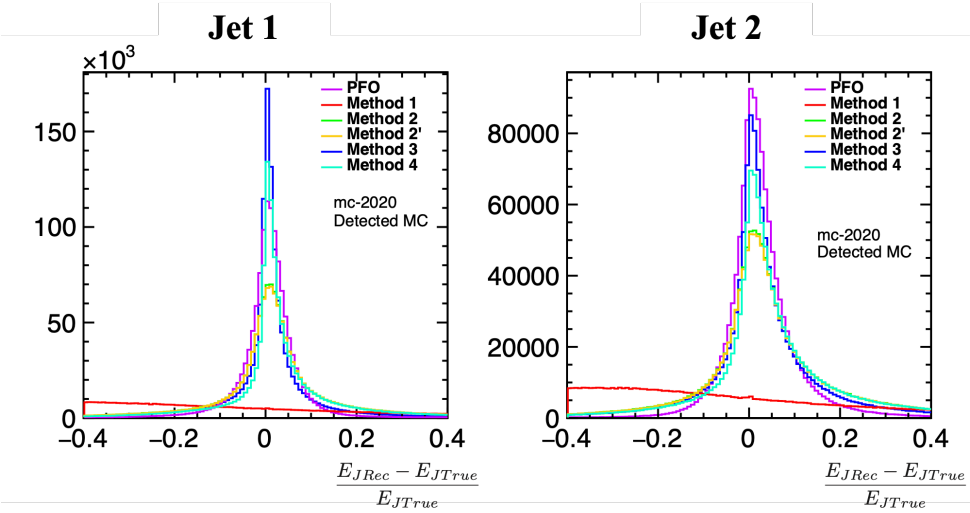

Figure 13.2: The relative difference of the reconstructed jet energy from its Detected-MC truth (DeMC) for the five methods and PFO.

13.2 Energy, Polar Angle and Flavor Dependences

In general, the measured jet energy might be biased depending on jet energy, jet polar angle and jet flavor because of various detector effects and therefore requires calibration. As a step of the calibration using the Angular Method, the dependences of relative differences of reconstructed jet energy shown in the previous section on the jet energy, jet polar angle and jet flavor are checked. In order to evaluate the dependences qualitatively, the relative difference distributions are fitted with a function which is sum of two Gaussian functions and one exponential function. The Gaussian function with smaller/larger sigma is named as a "core Gaussian"/"base Gaussian", respectively. The calibration is based on the mean value of the core Gaussian.

First, a comparison of the reconstructed jet energy with All-MC truth is performed in order to show the validity of the Angular Method. The energy, polar angle, and flavor dependence are shown in Fig. 13.3, Fig. 13.4 and Fig. 13.5, respectively. Figure 13.3 shows that the mean value of the core gaussian is of order 10^{-4} to 10^{-3} independent of the jet energy. The sigma value is better for higher energy jets. Figure 13.4 shows that the energy of forward jets has a slight positive bias, while those in the barrel region jet have a slight negative bias on the core gaussian. Figure 13.5 shows that the mean value of the core gaussian is order of 10^{-4} independent of the flavor.

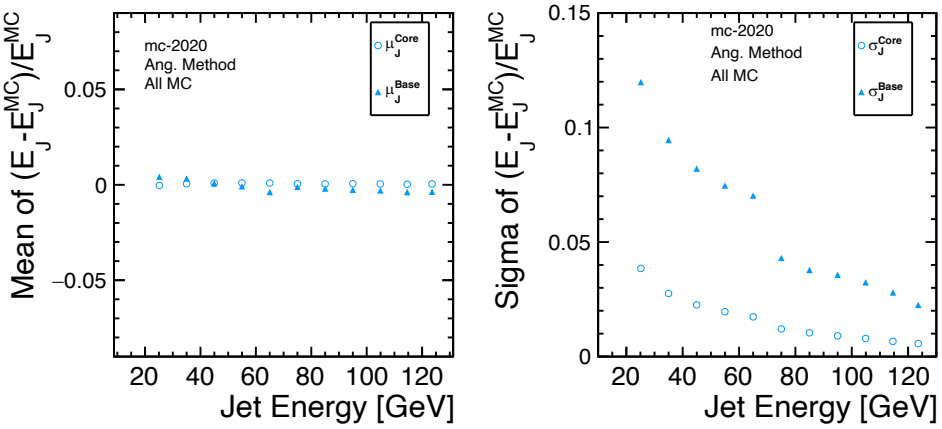

Figure 13.3: Energy dependence of mean and sigma of the fitting Gaussians when using All-MC truth (AlMC) as a reference.

Second, the comparison of the reconstructed jet energy with Detected-MC truth is demonstrated in order to consider the detector calibration. The energy, polar angle, and flavor dependence are shown in Fig. 13.6, Figure 13.7 and Fig. 13.8, respectively. Figure 13.6 and Fig. 13.7 show values are positive at all energies as Angular Method recovers missing particles. Figure 13.8 indicates a larger mean value on the core gaussian in the heavier flavor. This is because heavy flavor jet emits more neutrinos and Angular Method recovers the missing energy.

As a reference, comparison of the PFO jet energy with Detected-MC truth is demonstrated. Energy dependence, polar angle dependence and flavor dependence are shown in Fig. 13.9, Fig. 13.10 and Fig. 13.11, respectively. In comparing PFO energy with Detected-MC, Fig. 13.9, Fig. 13.10 and Fig. 13.11 show PFO has also positive bias due to miscalibration of the calorimeter.

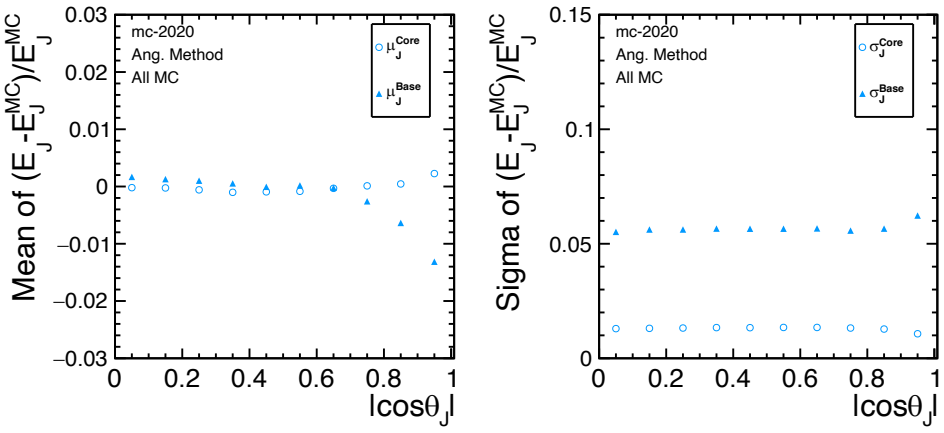

Figure 13.4: Polar angle dependence of mean and sigma of the fitting Gaussians when using All-MC truth (AlMC) as a reference.

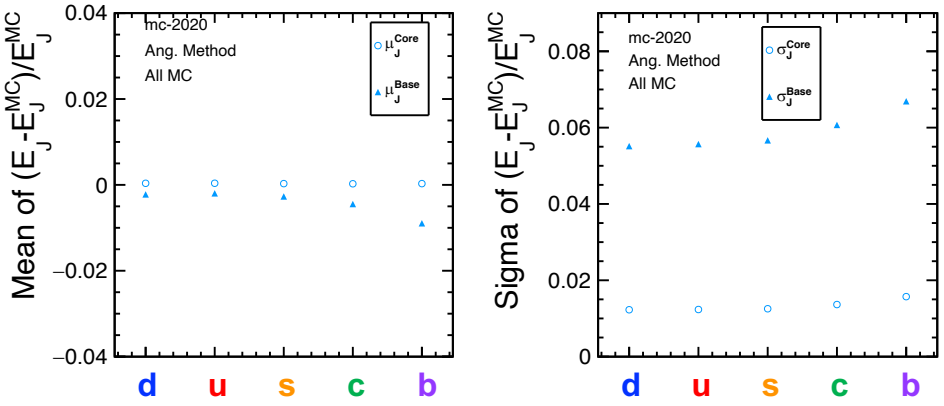

Figure 13.5: Flavor dependence of mean and sigma of the fitting Gaussians when using All-MC truth (AlMC) as a reference.

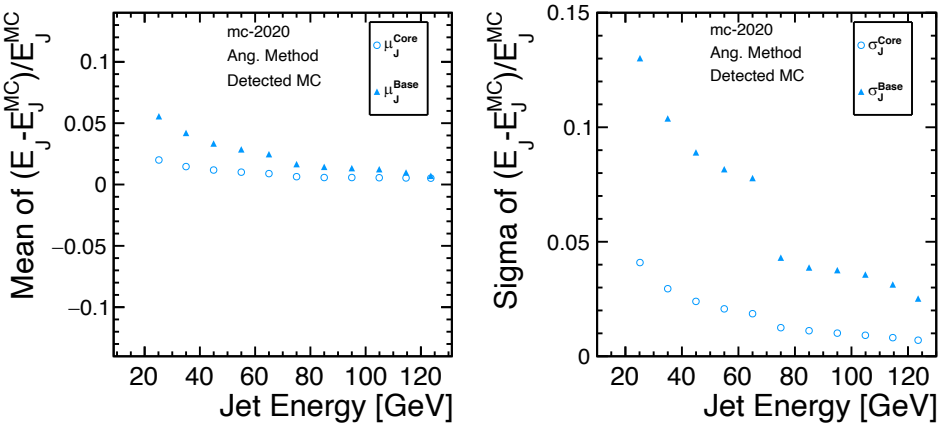

Figure 13.6: Energy dependence of mean and sigma of the fitting Gaussians when using Detected-MC truth (DeMC) as a reference.

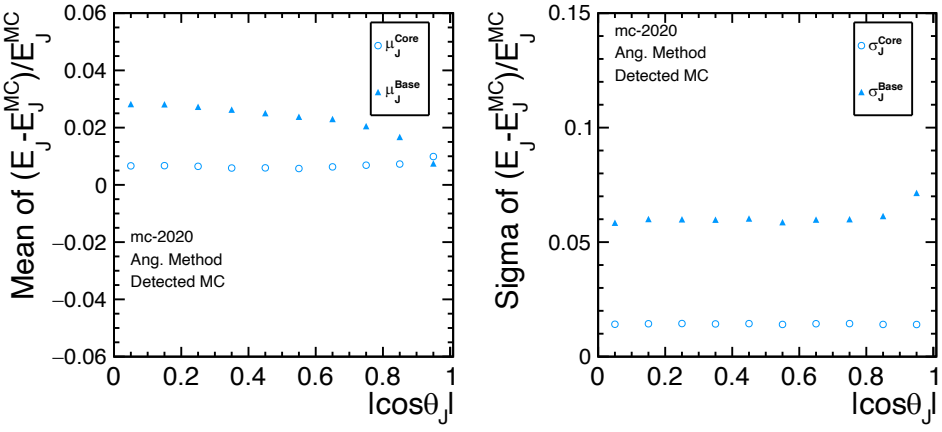

Figure 13.7: Polar angle dependence of mean and sigma of the fitting Gaussians when using Detected-MC truth (DeMC) as a reference.

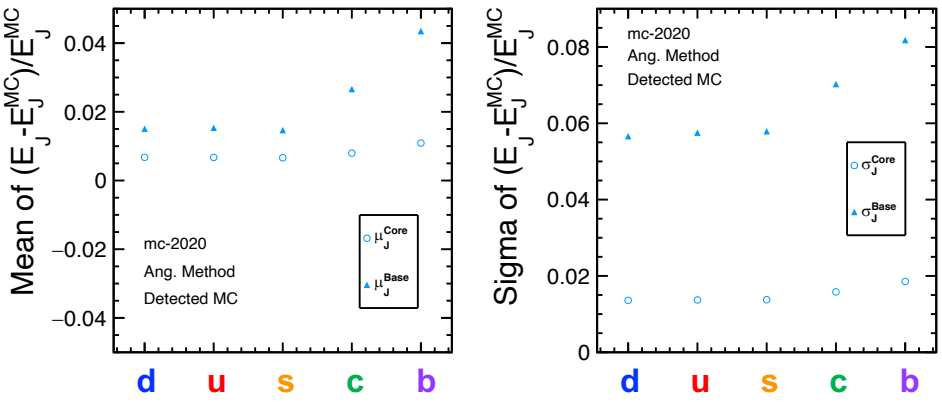

Figure 13.8: Flavor dependence of mean and sigma of the fitting Gaussians when using Detected-MC truth (DeMC) as a reference.

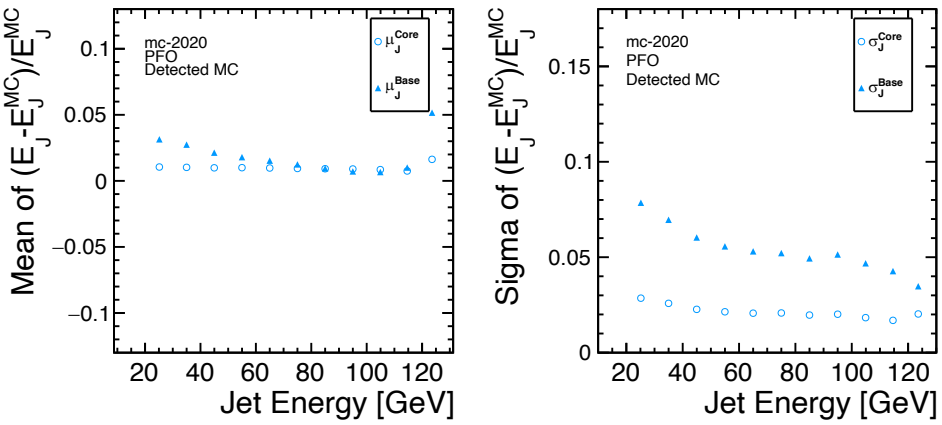

Figure 13.9: Energy dependence of mean and sigma of the fitting Gaussians for PFO when using Detected-MC truth (DeMC) as a reference.

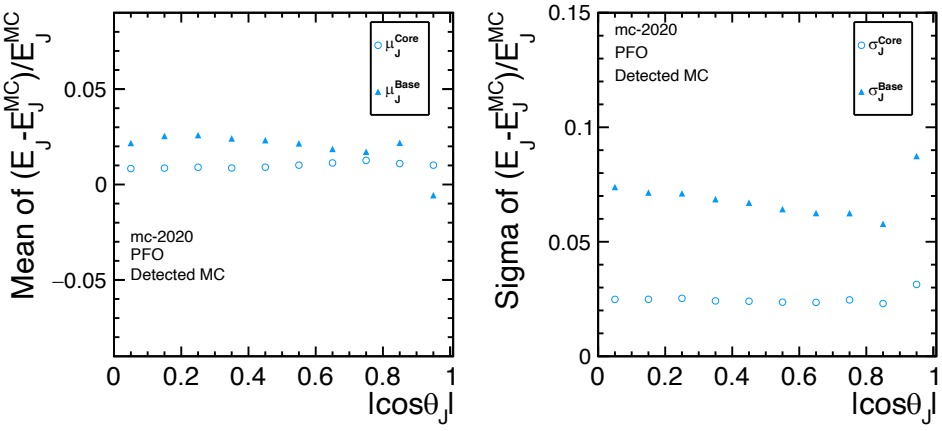

Figure 13.10: Polar angle dependence of mean and sigma of the fitting Gaussians for PFO when using Detected-MC truth (DeMC) as a reference.

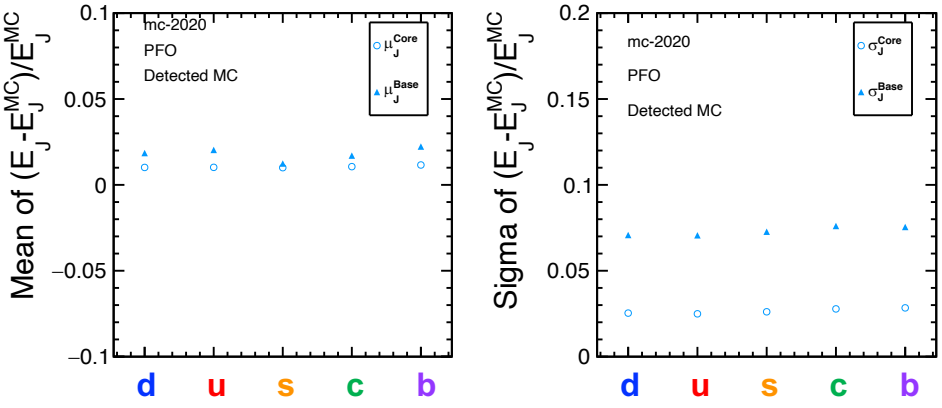

Figure 13.11: Flavor dependence of mean and sigma of the fitting Gaussians for PFO when using Detected-MC truth (DeMC) as a reference.

13.3 Jet Energy Calibration

In this section, we will demonstrate how the calibration can be done using the Angular Method introduced above. To correct the systematic shift in PFO energy, we introduce an energy and angle-dependent calibration factor. First, the distribution of $\frac{(E_J^{PFO}-E_J^{Ang.Method})}{E_J^{Ang.Method}}$ for uds jets is fitted and the mean value μ of the core Gaussian is extracted as a function of energy and $|\cos\theta|$. Then the calibration factor can be derived as $\frac{E_{Ang.Method}}{E_{PFO}} = \frac{1}{\mu+1}$. By taking a look at the fitting result of the relative difference between $E_J^{Ang.Method}$ and E_J^{AlMC} in the high $|\cos\theta|$ region as shown in Fig. 13.12, this fitting is valid up to very high $|\cos\theta|$. The binning in energy and $|\cos\theta|$, shown in Table 13.1, is decided by considering the number of events in each bin.

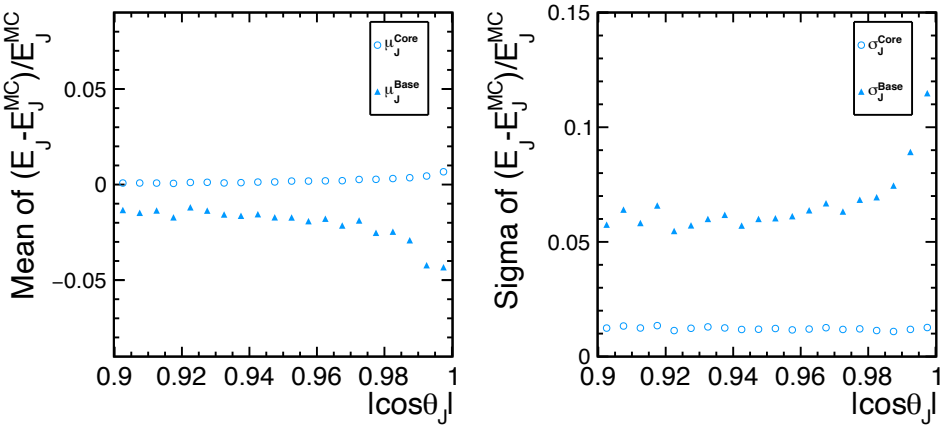

Figure 13.12: Fitting result of the relative difference between $E_J^{Ang.Method}$ and E_J^{AlMC} in the high $|\cos\theta|$ region. Fitting is valid in the very high $|\cos\theta|$ region.

Table 13.1: Binning of the calibration factor

Energy Range [GeV]	Upperbound of $\lvert\cos\theta\rvert$
20-30	0.2,0.4,0.6,0.8,0.9,0.95,1.0
30-40	0.2,0.4,0.6,0.8,0.9,0.94,0.97,1.0
40-50	0.2,0.4,0.6,0.8,0.9,0.94,0.97,1.0
50-60	0.2,0.4,0.6,0.8,0.9,0.92,0.94,0.96,0.98,1.0
60-70	0.2,0.4,0.6,0.8,0.9,0.92,0.94,0.96,0.98,1.0
70-80	0.2,0.4,0.6,0.8,0.9,0.92,0.94,0.96,0.98,1.0
80-90	0.2,0.4,0.6,0.8,0.9,0.92,0.94,0.96,0.98,1.0
90-100	0.2,0.4,0.6,0.8,0.9,0.92,0.94,0.96,0.98,1.0
100-110	0.2,0.4,0.6,0.8,0.9,0.92,0.94,0.96,0.97,0.98,0.985,0.99,0.995,1.0
110-120	0.2,0.4,0.6,0.8,0.9,0.92,0.94,0.96,0.97,0.98,0.985,0.99,0.995,1.0
120-130	0.2,0.4,0.6,0.8,0.9,0.92,0.94,0.96,0.97,0.98,0.985,0.99,0.995,1.0

The dependence of the calibration factor on energy and $|\cos\theta|$ is shown in Fig. 13.13. This result indicates the curved surface of the calibration factor is smooth enough to interpolate the intermediate values.

Using the derived calibration factor, calibration for PFO is performed. The relative difference

between calibrated E_J^{PFO} and $E_J^{Ang.Method}$ is estimated in the same way as the calibration factor and in the same binning is derived and the result is shown in Fig. 13.14, showing that relative difference became much closer to 1 when comparing with the Fig. 13.13.

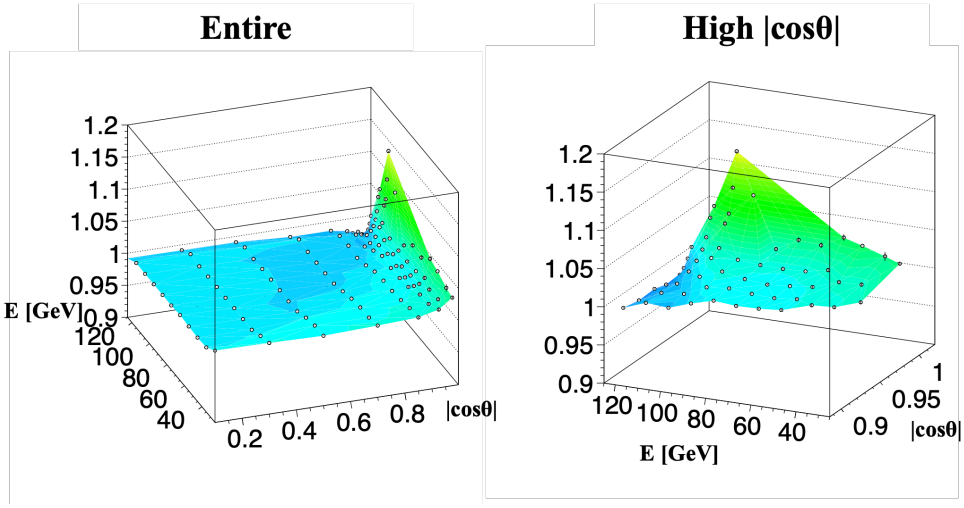

Figure 13.13: Distribution of the calibration factor as a function of energy and $|\cos\theta|$. Left-side figure shows all energy and $|\cos\theta|$ region while right shows only high $|\cos\theta|$ region.

Next, we will investigate the calibration uncertainty expected at the ILC. The overall jet energy scale uncertainty for this calibration can be estimated using the following equation:

$$\text{Calibration Uncertainty} = \sqrt{(\Delta\mu_{PFO})^2 + (\Delta\mu_{Ang.Method})^2}, \tag{13.1}$$

here $\Delta\mu$ denotes the error of the mean value of the fitting core Gaussian. The jet energy scale uncertainty calculated this way is shown in Fig. 13.15.

Figure 13.15 shows that the jet energy scale uncertainty is $\sim 10^{-4}$ which corresponds to $\sim$ 10 MeV.

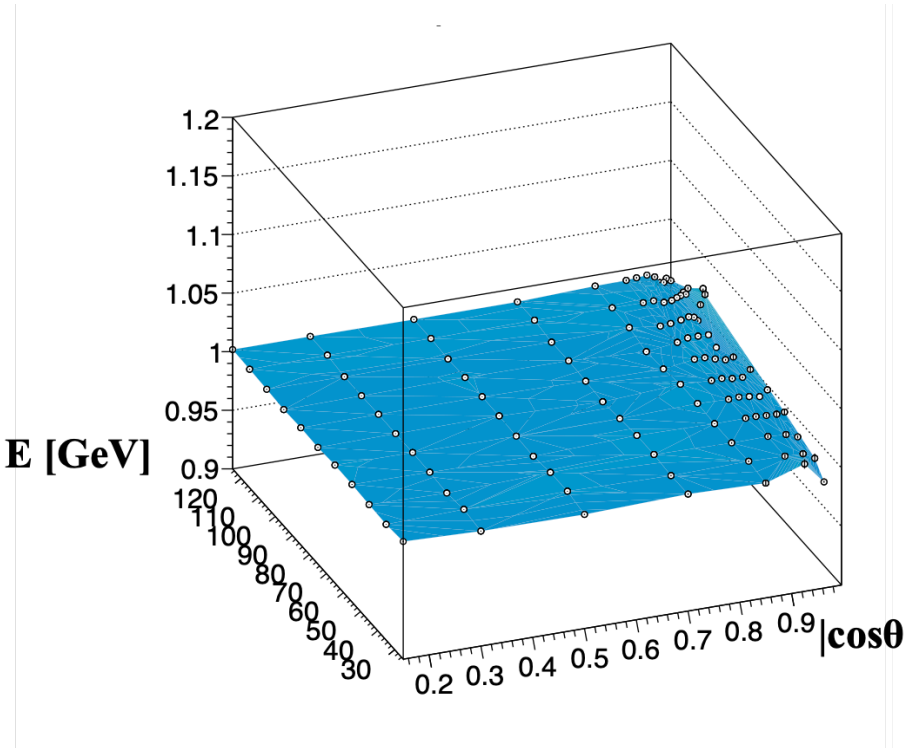

Figure 13.14: Distribution of the relative difference between calibrated E_J^{PFO} and $E_J^{Ang.Method}$ as a function of energy and $|\cos\theta|$ for all energy and $|\cos\theta|$ region. This plot shows that relative difference became much closer to 1 when comparing with the Fig. 13.13.

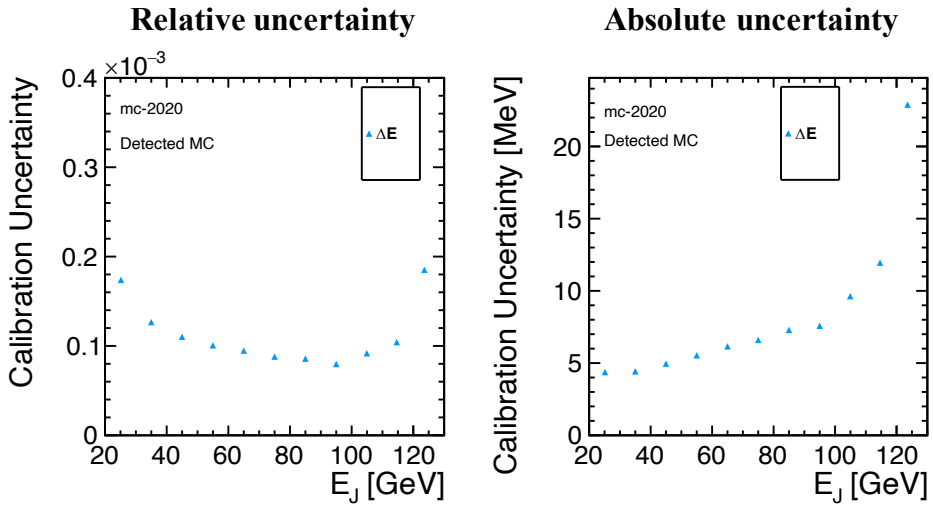

Figure 13.15: E_J scale uncertainty after the jet energy calibration using the Angular Method as a function of E_γ. Left figure shows the relative values and right shows the absolute values.

Chapter 14

Summary of Part III

In order to reduce the systematic error of the JES measurement, we developed a data-driven method to calibrate the jet energy. This method makes use of measured jet masses and jet and photon directions to extract jet energies without reference to the directly measured energies in the $e^+e^- \to \gamma Z, Z \to 2\,\text{Jets}$ process. Various methods to calibrate the jet energy are studied in full-simulation demonstration. Among the five kinematic reconstruction methods studied, the Angular Method is found to be the best due to its good resolution and peak position. By comparing the Angular Method reconstructed and directly measured jet energies, the reconstructed jet energy resolution is concluded to be better than the measured one. The jet energy kinematically reconstructed by the Angular Method can recover energies of undetected particles. Using this method, calibration factors are estimated as a function of energy and polar angle. We can achieve JES accuracy of $\sim 10^{-4}$, which corresponds to absolute energy uncertainty of about 5 to 20 MeV.

Part IV

Measurement of A_{LR} at the ILC

Chapter 15

Simulation Setup

In this part, signal events $e^+e^- \to \gamma Z$ are first generated using Whizard 2.85 [38] and simulated in the ILD_l5_v02. We consider the model with Si-ECAL and AHCAL calorimeter. It implements the 14 mrad beam crossing angle, IP smearing and offset depending on the initial particles [38]. The whole set of programs used in this analysis is packaged as iLCSoft version v02-02 [38]. The event simulation for this analysis has been done at the center-of-mass energy of 250 GeV. The assumed integrated luminosity is $\int Ldt = 900\,\mathrm{fb}^{-1}$ each for the two beam polarizations $(P_{e^-}, P_{e^+}) = (-0.8, +0.3)$ and $(+0.8, -0.3)$. The sample is generated with

$$\sin^2\theta_W = 0.22225 \tag{15.1}$$

which is equivalent to

$$A_{LR} = 0.219298. \tag{15.2}$$

In our analysis, all particles are forced to be clustered into 2 jets and the jet with higher reconstructed energy is defined as "jet 1 " and the other as "jet 2 " .

Chapter 16

Signal Definition and Background

We define the signal channel as $e^+e^- \to \gamma Z$ and $Z \to q\bar{q}$ process. Radiative return photons are so collinear with the e^-/e^+ beam that they go into the beam pipe in most events (Fig. 16.1). Then only 2 jets remain in the final state and many processes, *e.g.* those shown in Fig. 16.2, can be background. Our $e^+e^- \to q\bar{q}$ samples also contain events in which the Z is not on-shell. In order to evaluate the error of A_{LR}, we need to select signal events and distinguish signal events from background.

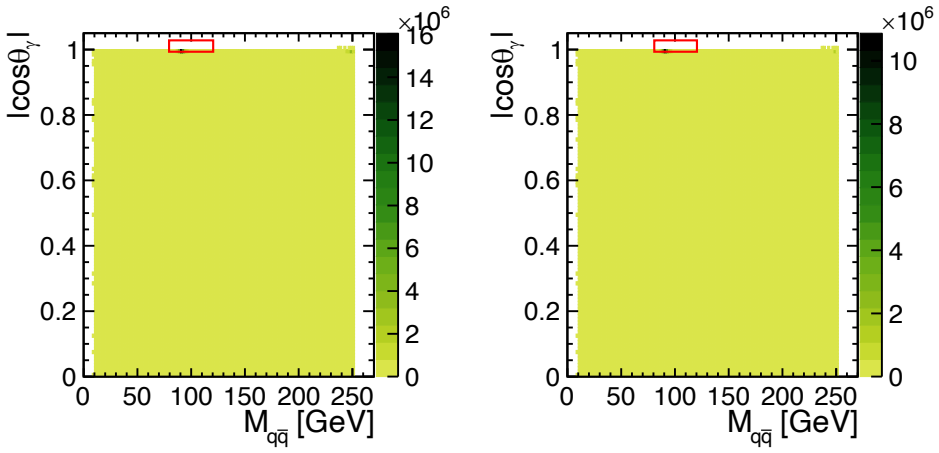

Figure 16.1: Photon angle and invariant mass of Z boson distributions in the $e^+e^- \to q\bar{q}$ samples. Each vertical axis is absolute value of cosine of polar angle of the signal photon. Left plot corresponds to $(P_{e^-}, P_{e^+}) = (-0.8, +0.3)$ case and right plot corresponds to $(+0.8, -0.3)$ case. Most photons are very forward. Red surrounded region corresponds to the "core signal".

Events satisfying following "Preselection A" in our $e^+e^- \to q\bar{q}$ samples are signal events and events satisfying both 'Preselection A" and 'Preselection B" are defined as "core signal", which may comprises the major part of the radiative return events.

Preselection A: $80\,\mathrm{GeV} < M_{q\bar{q}}(\text{MC truth}) < 120\,\mathrm{GeV}$
Preselection B: $|\cos\theta_\gamma(\text{MC truth})| > 0.999$

The considered samples have a final state of two leptons "2f_l", two quarks "2f_h", four leptons

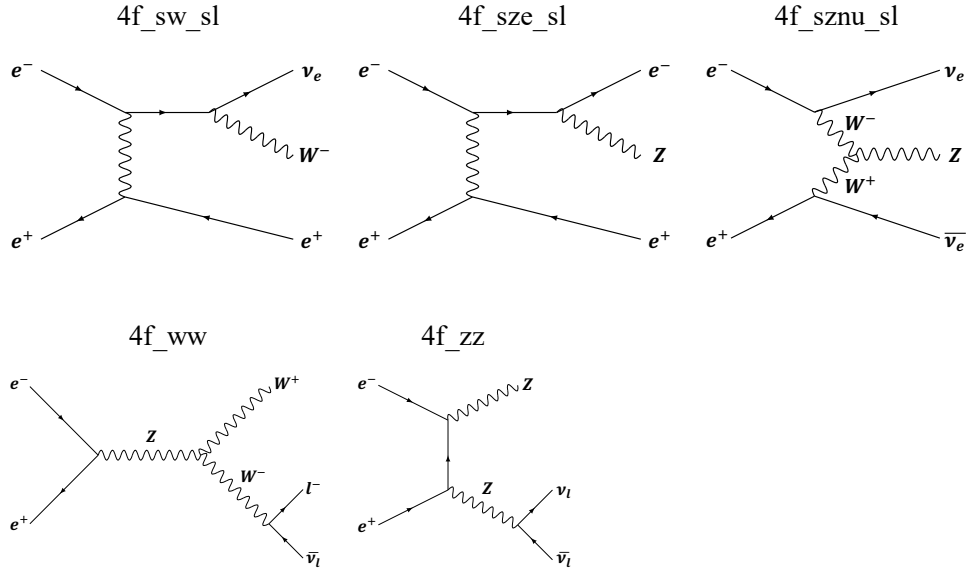

Figure 16.2: Potential processes which can be background for the $e^+e^- \to \gamma Z$ and $Z \to q\bar{q}$ process with abbreviated process names.

"4f_l", two quarks and two leptons "4f_sl", and four quarks "4f_h". In order to suppress background events, background exclusion cuts are defined as follows by considering distributions of several observables useful for the cuts.

Cut 1 $N_{\gamma(E>50\,\mathrm{GeV})} = 0$
Cut 2 $120\,\mathrm{GeV} < E_{vis} < 160\,\mathrm{GeV}$
Cut 3 $|\cos\theta_{2j}| > 0.95$
Cut 4 $N_{J1}^{charged} + N_{J2}^{charged} > 4$
Cut 5 $N_{J1}^{total} + N_{J2}^{total} > 10$
Cut 6 $50\,\mathrm{GeV} < M_{2j} < 160\,\mathrm{GeV}$
Cut 7 $\cos\theta_{12} > -0.99$ or $\frac{E_{J1}-E_{J2}}{E_{J1}+E_{J2}} > 0.5$

Distributions of total visible energy E_{vis}, total momentum direction of the 2-jet system $|\cos\theta_{2j}|$, the number of detected charged particles for each jet $N_{J1}^{charged}$ and $N_{J2}^{charged}$, the sum of the numbers of detected charged and neutral particles N_{J1}^{total} and N_{J2}^{total}, and the invariant mass of the 2-jet system M_{2j} of the signal and background processes for each polarization case are shown in Fig. 16.3 to Fig. 16.7, respectively. According to Fig. 16.5 and Fig. 16.6, it is effective to suppress the background events using the sum $N_{J1}^{charged} + N_{J2}^{charged}$ and $N_{J1}^{total} + N_{J2}^{total}$.
After Cut 1 to 6, photon angle and invariant mass of Z boson distributions of our $e^+e^- \to q\bar{q}$ samples show two different components (Fig. 16.8): $M_{q\bar{q}} \sim 91.2$ GeV radiative return-like events and $M_{q\bar{q}} \sim 250$ GeV events. Figure 16.9 shows the distributions of opening angle of two jets $\cos\theta_{12}$ and jet energy asymmetry $\frac{E_{J1}-E_{J2}}{E_{J1}+E_{J2}}$ for 80 GeV $< M_{q\bar{q}} <$ 120 GeV signal, $M_{q\bar{q}} > 240$ GeV signal, and backgrounds after Cut 6. In order to exclude the $M_{q\bar{q}} \sim 250$ GeV events in signal, we use Cut 7 in addition as jets are not back-to-back and jet energies are asymmetric in radiative return events.

Table 16.1 and Table 16.2 show the luminosity normalized expected number of remaining events after each cut for $(P_{e^-}, P_{e^+}) = (-0.8, +0.3)$ and $(+0.8, -0.3)$ polarization, respectively

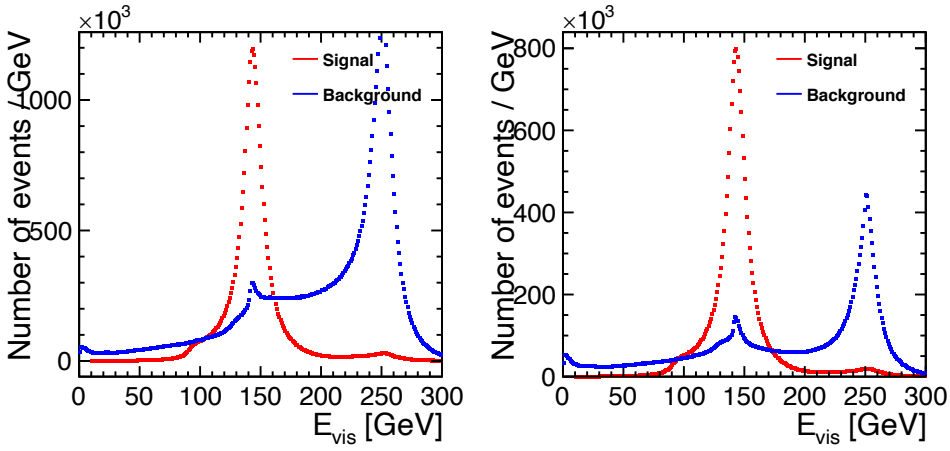

Figure 16.3: Distribution of the visible energy E_{vis} of signal and background processes after Cut 1 for each polarization case. Left plot corresponds to $(P_{e^-}, P_{e^+}) = (-0.8, +0.3)$ case and right plot corresponds to $(+0.8, -0.3)$ case.

at the ILC 250. A stack plot for the signal and background events after Cuts 1 through 7 is shown as a function of the reconstructed invariant mass of the 2-jet system M_{2j} in Fig. 16.10.

Table 16.1: Reduction table for signal and each background processes for $(P_{e^-}, P_{e^+}) = (-0.8, +0.3)$ polarization, assuming $\int Ldt = 900\,\text{fb}^{-1}$.

$\times 10^6$ events	Signal	Signal (Core)	2f_l	4f_l	4f_sl	4f_h	2f_h	Bkg. Total
Expected	46.0	32.5	12.7	9.34	17.2	15.1	23.6	78.1
Cut 1	32.7	31.1	10.1	5.96	16.0	14.8	21.6	68.3
Cut 2	24.6	24.4	2.55	1.46	3.22	0.00422	1.09	8.32
Cut 3	24.5	24.4	1.93	0.366	0.526	0.00352	1.04	3.87
Cut 4	24.4	24.3	0.299	0.0574	0.523	0.00352	1.00	1.88
Cut 5	24.3	24.2	0.0651	0.0102	0.520	0.00352	0.977	1.58
Cut 6	24.2	24.2	0.0571	0.00807	0.470	0.00210	0.694	1.23
Cut 7	24.2	24.1	0.0534	0.00647	0.463	0.00204	0.682	1.21

According to Table 16.1 and Table 16.2, signal selection efficiencies are 0.52678 ± 0.00017 and 0.52715 ± 0.00016 for $(P_{e^-}, P_{e^+}) = (-0.8, +0.3)$ and $(+0.8, -0.3)$ polarizations, respectively, where we assumed the error on the efficiency is binomial:

$$\Delta\eta = \sqrt{\frac{\eta(1-\eta)}{N_{generated}}}. \tag{16.1}$$

Background-to-signal ratios are 0.0499 and 0.0461 for $(P_{e^-}, P_{e^+}) = (-0.8, +0.3)$ and $(+0.8, -0.3)$ polarizations respectively after the seven cuts. For the core signal, selection efficiencies are 0.74166 ± 0.00015 and 0.74235 ± 0.00014 and background-to-signal ratios are 0.0500 and 0.0462 for $(P_{e^-}, P_{e^+}) = (-0.8, +0.3)$ and $(+0.8, -0.3)$ polarizations, respectively.

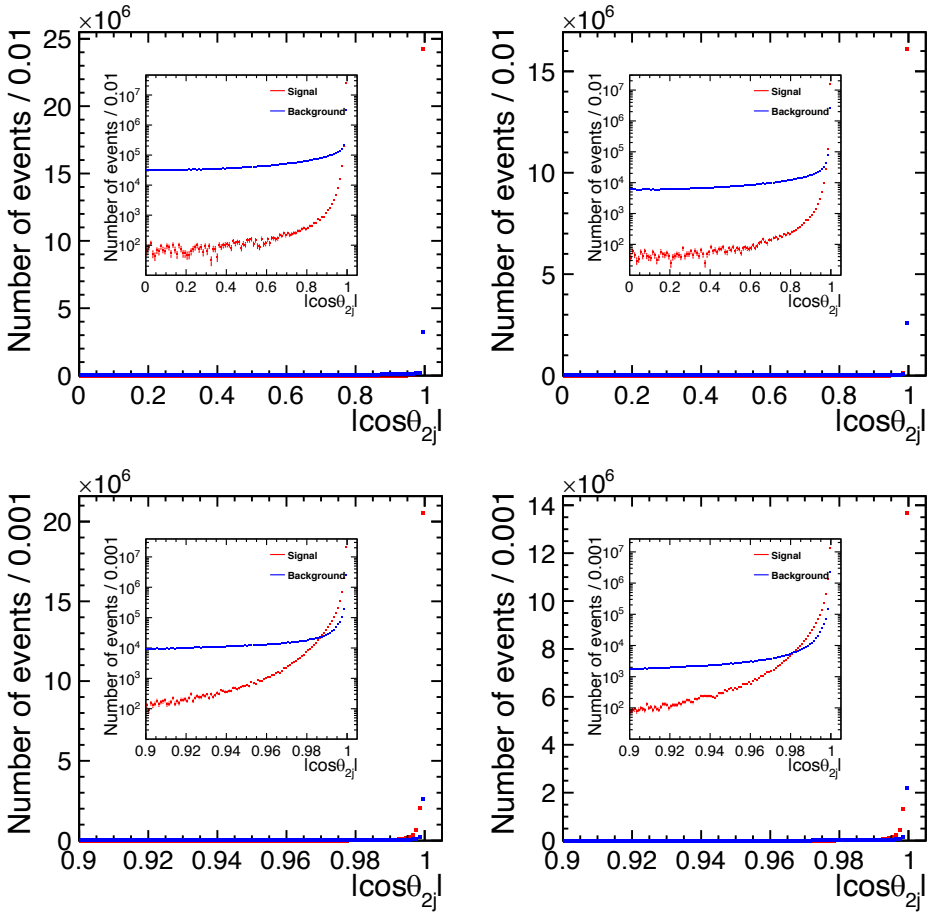

Figure 16.4: Distribution of the total momentum direction of the 2-jet system $|\cos\theta_{2j}|$ of signal and background processes after Cut 1 and 2 for each polarization case. Left two plots correspond to $(P_{e^-}, P_{e^+}) = (-0.8, +0.3)$ case and right two plots correspond to $(+0.8, -0.3)$ case. Top plots show entire $|\cos\theta_{2j}|$ region and bottom plots show high $|\cos\theta_{2j}|$ region.

Table 16.2: Reduction table for signal and each background processes for $(P_{e^-}, P_{e^+}) = (+0.8, -0.3)$ polarization, assuming $\int Ldt = 900\,\text{fb}^{-1}$.

$\times 10^6$ events	Signal	Signal (Core)	2f_l	4f_l	4f_sl	4f_h	2f_h	Bkg. Total
Expected	30.5	21.6	9.84	5.50	2.56	1.41	10.6	29.9
Cut 1	21.7	20.6	7.77	2.33	1.86	1.38	9.37	22.7
Cut 2	16.3	16.2	1.83	0.378	0.370	0.00137	1.04	3.62
Cut 3	16.3	16.2	1.37	0.259	0.106	0.00124	1.03	2.77
Cut 4	16.2	16.1	0.212	0.0357	0.104	0.00124	0.985	1.34
Cut 5	16.2	16.1	0.0454	0.00603	0.102	0.00124	0.958	1.11
Cut 6	16.1	16.0	0.0396	0.00468	0.0934	0.000986	0.616	0.754
Cut 7	16.1	16.0	0.0372	0.00320	0.0900	0.000967	0.609	0.740

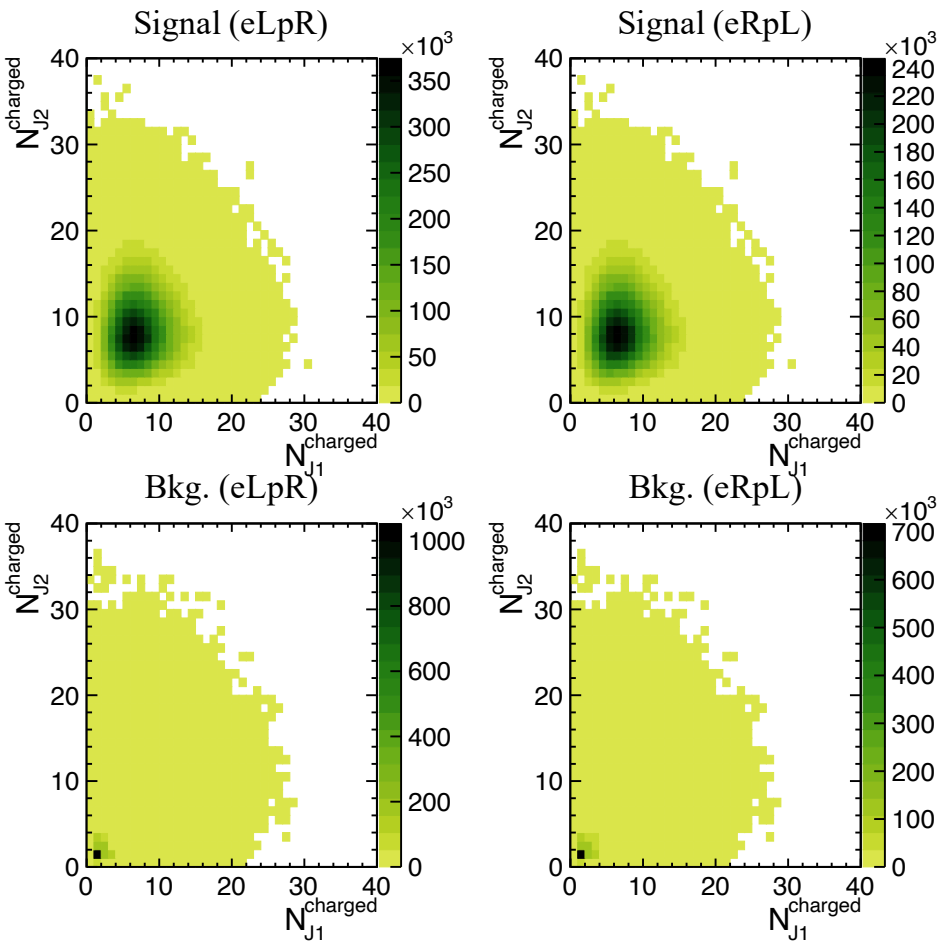

Figure 16.5: Distribution of the number of detected charged particles for each jet $N_{J1}^{charged}$ and $N_{J2}^{charged}$ of signal and background processes after Cut 1 to 3 for each polarization case. Top and bottom plots corresponds to signal and background processes. Left two plots correspond to $(P_{e^-}, P_{e^+}) = (-0.8, +0.3)$ case and right two plots correspond to $(+0.8, -0.3)$ case.

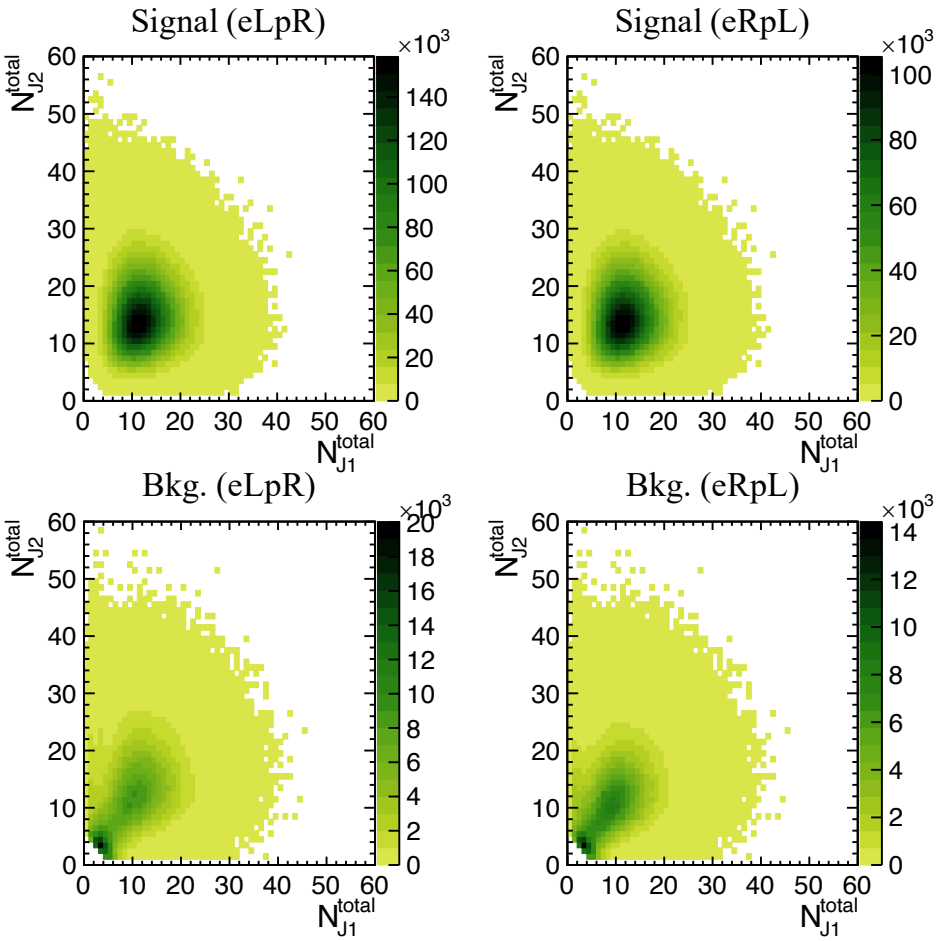

Figure 16.6: Distribution of the number of detected particles for each jet N_{J1}^{total} and N_{J2}^{total} of signal and background processes after Cut 1 to 4 for each polarization case. Top and bottom plots corresponds to signal and background processes. Left two plots correspond to $(P_{e^-}, P_{e^+}) = (-0.8, +0.3)$ case and right two plots correspond to $(+0.8, -0.3)$ case.

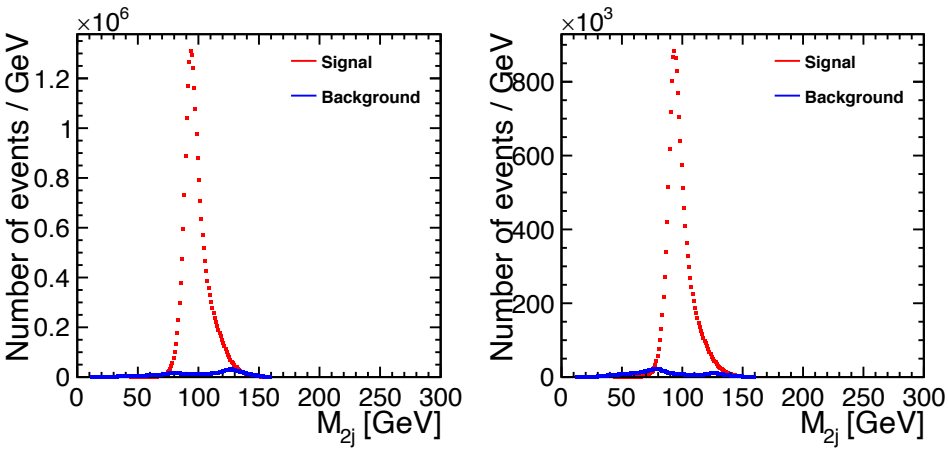

Figure 16.7: Distribution of the invariant mass of 2-jet system M_{2j} of signal and background process after Cut 1 to 5 for each polarization case. Left plot corresponds to $(P_{e^-}, P_{e^+}) = (-0.8, +0.3)$ case and right plot corresponds to $(+0.8, -0.3)$ case.

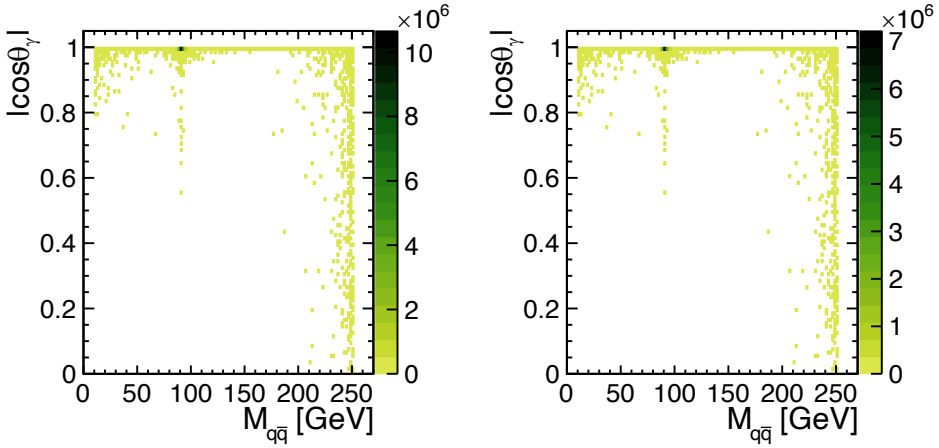

Figure 16.8: Photon angle and invariant mass of Z boson distributions for $e^+e^- \to q\bar{q}$ samples after Cut 1 to 6. Each vertical axis is absolute value of cosine of polar angle of the signal photon. Left plot corresponds to $(P_{e^-}, P_{e^+}) = (-0.8, +0.3)$ case and right plot corresponds to $(+0.8, -0.3)$ case.

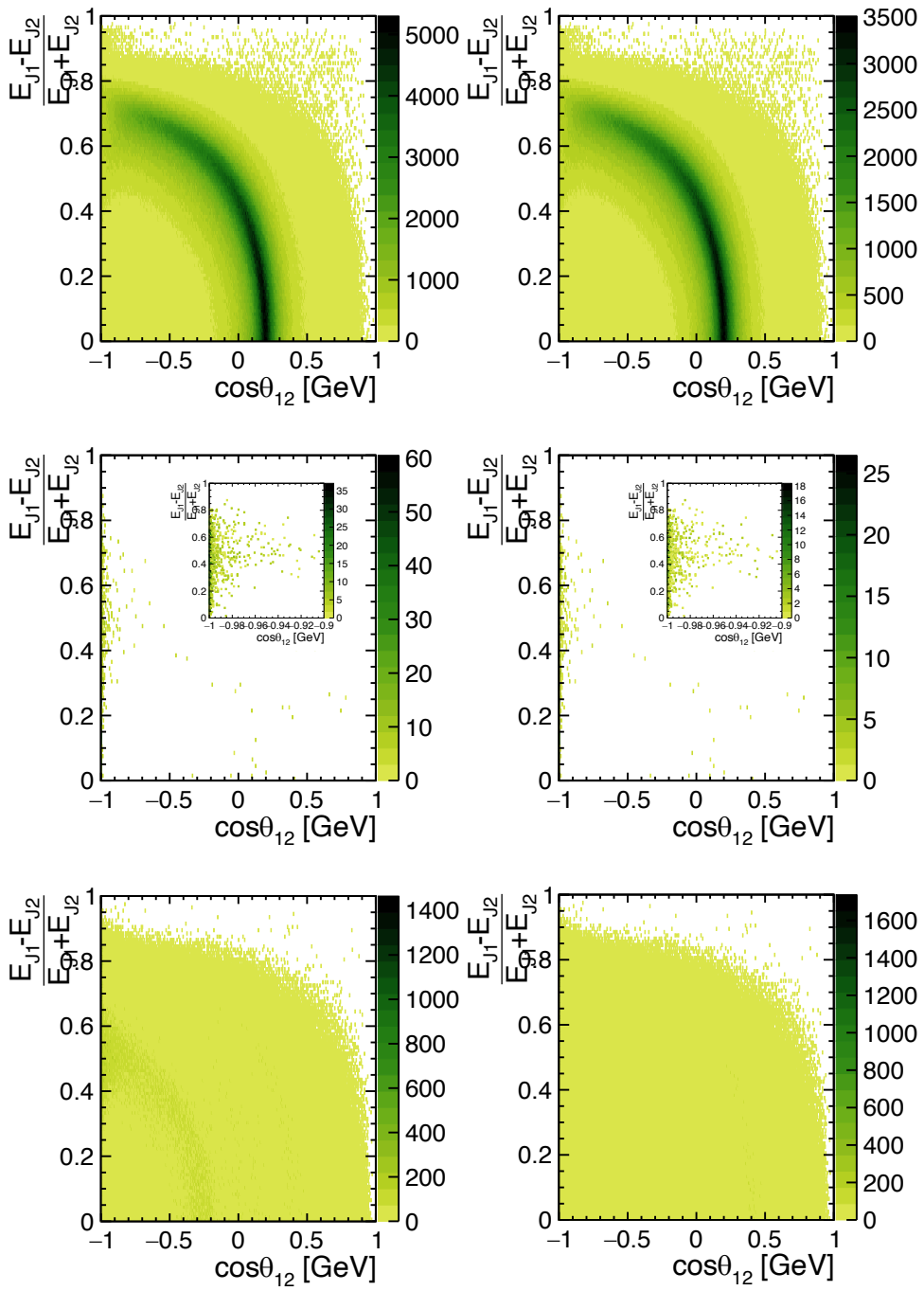

Figure 16.9: Distributions of opening angle of two jets $\cos\theta_{12}$ and jet energy asymmetry $\frac{E_{J1}-E_{J2}}{E_{J1}+E_{J2}}$ for 80 GeV $< M_{q\bar{q}} <$ 120 GeV signal (top), $M_{q\bar{q}} >$ 240 GeV signal (middle), and backgrounds (bottom) after Cut 1 to 6. Left plots correspond to $(P_{e^-}, P_{e^+}) = (-0.8, +0.3)$ case and right plots correspond to $(+0.8, -0.3)$ case.

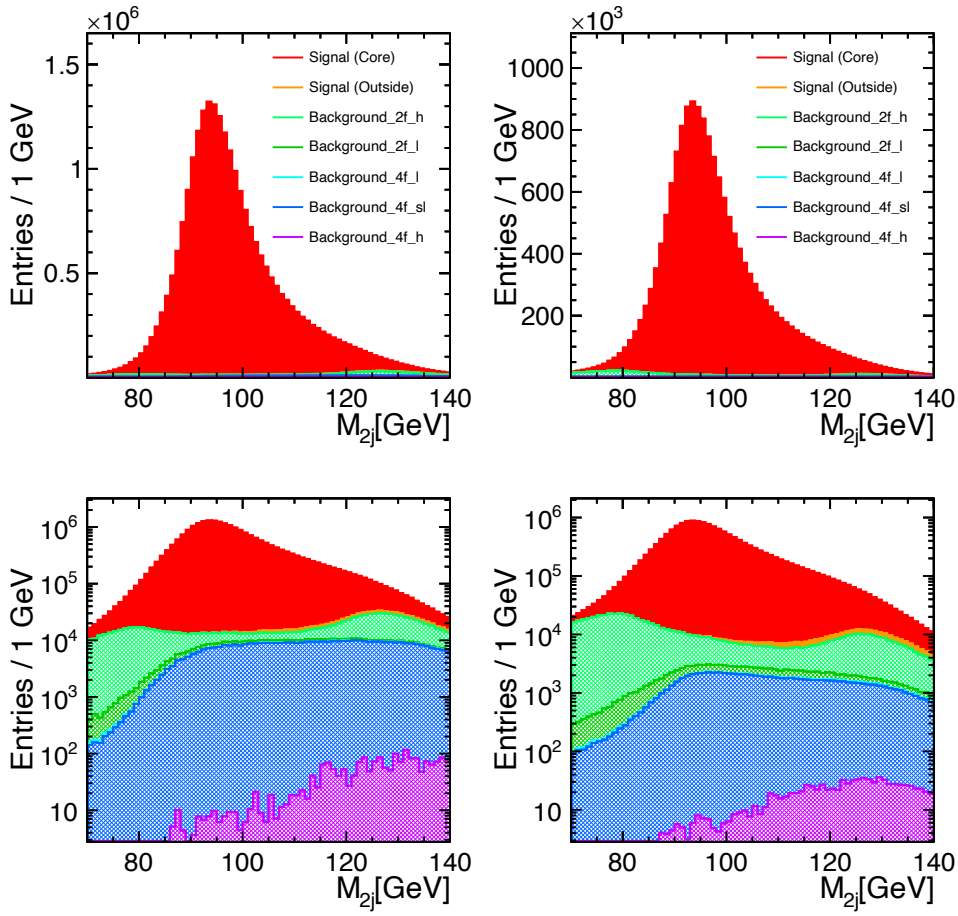

Figure 16.10: Stack plot of the invariant mass of 2-jet system M_{2j} for the signal and background events for $(P_{e^-}, P_{e^+}) = (-0.8, +0.3)$ and $(+0.8, -0.3)$ polarization. Left plots are $(P_{e^-}, P_{e^+}) = (-0.8, +0.3)$ and right plots are $(+0.8, -0.3)$ polarization respectively after Cut 1 to 7. They are show in linear scale in top plots and in log scale in bottom plots.

Chapter 17

Evaluation of the Error

We now consider the error on A_{LR} (2.32). Assume the real experimental case of electron polarization P_- is $|P_-| = 0.8$ and positron polarization P_+ is $|P_+| = 0.3$. The observed left-right asymmetry A_{LRobs} is defined using the cross section of the Z production in eLpR polarization σ_- and eRpL polarization σ_+,

$$A_{LRobs} = \frac{\sigma_- - \sigma_+}{\sigma_- + \sigma_+}. \tag{17.1}$$

Relations between σ_-/σ_+ and σ_L/σ_R, which correspond to cross sections with 100% polarized beams, are

$$\begin{aligned} \sigma_- &= \frac{1}{4}(1+|P_-|)(1+|P_+|)\sigma_L + \frac{1}{4}(1-|P_-|)(1-|P_+|)\sigma_R \\ \sigma_+ &= \frac{1}{4}(1-|P_-|)(1-|P_+|)\sigma_L + \frac{1}{4}(1+|P_-|)(1+|P_+|)\sigma_R. \end{aligned} \tag{17.2}$$

Then,

$$A_{LR} = A_{LRobs}\frac{1+|P_-||P_+|}{|P_-|+|P_+|} = A_{LRobs} \times f. \tag{17.3}$$

The error on A_{LR} is expressed as

$$\left(\frac{\Delta A_{LR}}{A_{LR}}\right)^2 = \left(\frac{\Delta A_{LRobs}}{A_{LRobs}}\right)^2 + \left(\frac{\Delta f}{f}\right)^2. \tag{17.4}$$

Then error propagation derives

$$\left(\frac{\Delta f}{f}\right)^2 = \left(\frac{|P_-|(1+|P_+|)(1-|P_+|)}{(|P_-|+|P_+|)(1+|P_-||P_+|)}\right)^2 \left(\frac{\Delta|P_-|}{|P_-|}\right)^2 + \left(\frac{|P_+|(1+|P_-|)(1-|P_-|)}{(|P_-|+|P_+|)(1+|P_-||P_+|)}\right)^2 \left(\frac{\Delta|P_+|}{|P_+|}\right)^2. \tag{17.5}$$

In order to evaluate the error on A_{LRobs}, we define the number of Z production events in the eLpR polarization as N_- and the eRpL polarization as N_+, respectively,

$$\begin{aligned} N_- &= \eta_- L_- \sigma_- \\ N_+ &= \eta_+ L_+ \sigma_+, \end{aligned} \tag{17.6}$$

where η and L are the selection efficiency and the integrated luminosity, respectively. We will consider the product of η and L as

$$\begin{aligned} \alpha &= L_-\eta_- \\ \beta &= L_+\eta_+, \end{aligned} \tag{17.7}$$

then

$$A_{LRobs} = \frac{\frac{N_-}{\alpha} - \frac{N_+}{\beta}}{\frac{N_-}{\alpha} + \frac{N_+}{\beta}}. \tag{17.8}$$

The error on A_{LRobs} is expressed as

$$\begin{aligned} \left(\frac{\Delta A_{LRobs}}{A_{LRobs}}\right)^2 &= \left(\frac{2\left(\frac{N_-}{\alpha}\right)\left(\frac{N_+}{\beta}\right)}{\left(\frac{N_-}{\alpha} - \frac{N_+}{\beta}\right)\left(\frac{N_-}{\alpha} + \frac{N_+}{\beta}\right)}\right)^2 \left(\left(\frac{\Delta\alpha}{\alpha}\right)^2 + \left(\frac{\Delta\beta}{\beta}\right)^2 + \left(\frac{\Delta N_-}{N_-}\right)^2 + \left(\frac{\Delta N_+}{N_+}\right)^2\right) \\ &= \left(\frac{1}{2A_{LRobs}}\left(1 - A_{LRobs}^2\right)\right)^2 \left(\left(\frac{\Delta\alpha}{\alpha}\right)^2 + \left(\frac{\Delta\beta}{\beta}\right)^2 + \left(\frac{\Delta N_-}{N_-}\right)^2 + \left(\frac{\Delta N_+}{N_+}\right)^2\right). \end{aligned} \tag{17.9}$$

Using (17.4), (17.5) and (17.9), we can evaluate the error on A_{LR}.

First, we assume that the errors of f, η, and L are negligible. From this calculation, statistical error will be obtained. If we further assume that background is negligible *i.e.* $(\sqrt{N_{-S} + N_{-B}})^2 \sim N_{-S}$ and $(\sqrt{N_{+S} + N_{+B}})^2 \sim N_{+S}$ where N_{+S} and N_{-S} are numbers of Z production events in the signal and N_{+B} and N_{-B} are numbers of the background events, then (17.9) gives

$$(\Delta A_{LRobs})^2 = \left(\frac{1}{2}\left(1 - A_{LRobs}^2\right)\right)^2 \left(\left(\frac{\Delta N_-}{N_-}\right)^2 + \left(\frac{\Delta N_+}{N_+}\right)^2\right). \tag{17.10}$$

Now we define the overall number of Z production events as N *i.e.* $N = N_- + N_+$.
When we assume that $\eta_- = \eta_+$ and $L_- = L_+$ *i.e.* $\alpha = \beta$,

$$\begin{aligned} N_- &= \frac{N}{2}(1 + A_{LRobs}) \\ N_+ &= \frac{N}{2}(1 - A_{LRobs}). \end{aligned} \tag{17.11}$$

Then, the error on A_{LRobs} is

$$(\Delta A_{LRobs})^2 = \frac{1}{N}(1 + A_{LRobs})(1 - A_{LRobs}). \tag{17.12}$$

In this case of a very small number of background events, we can estimate the statistical error just from A_{LRobs} and N. Using the results in Table 16.1 and Table 16.2 in (17.12) and translating the A_{LRobs} into A_{LR} by (17.3),

$$A_{LR} = 0.22810 \pm 0.00017\,(stat) \tag{17.13}$$

for all signal. This statistical error is ~ 12.3 times better than the overall error at the SLC. For the core signal,

$$A_{LR} = 0.22827 \pm 0.00017\,(stat) \tag{17.14}$$

In the case that we have a non-negligible number of background events, we should replace the (17.10) as follows.

$$(\Delta A_{LRobs})^2 = \left(\frac{1}{2}\left(1 - A_{LRobs}^2\right)\right)^2 \left(\left(\frac{\sqrt{N_{-S} + N_{-B}}}{N_{-S}}\right)^2 + \left(\frac{\sqrt{N_{+S} + N_{+B}}}{N_{+S}}\right)^2\right). \quad (17.15)$$

When we use this more accurate evaluation, the statistical error on A_{LR} is estimated to be 1.8×10^{-4} which is almost identical to the result in the previous definition, which confirms the number of background is indeed negligible.
The derived A_{LR} value (17.13) does not agree with the simulation setting 0.219 in (15.2). If we change the range of $M_{q\bar{q}}$ in the signal definition *i.e.* Preselection A, the A_{LR} value is changed. The $M_{q\bar{q}}$ dependence of the A_{LR} value is shown in Fig. 17.1. Fig. 17.1 indicates that events with

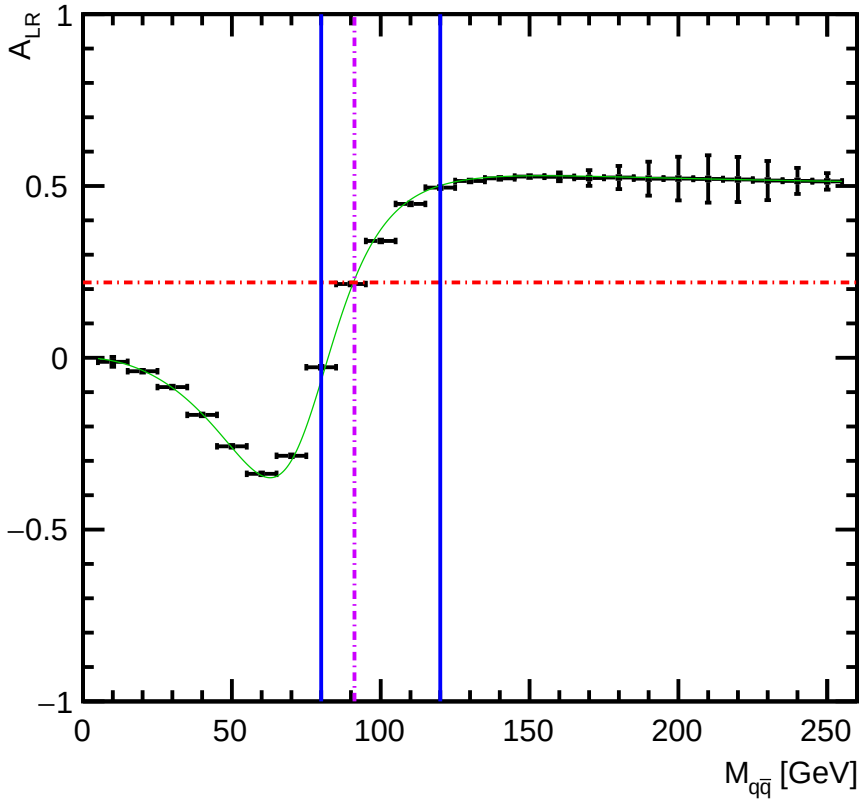

Figure 17.1: $M_{q\bar{q}}$ dependence of A_{LR}. Red dashed line corresponds to the simulation setting and blue lines are boundaries of signal and background in our analysis. Green curve shows the theoretical prediction when $\sin^2\theta_W = 0.2225$. In our signal region, the A_{LR} value varies almost linearly and we can cancel the deviation by taking appropriate $M_{q\bar{q}}$ range.

$M_{q\bar{q}}$ away from the Z-pole dominantly cause the discrepancy. This discrepancy was caused by another process contained in the sample *i.e.* the $e^+e^- \to \gamma \to q\bar{q}$ diagram contamination. In our signal region, the A_{LR} value varies almost linearly and we can cancel the deviation by taking appropriate $M_{q\bar{q}}$ range.

We have so far been assuming that the polarization $|P_-|$ and $|P_+|$, selection efficiency η, and integrated luminosity L have no errors. However, these have errors and the errors can cause further systematic error on A_{LR}.
When including the predicted polarization error of $\frac{\Delta|P_-|}{|P_-|} = \frac{\Delta|P_+|}{|P_+|} = 0.001$ into (17.5) [43], the total absolute error on A_{LR} is estimated to be 0.000216 for all signal.
Next, errors on α and β will be considered. Most of the error on α and β are correlated because α and β are evaluated in the same setup. We now show that this correlated part has a negligible effect. We define the error matrix of α and β as Er,

$$(\Delta A_{LRobs})^2 = \begin{pmatrix} \frac{\partial A_{LRobs}}{\partial \alpha} & \frac{\partial A_{LRobs}}{\partial \beta} \end{pmatrix} Er \begin{pmatrix} \frac{\partial A_{LRobs}}{\partial \alpha} \\ \frac{\partial A_{LRobs}}{\partial \beta} \end{pmatrix} \tag{17.16}$$

$$Er \equiv \begin{pmatrix} <(\Delta\alpha)^2> & <(\Delta\alpha)(\Delta\beta)> \\ <(\Delta\alpha)(\Delta\beta)> & <(\Delta\beta)^2> \end{pmatrix} \tag{17.17}$$

and divide Er into uncorrelated and fully correlated error contributions,

$$Er = \begin{pmatrix} u_\alpha & 0 \\ 0 & u_\beta \end{pmatrix} + \begin{pmatrix} c & c \\ c & c \end{pmatrix}. \tag{17.18}$$

As

$$\begin{aligned} \begin{pmatrix} \frac{\partial A_{LRobs}}{\partial \alpha} \\ \frac{\partial A_{LRobs}}{\partial \beta} \end{pmatrix} &= \left(\frac{2\left(\frac{N_{-+}}{\alpha}\right)\left(\frac{N_{+-}}{\beta}\right)}{\left(\frac{N_{-+}}{\alpha} + \frac{N_{+-}}{\beta}\right)^2} \right) \begin{pmatrix} -\frac{1}{\alpha} \\ \frac{1}{\beta} \end{pmatrix} \\ &= \left(\frac{1}{2}\left(1 - A_{LRobs}^2\right) \right) \begin{pmatrix} -\frac{1}{\alpha} \\ \frac{1}{\beta} \end{pmatrix}, \end{aligned} \tag{17.19}$$

$$(\Delta A_{LRobs\_correlated})^2 = c \times \left(\frac{1}{2}\left(1 - A_{LRobs}^2\right) \right)^2 \left(\frac{1}{\alpha} - \frac{1}{\beta} \right)^2 \tag{17.20}$$

$$\Delta A_{LRobs\_correlated} \simeq \frac{1}{2}\left(1 - A_{LRobs}^2\right) \times \left| \frac{\beta - \alpha}{\alpha} \right| \times \frac{\sqrt{c}}{\alpha}. \tag{17.21}$$

This (17.21) means if the integrated luminosity is adjusted to satisfy $\alpha = \beta$ in the experiment, this correlated part would disappear. In the simulation sample used in this analysis,

$$\Delta A_{LRobs\_correlated} = \frac{\sqrt{c}}{\alpha} \times 3.4 \times 10^{-4}, \tag{17.22}$$

which is small enough to ignore. Therefore only uncorrelated parts of $\Delta\alpha$ and $\Delta\beta$ will be considered below. The possible sources of the uncorrelated error are the difference of selection efficiency in each polarization combination and time dependence of the luminosity measurements. If $\frac{\Delta\alpha}{\alpha} = \frac{\Delta\beta}{\beta} = 0.00016$ (*i.e.* 0.016%), the total systematic error on A_{LR} from polarization, selection efficiency, and luminosity is estimated to be 0.000174, comparable to the statistical error 0.000178. In this case, total absolute error on A_{LR} is 0.00025, 8.8 times better precision than that from the SLC (0.00219).

Chapter 18

Summary of Part IV

As A_{LR} is useful to constrain SMEFT parameters, it is motivated to improve this observable at the ILC. In order to assess by how much we can improve the precision, a full simulation study including $e^+e^- \to \gamma Z$ process and various background processes was performed. Signal events are defined as radiative return events with hadronic decay of the Z boson. In order to exclude background processes, cut conditions were considered. With the seven cuts considered, signal selection efficiencies are 0.52678 ± 0.00017 and 0.52715 ± 0.00016 for $(P_{e^-}, P_{e^+}) = (-0.8, +0.3)$ and $(+0.8, -0.3)$ polarizations, respectively. Background-to-signal ratios are 0.0499 and 0.0461 for each polarization combinations respectively after the cuts. For the core signal, selection efficiencies are 0.74166 ± 0.00015 and 0.74235 ± 0.00014 and background-to-signal ratios are 0.0500 and 0.0462 for $(P_{e^-}, P_{e^+}) = (-0.8, +0.3)$ and $(+0.8, -0.3)$ polarizations, respectively.

The statistical error on A_{LR} is estimated to be 1.8×10^{-4} with these cuts. When considering a polarization error of $\frac{\Delta|P_-|}{|P_-|} = \frac{\Delta|P_+|}{|P_+|} = 0.001$, the total absolute error on A_{LR} is estimated to be 0.000216. If the integrated luminosity is adjusted to satisfy the product of luminosity and selection efficiency is same for each polarization combination, the correlated part of the error on this product would disappear. Then we need to think about only uncorrelated parts. If $\frac{\Delta\alpha}{\alpha} = \frac{\Delta\beta}{\beta} = 0.00016$ (*i.e.* 0.016%), the total systematic error on A_{LR} from polarization, selection efficiency, and luminosity is estimated to be 0.000174, comparable to the statistical error 0.000178. In this case, total absolute error on A_{LR} is 0.00025, 8.8 times better precision than that from the SLC (0.00219).

Part V

Conclusion

Radiative return process $e^+e^- \to \gamma Z$ provides a large set of Z-pole data at initial stage of ILC at 250 GeV useful for both physics measurements and detector calibration. We performed the first full simulation study of this process based on ILD, including realistic SM background events.

• Photon energy scale calibration
ILC makes it possible to perform various precision measurement for the BSM and highly sensitive new particle search. So as to achieve this, a high performance detector which reconstructs all final states in terms of fundamental particles, *i.e.* leptons, quarks, gauge bosons, and the Higgs bosons are essential. By measuring each final state particle energy in the most proper way, we can identify the W, Z, and Higgs bosons which decay to jets. Not only accuracy of detected energy but also energy scale accuracy is essential for this precise final state reconstruction. Therefore, photon and jet energy scale calibration is important.
In order to reduce the systematic error of the photon energy measurement, a photon energy calibration method using the $e^+e^- \to \gamma Z$ process was developed. Among the five kinematic reconstruction methods studied, the Angular Method is found to be the best due to its good resolution and its symmetric response. The resolution of the photon energy kinematically reconstructed by the Angular Method is better than that of the PFO photon energy except in the singular regions near $\sin\phi_\gamma = 0$ and $|\cos\theta_\gamma| = 1$ and the Angular Method has almost no bias. We have hence shown that the PFO photon energy can be calibrated effectively using the Angular Method. It is concluded that the photon energy scale uncertainty after the calibration is below 80 MeV for $E_\gamma \sim 120$ GeV decreasing to 15 MeV for $E_\gamma \sim 250$ GeV.

• Jet energy scale calibration
In order to reduce the systematic error of the JES measurement, we developed a new data-driven jet energy calibration method (Angular Method) using kinematical reconstruction of the $e^+e^- \to \gamma Z$ process using measured jet masses and jet and photon angles. Among the five kinematic reconstruction methods studied, the Angular Method is found to be the best in terms of resolution and potential calibration bias. The jet energy kinematically reconstructed by the Angular Method can recover energies of undetected particles. Using this method, calibration factors are estimated as a function of energy and polar angle. We can achieve JES accuracy of $\sim 10^{-4}$, which corresponds to absolute energy uncertainty of about 5 to 20 MeV.

• Evaluation of the error of A_{LR} at the ILC
As A_{LR} is useful to constrain SMEFT parameters, it is motivated to improve this observable at the ILC. In order to assess by how much we can improve the precision, a full simulation study including $e^+e^- \to \gamma Z$ process and various background processes was performed. In order to exclude background processes, cut conditions were considered. For the radiative return with hadronic decay case, background-to-signal ratios are 0.0499 and 0.0461 for $(P_{e^-}, P_{e^+}) = (-0.8, +0.3)$ and $(+0.8, -0.3)$ polarization, respectively. The statistical error on A_{LR} is estimated to be 1.8×10^{-4} with these cuts. Considering the systematic errors from polarization, selection efficiency and integrated luminosity, we think most of this systematic error from efficiency and luminosity will be canceled out. The dominant systematic error would be the polarization uncertainty. If the errors from the uncorrelated part of the error on product of efficiency and luminosity is around 0.016%, the total systematic error is same size with the statistical error. In this case, the total absolute error on A_{LR} is 0.00025, 8.8 times better precision than the SLC.

AKNOWLEDGEMENTS

I am grateful to my supervisor Prof. Keisuke Fujii for giving me consistent support including instruction of theory, simulation, and detectors at the ILC, without whom I would not have been able to complete this research. I am also grateful to my supervisor Associate Prof. Daniel Jeans for providing me insightful suggestions and correcting my English writings. I express my sincere thanks to Assistant Prof. Junping Tian who gave me very important advices and technical assistances continuously. I would like to thank all KEK ILC group staff members for providing me useful comments and helpful discussions. I also appreciate ILD physics working group members. Finally, I would like to thank my family for supporting me to continue my research.

Bibliography

[1] K. Fujii *et al.*, arXiv:1710.07621 [hep-ex].

[2] T. Barklow *et al.*, Phys. Rev. D **97**, no. 5, 053003 (2018) doi:10.1103/PhysRevD.97.053003 [arXiv:1708.08912 [hep-ph]].

[3] T. Barklow *et al.*, Phys. Rev. D **97**, no. 5, 053004 (2018) doi:10.1103/PhysRevD.97.053004 [arXiv:1708.09079 [hep-ph]].

[4] J. Cohen *et al.*, Phys. Rev. D **94**, no. 3, 035030 (2016) doi:10.1103/PhysRevD.94.035030 [arXiv:1602.01698 [hep-ph]].

[5] The ALEPH Collaboration, the DELPHI Collaboration, the L3 Collaboration, the OPAL Collaboration, the SLD Collaboration, the LEP Electroweak Working Group, the SLD electroweak and heavy flavour groups, Precision Electroweak Measurements on the Z Resonance, 2005, Phys.Rept.427:257-454,2006; arXiv:hep-ex/0509008. DOI: 10.1016/j.physrep.2005.12.006.

[6] T. Ueno, A simulation study on measurement of the polarization asymmetry ALR using the initial state radiation at the ILC with center-of-mass energy of 250 GeV, Master Thesis, Tohoku University (2018).

[7] T. Behnke *et al.*, arXiv:1306.6329 [physics.ins-det].

[8] J. S. Marshall and M. A. Thomson, Eur. Phys. J. C **75**, no. 9, 439 (2015) doi:10.1140/epjc/s10052-015-3659-3 [arXiv:1506.05348 [physics.data-an]].

[9] Philip Bambade *et al.*, The International Linear Collider: A Global Project, 2019; arXiv:1903.01629.

[10] The ILD Concept Group, The International Large Detector: Letter of Intent, 2010; arXiv:1006.3396.

[11] Yorikiyo Nagashima, 朝倉物理学体系 6 高エネルギー物理学の発展, 1999

[12] Yoji Totsuka, 岩波講座 現代の物理学 第 10 巻 素粒子物理, 1992

[13] Yasushi Watanabe, 新物理学シリーズ 33 素粒子物理入門 -基本概念から最先端まで-, 2002

[14] Seiji Rin, 現代理論物理学シリーズ 5 素粒子の標準理論を超えて, 2015

[15] P.A. Zyla *et al.* (Particle Data Group), Prog. Theor. Exp. Phys. 2020, 083C01 (2020)

[16] Michael E. Peskin, Concepts of Elementary Particle Physics, version of April 2, 2019

[17] B. Grzadkowski *et al.*, Dimension-Six Terms in the Standard Model Lagrangian, 2010; arXiv:1008.4884. DOI: 10.1007/JHEP10(2010)085.

[18] Rodrigo Alonso *et al.*, Renormalization Group Evolution of the Standard Model Dimension Six Operators III: Gauge Coupling Dependence and Phenomenology, 2013; arXiv:1312.2014. DOI: 10.1007/JHEP04(2014)159.

[19] J. T. Boyd, LHC Run-2 and Future Prospects, 2020; arXiv:2001.04370.

[20] The ILD Collaboration, International Large Detector: Interim Design Report, 2020; arXiv:2003.01116.

[21] Keisuke Fujii *et al.*, Physics Case for the 250 GeV Stage of the International Linear Collider, 2017; arXiv:1710.07621.

[22] Chris Adolphsen *et al.*, The International Linear Collider Technical Design Report - Volume 3.II: Accelerator Baseline Design, 2013; arXiv:1306.6328.

[23] Nishitani,T. *et al.*, Highly polarized electrons from GaAs-GaAsP and InGaAs-AlGaAs strained-layer superlattice photocathodes, 2005; DOI:10.1063/1.1886888,

[24] S.Michizono, LCUK Community Planning Meeting for ILC. Sep 18, 2020.

[25] A. Besson *et al.*, From vertex detectors to inner trackers with CMOS pixel sensors, 2016; arXiv:1604.02957. DOI: 10.1016/j.nima.2016.04.081.

[26] C. Calancha Paredes *et al.*, " Progress in the development of the vertex detector with fine pixel CCD at the ILC ", PoS Vertex2013 (2013) 022.

[27] M. Vos *et al.*, " DEPFET active pixel detectors ", PoS VERTEX2009 (2009) 015.

[28] D. C. Arogancia, Study in a beam test of the resolution of a Micromegas TPC with standard readout pads, 2007, Nucl.Instrum.Meth.A602:403-414,2009; arXiv:0705.2210. DOI: 10.1016/j.nima.2009.01.014.

[29] D. Tsionou, On behalf of the LCTPC collaboration, "Studies on GEM modules for a Large Prototype TPC for the ILC", 2017. Nucl.Instrum.Meth.A845:309-312, Proceedings of the Vienna Conference on Instrumentation 2016, DOI: https://doi.org/10.1016/j.nima.2016.05.011.

[30] https://confluence.desy.de/display/ILD/Simulation

[31] iLCSoft authors, " iLCSoft Project Page ", https:// github.com/iLCSoft (2016).

[32] F. Gaede, iLCSoft Tutorial. DESY. July 16, 2018.

[33] https://ilcsoft.desy.de/portal/software_packages/lcio/

[34] F. Gaede, Advanced computing and analysis techniques in physics research. Proceedings, 10th International Workshop, ACAT05, Zeuthen, Germany, May 22-27, 2005, Nucl. Instrum. Meth. A**559**, 177 (2006).

[35] https://ilcsoft.desy.de/portal/software_packages/marlin/

[36] M Frank *et al.*, 2014 J. Phys.: Conf. Ser. 513 022010

[37] S. Agostinelli *et al.* (GEANT4), Nucl. Instrum. Meth. A**506**, 250 (2003).

[38] Hiroaki Ono and Akiya Miyamoto, Status of 250 GeV MC sample production ILD. software and analysis meeting 2021 Apr. 07. https://agenda.linearcollider.org/event/9170/contributions/47779/attachments/36590/57160/20210407_ILD_software_ono.pdf

[39] W. Kilian *et al.*, Eur. Phys. J. C **71**, 1742 (2011) doi:10.1140/epjc/s10052-011-1742-y [arXiv:0708.4233 [hep-ph]].

[40] Taikan Suehara and Tomohiko Tanabe, LCFIPlus: A Framework for Jet Analysis in Linear Collider Studies, 2015, Nucl.Instrum.Meth. A808 (2016), 109-116; arXiv:1506.08371. DOI: 10.1016/j.nima.2015.11.054.

[41] S. Catani *et al.*, New clustering algorithm for multi jet cross-sections in e^+e^- annihilation. Phys. Lett., B269:432
UTF2013438, 1991.

[42] T. Madlener, Tutorial: Introduction to iLCSoft. July 21, 2021.

[43] D. M. Asner *et al.*, ILC Higgs White Paper, 2013; arXiv:1310.0763.